Charles University in Prague
Faculty of Mathematics and Physics

DOCTORAL THESIS

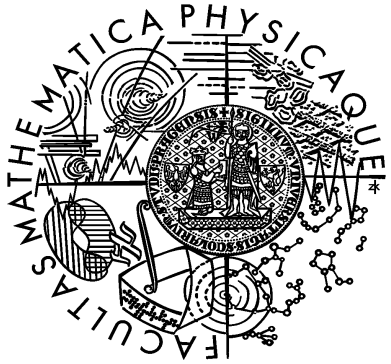

Olga Gutynska

Correlation properties of magnetosheath fluctuations

Department of Surface and Plasma Science

Thesis supervisor: Prof. RNDr. Jana Šafránková, DrSc.

Study Branch: f-2

Prague 2011

Preface

The work presented in this thesis has been carried out at the Department of Surface and Plasma Science of the Faculty of Mathematics and Physics of Charles University in Prague. I am first and foremost grateful to my supervisors Prof. Jana Šafránková and Prof. Zdeněk Němeček. Jana's dedication to research work, great patience, selflessness and her prompt grasping of relevant issues have greatly impressed me. Zdeněk's profound competence in physics, in particular the Space Physics, his excellent guidance and patience have advanced my knowledge and understanding in the field. Zdeněk is also an excellent teacher: he rarely takes anything as self-evident and always seems to have time and patience to discuss matters in detail. I am very happy to have had an opportunity to work with such front-line scientists.

I heartily thank to Dr. Lubomír Přech for his great help with data accessing and useful advice in programming in the course my work. Also, I wish to thank all academic staff of our Department for lecturing and willingness to help in understanding of fundamental principles of Plasma Physics.

I would also like to thank my family, especially my Mother, as she has always been a great support to me in all my undertakings; my in-laws for their support and existence, and my friends for the same reason. Finally, I wish to express my deepest gratitude to my husband Andrey, whose efforts concerning this thesis were not merely to support and inspire me; he also provided excellent ground-level comments on this thesis.

This thesis combines the results of magnetosheath fluctuation investigations from several separate but closely related studies. In Chapter 1, we define a present knowledge about solar-terrestrial coupling and discuss processes in the different sheaths. The aims of the thesis are presented in Chapter 2. In Chapter 3, we describe spacecraft measurements in the solar wind and sheaths and used data sets and correlation methods for an analysis of magnetic field and plasma fluctuations. Since the coupling between the solar wind and the magnetosphere is controlled by the IMF orientation, Chapter 4 contains a study of an estimation of reliability of prediction of the magnetosheath B_Z component from interplanetary magnetic field observations. Consequently, in the last part of the thesis (Chapter 5), we consider MHD properties of plasma and magnetic field fluctuations in the Earth's magnetosheath and other sheaths where high-time resolution plasma data are available. We compare correlations of fluctuations of the plasma density and magnetic field strength using methods described in Chapter 3.

This thesis was prepared under a support of the Research Plan MSM 0021620860 that is financed by the Ministry of the Education of the Czech Republic.

I declare that I carried out this doctoral thesis independently, and only with the cited sources, literature and other professional sources.

I understand that my work relates to the rights and obligations under the Act No. 121/2000 Coll., the Copyright Act, as amended, in particular the fact that the Charles University in Prague has the right to conclude a license agreement on the use of this work as a school work pursuant to Section 60 paragraph 1 of the Copyright Act.

In Prague, June 2011 Olga Gutynska

Abstract

Title: *Correlation properties of magnetosheath fluctuations*

Author: *Olga Gutynska*

Department: *Department of Surface and Plasma Science*

Supervisor: *Prof. RNDr. Jana Šafránková, DrSc.*

e-mail address: *Jana.Safrankova@mff.cuni.cz*

Abstract: *This thesis deals with fluctuations of the magnetic field (MF) and plasma density in different magnetosheath locations. The statistical study of the correlation length of these quantities has shown that these lengths are surprisingly low for both the ion flux and MF (approx. 1 R_E). However, the correlation length increases with an increasing correlation between the magnetosheath and interplanetary magnetic fields (IMF). Further, we have found that the correlation length of MF fluctuations depends on the solar wind speed, on a correlation between IMF and magnetosheath MF fluctuations, and on the amplitude of fluctuations. The statistical study of radial profiles of cross-correlations between MF and plasma density at the subsolar and flank regions based on Cluster and THEMIS magnetosheath observations revealed better correlations toward the magnetopause. A study of the modification of the IMF direction in the magnetosheath has shown that a reliable prediction of the magnetosheath B_Z sign requires $|IMF\ B_Z| > 2\ nT$ and that this prediction is more precise during solar minimum. Finally, we compared fluctuations in different sheaths: 1) slow or mirror wave modes prevail in all sheaths except the heliosheath; 2) correlated variations of the magnetic field and plasma density increase with the distance from the Sun; 3) the typical cross-correlation coefficients are ~ 0.3 in the Earth's magnetosheath; ~ 0.9 in the sheaths of magnetic clouds; ~ 0.5 in the Jupiter's magnetosheath; and ~ 0.6 in the heliosheath.*

Keywords: *heliosheath, planetary sheath, magnetosheath, magnetic field, plasma, fluctuations, correlation analysis*

Abstract

Název práce: *Korelačí vlastnosti fluktuací v přechodové oblasti*

Autor: *Olga Gutynská*

Katedra: *Katedra fyziky povrchů a plazmatu*

Vedoucí disertační práce: *Prof. RNDr. Jana Šafránková, DrSc.*

e-mail address: *Jana.Safrankova@mff.cuni.cz*

Abstract: *Disertační práce je věnována fluktuacím magnetického pole a koncentraci iontů v různých částech přechodových oblastí. Statistická studie korelační délky těchto veličin ukázala, že jejich vzájemná korelace je překvapivě nízká (v rádu 1 R_E), avšak tato délka se zvětšuje, pokud jsou korelovány změny meziplanetárního magnetického pole a magnetického pole v přechodové oblasti. Dále jsme prokázali, že korelační délka fluktuací magnetického pole závisí na rychlosti slunečního větru, na stupni korelace mezi fluktuacemi ve slunečním větru a přechodové oblasti a na amplitudě fluktuací. Statistická studie radiálních profilů křížové korelace mezi magnetickým polem a koncentrací iontů založená na rozsáhlém souboru dat z projektů THEMIS a Cluster lokalizovaných v různých místech přechodové oblasti dokázala, že korelace mezi oběma veličinami se zvyšuje směrem k magnetopauze. Studie zachování orientace B_Z složky meziplanetárního magnetického pole v přechodové oblasti, což je základem studií mnoha procesů na magnetopauze, naznačila, že pravděpodobnost pozorování stejné orientace ve slunečním větru a v přechodové oblasti vyžaduje, aby hodnota této složky (bez ohledu na znaménko) byla větší než 2 nT, jinak je pravděpodobnost jejího zachování velmi malá. Pravděpodobnost se dále mění v průběhu slunečního cyklu (pro sluneční maximum je nižší). Závěrem jsme porovnávali vlastnosti fluktuací magnetického pole a koncentrace iontů v přechodových oblastech planet, magnetických oblaků a heliosféře a našli jsme, že: 1) pomalé vlny dominují ve všech přechodových oblastech kromě heliosféry, 2) korelace mezi oběma veličinami se zvyšuje se vzdáleností od Slunce a 3) typické korelační koeficienty jsou ~ 0.3 v přechodové oblasti Země (na denní i noční straně), ~ 0.5 v přechodové oblasti Jupiteru, ~ 0.6 v heliosféře a ~ 0.9 v přechodové oblasti magnetických oblaků.*

Klíčová slova: *přechodová oblast v heliosféře, přechodová oblast planet, přechodová oblast Země, magnetické pole, plazma, fluktuace, korelační analýza*

Contents

Chapter 1

Introduction

1.1 The solar wind and the magnetosphere

1.1.1 The solar wind and the IMF

The solar wind (SW) is a stream of ionized particles, primarily electrons and protons, flowing outward from the Sun through the solar system. The existence of a SW had been known from comet observations in early 1950s but the properties were predicted theoretically by Parker in 1958 that were confirmed by the satellites Lunik III and Venus I in 1959 and by Mariner II in the early 1960s. *Parker* (1958) suggested that the corona could not remain in static equilibrium but must be continually expand. The main solution of the equation describing the expansion of the solar corona is presented in Figure 1.1, which shows the change in the rate of expansion with a heliocentric distance depending on the temperature isothermally isotropic corona.

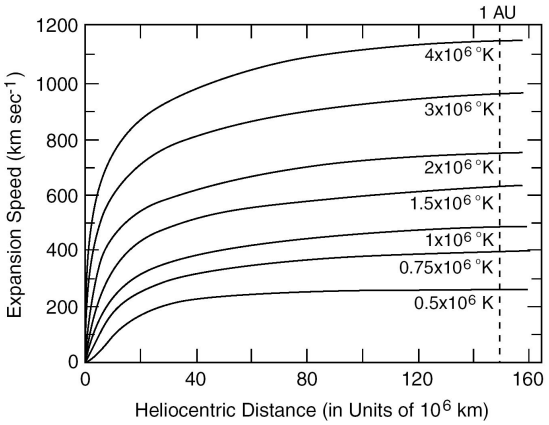

Figure 1.1: Profiles of the SW velocity for a values of the coronal temperature. Adapted from *Parker* (1958).

The expanding SW carries away the solar MF forming the IMF. The IMF

lines are frozen into the SW plasma. The SW moves out almost radially from the Sun, the rotation of the Sun leads to a spiral form of the MF. Figure 1.2 shows the spiral nature of the IMF. At the orbit of the Earth, the angle between the field

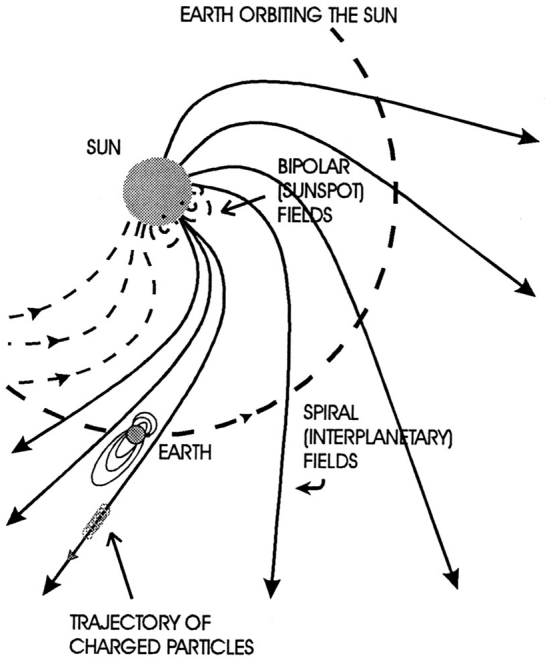

Figure 1.2: IMF as originating in the Sun and as deformed by the effects of the solar rotation and SW. Adapted from NASA/IPAC Extragalactic Database.

lines and the radial direction is about 45 degrees. Furthermore, sectors (typically four) with alternating inward and outward directed MFs can be identified.

The SW plasma consists mostly of hot electrons and protons with a minor fraction of He^{2+} ions and some other heavier ions (typically at high charge states). The Table 1.1 lists the basic SW characteristics.

Parameter	Minimum	Average	Maximum
Density (cm^{-3})	0.4	6.5	100
Helium %	0	5	25
Flow speed (km/s)	200	400	900
MF (nT)	0.2	6	80

Table 1.1: Average values of SW parameters observed near the orbit of the Earth.

1.1.2 Interaction of the IMF with the Earth's magnetosphere

A shock front called the bow shock (BS) is formed in the SW when the supersonic plasma emitted from the Sun interacts with the Earth's MF. The Earth's MF has

a dipole structure with a MF strength at the equator on the Earth's surface of about 30 000 nT, and at 10 Earth radius[1] (R_E) of about 30 nT.

The dipole MF of the Earth is an impenetrable barrier to the SW plasma which therefore is decelerated to a subsonic velocity and flows around the Earth. As first considered by *Chapman and Ferraro* (1931a,b), the dipole MF geometry interacting with the SW can be described using the mirror field method, in which a conducting plane representing the SW is replaced by an image of the dipole located symmetrically with respect to the plane (Figure 1.3a). As a result of that mirror method it would be to compress the terrestrial field on the right hand side (in Figure 1.1a) of the conducting plane. Eventually, as sketched in Figure 1.3b, the solar plasma would surround the dipole field forming a bullet-shaped plasma cavity.

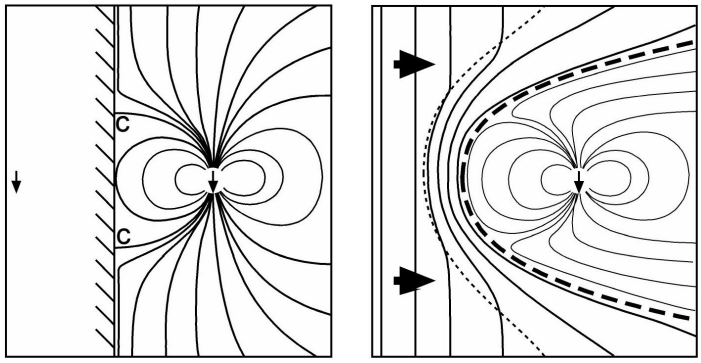

Figure 1.3: (a) Disturbed dipole field geometry in the mirror method. Adapted from *Chapman and Bartels* (1941). (b) Formation of the bullet-shaped magnetosphere in the moving SW.

Due to the frozen-in condition, the interplanetary and terrestrial MFs cannot mix and a discontinuity surface, the magnetopause (MP), develops between the two fields (the thick dashed line in Figure 1.3b). Furthermore, as the SW streams at a much higher speed than that at which information is conveyed within the plasma, a shock front develops around the MP. Ahead of the MP, there is formed the deflected flow where the SW plasma is heated and slowed from supersonic to subsonic speeds called the magnetosheath (MSH). In the anti-sunward direction, the Earth's MF is confined in a comet-like cavity, the magnetosphere. The BS (thin dotted line in Figure 1.3b) separates the undisturbed SW from the shocked SW, the MSH. The SW compresses the magnetosphere at the sunward side, so that the dayside MP is located roughly at 10 R_E distance from the center of the Earth. In the nightside, interaction with the SW stretches the magnetosphere forming a long tail (hundreds of R_E's). Figure 1.4 shows a sketch of the SW - Earth interaction and the main boundaries.

[1] 1 R_E = 1 Earth's radius, ~6371,2 km

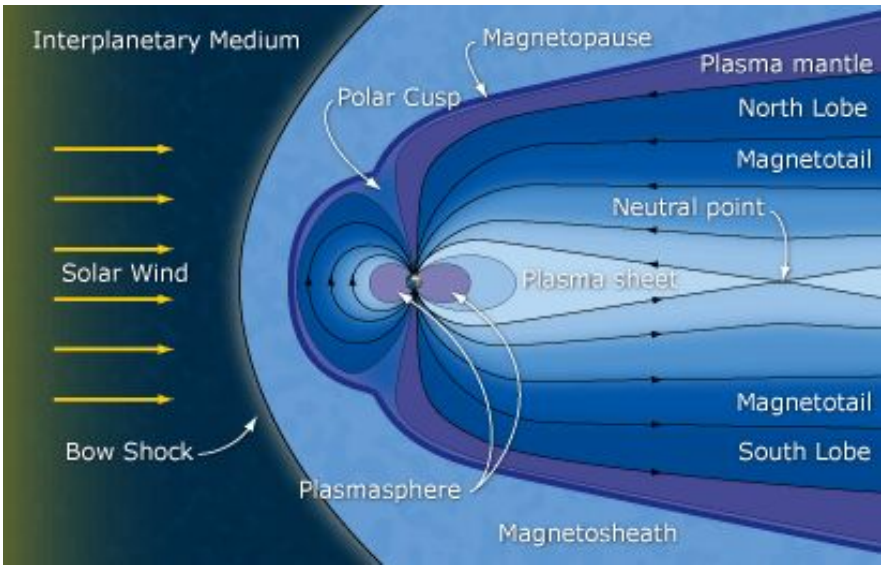

Figure 1.4: Earth's magnetic environment Illustration of Earth's magnetic environment, with key regions indicated. Adapted from The European Space Agency.

Although the mirror field method was the first step in describing the Earth's magnetic field geometry in space, some of its predictions are still valid. For example, a current system develops on the MP, with a purpose of shielding out the magnetospheric MF from the SW. These currents are today called the Chapman-Ferraro currents. Furthermore, the mirror analogy yields two singular field lines, labeled with C in Figure 1.3a. Because plasma can freely moves along magnetic field lines, these singular field lines mapping to the MP, thus offer a location where the MSH matter can enter the magnetosphere. These field lines mark the magnetospheric cusp regions, although in reality, the cusps are more like horns of a finite width rather than singular field lines.

1.2 Magnetosphere models

Earlier magnetospheric studies concentrate mainly on large scale phenomena and processes. This preference led to a promotion of magnetohydrodynamic (MHD) equations to investigate the dynamics of magnetospheric plasmas. A number of useful concepts were developed. These include a conception of magnetospheric convection, the general shape of the magnetosphere, and their dependence on the upstream SW conditions. The simplifying assumptions adopted by MHD equations have both advantages and disadvantages. On the one hand, they allow to obtain understanding of magnetosheric phenomena even with rather limited survey of studied regions as well as positions of the magnetospheric boundaries. However, they exclude more advanced understanding on the exact nature and the complexities involved in a number of magnetosheric plasma processes which may

have global consequences.

1.2.1 Global MHD models

At present stage, many magnetospheric models are developed and in many of them we are confronted with problems for which solutions lie beyond the MHD descriptions. However, in practical observations, we can only compare data obtained from different spacecraft with predicted scenarios.

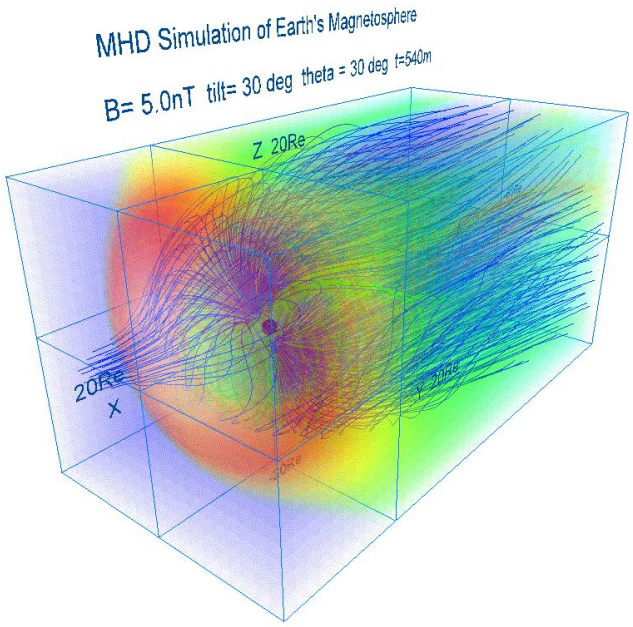

Figure 1.5: 3-dimensional configuration of the MF lines, plasma temperature and plasma flow in the Earth's magnetosphere with a dipole tilt of 30 degrees shown by Virtual Reality Modeling Language when the IMF is northward and duskward. Adapted from Solar-Terrestrial Environment Laboratory, Nagoya University.

Figure 1.5 shows the MF lines from a global MHD simulation of the interaction of the SW and the Earth's magnetosphere for the dipole tilt of 30 degrees when the IMF is northward and duskward. In this plot, the inner field lines close within the simulation box (both ends of the field go into the Earth), while the outer field lines extend to the back of the simulation box. The magnetosphere is bullet-shaped, and the magnetic null points occur at about 72° latitude (*Ogino et al.*, 1992). MHD models such as that shown here are very useful for describing the magnetic configuration and the flow around it. However, they have significant limitations. Because the plasma is assumed to be a magnetized fluid, the models do not simulate kinetic effects and the plasma instabilities that could arise. The parameters must be chosen for numerical stability rather than on the basis of physical constraints. Moreover, the spatial resolution often is too coarse to describe the phenomena of interest accurately. Hence, other techniques

have been developed to address these problems. The hybrid technique treats ions as particles and electrons as a massless fluid in order to include some of the kinetic effects in a plasma. At the other extreme, gas-dynamic simulations have been used for situations in which the magnetic forces can be neglected, so that increased spatial resolution and faster computational speed can be obtained. Gas-dynamic simulations have been employed since the mid-1960s in studying the SW interaction with the magnetosphere and have been very influential in guiding our understanding of this problem.

1.2.2 The gas-dynamic model

Estimates of the global plasma properties in the MSH are predominantly based on the results of the gas-dynamic model predictions of *Spreiter et al.* (1966). This model ignores all magnetic forces on the flow. It calculates MF lines by convecting the field lines along with the fluid. In this model, the flow is cylindrically symmetric about the Sun-Earth line. The results of the simulations depend on the shape of the obstacle, the Mach number, M_{SW} of the flow, and the polytropic index γ. The value of SW Mach number is equal to the Mach number of the magnetosonic wave because the BS is a fast magnetosonic shock. The polytropic index is usually equal to $\frac{5}{3}$, which is convenient for a gas with three degrees of freedom.

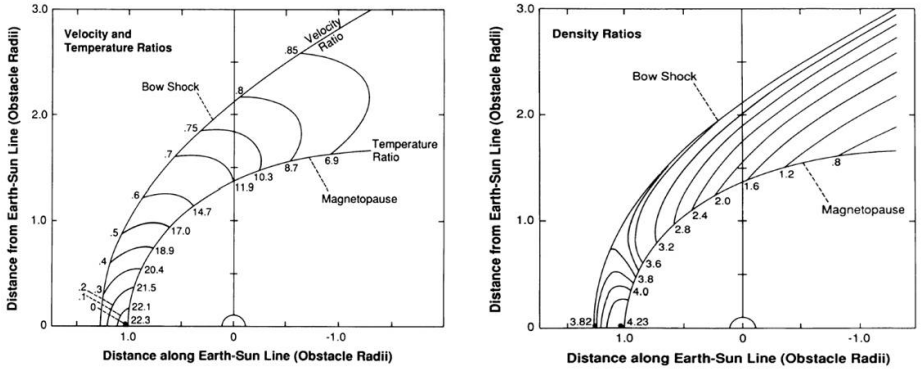

(a) (b)

Figure 1.6: Velocity and temperature (a) and density (b) contours for supersonic flow past the magnetosphere (for M=8, γ=2). Adapted from *Spreiter et al.* (1966).

Figures 1.6a, b show the lines of constant velocity, temperature and density in the MSH normalized by the upstream SW value. The streamlines show the direction of the flow. The density ratio behind the shock is close to the maximum as it compressed in this region. The temperature concurs with velocity in Figure 1.6b, because the temperature ratio is related to the velocity ratio by the expression:

$$\frac{T}{T_{SW}} = 1 + \frac{(\gamma - 1)\, M_{SW}^2}{2} \left(1 - \frac{V^2}{V_{SW}^2}\right), \tag{1.1}$$

which is obtained by integrating the energy equation (*Spreiter et al.*, 1966).

In the model, the SW flows along the Sun-Earth line, strikes the subsolar MP and then is diverted radially from this point. The model further predicts that velocities decrease from the BS to the MP, whereas the density and temperature increase in the vicinity of the stagnation streamline. Farther from the subsolar region, the density and velocity decrease but the temperature increases through radial profiles from the BS to the dayside MP. Along the flanks of the near-Earth magnetotail, minimum velocities and maximum temperatures occur in the middle MSH. The plasma flowing radially away from the stagnation streamline accelerates up to the SW speed and becomes increasingly like SW toward the flanks, where the BS is weaker.

These predictions were generally confirmed by experimental studies. However, it has many limitations. In particular, it predicts a density and MF increases at the MP which is not observed. Moreover, the gas-dynamic model cannot account for MHD waves. Another limitation of these techniques is their assumption of isotropic pressure. Finally, the gas-dynamic approach does not simulate small-scale features of the gyroradius or smaller size. At the BS, these have been found to be of critical importance in providing the dissipation required by the Rankine-Hugoniot equations. These processes may have equal import at the MP.

1.2.3 MHD simulations

Zwan and Wolf (1976) used the results of the *Spreiter et al.* (1966) model at the BS and the MP and provided a formulation and numerical estimation of the MSH flow using a MHD approach. Their model describes a magnetic flux tube moving from the BS to the MP and predicted an increase of the magnetic field strength which is coupled with a plasma depletion. Both a diversion of the flow at the BS along the magnetic field direction and a squeezing effect close to the MP where flux tubes pile up are found to lead to a density depletion at the MP. The result is a net density decrease in regions where the deceleration of the flow is not efficient and diversion of the flow dominates.

Wu (1992) made numerical simulations of the MSH profile using a 3-D MHD calculation, taking into account the formation of a plasma depletion layer. In this model, the magnetosphere is a solid impermeable obstacle. The density increases first and then decreases from the bow shock toward the MP along the Sun-Earth line. In the inner MSH, the decrease with distance from the MP is more abrupt than the increase in density within the outer MSH.

Song et al. (1999a,b) have carried out comparisons of observations and MHD models. The authors discovered a region of a plasma density enhancement and magnetic field depression in the inner MSH and attributed it to a slow-mode

standing wave. *Siscoe et al.* (2002) discussed some aspects of the MSH flow if magnetic forces are included in the framework of ordinary gasdynamics (*Spreiter et al.*, 1966). The authors suggested four such aspects and illustrated them with computations using a numerical MHD code that simulates the global magnetosphere and its MSH. *Fuselier et al.* (2002) compared observations of MSH plasma in the high-altitude cusp with gas dynamic and MHD model predictions. They found that gasdynamic models over-estimate the flow velocity adjacent to the MP at high latitudes while MHD models which include the effects of magnetic reconnection predicted lower flow velocities than those observed in the same region. However, some limitation of these comparisons is that they are either based on a single case study or a small number of observations.

The Block-Adaptive-Tree Solar-wind Roe-type Upwind Scheme (BATS-R-US) uses approximate Riemann solvers based on the waves associated with the full magnetohydrodynamic system (*Powell et al.*, 1999). This model, due to the high-resolution approach, is second-order accurate in smooth regions, and locally first-order accurate in discontinuous regions. The code shares many characteristics with other global MHD models. Two features that set it apart are the use of an adaptively refined mesh, and its near-perfect scaling on massively parallel computers. These two features allow the model to be run at dramatically higher resolution than has been achieved to date in global MHD models.

Samsonov (2006) developed a MSH numerical MHD model which calculates SW flow around the MP for different IMF orientations. The author has found that the magnetic field magnitude and values of other MHD parameters in the MSH depend on the direction of the interplanetary magnetic field.

1.2.4 BS models

The position and shape of Earth's BS are dependent upon the shape and size of the MP obstacle and the condition of the impinging SW plasma (e.g., *Bennett et al.*, 1997; *Cairns and Lyon*, 1995; *Chapman and Cairns*, 2003; *De Sterck and Poedts*, 1999; *Fairfield*, 1971; *Fairfield et al.*, 2001; *Farris et al.*, 1991; *Merka et al.*, 2003a,b; *Peredo et al.*, 1995; *Russell*, 1985; *Russell and Zhang*, 1992; *Spreiter and Stahara*, 1985; *Spreiter et al.*, 1966; *Stahara*, 2002; *Verigin et al.*, 2001). In terms of MHD theory, the relevant SW parameters are the ram pressure $P_{ram} = \rho_{sw}\nu_{sw}^2$, Alfvén Mach number $M_A = \nu_{sw}/\nu_A$, sonic Mach number $M_S = \nu_{sw}/c_S$, fast magnetosonic Mach number $M_{ms} = \nu_{sw}/\nu_{ms}$, the magnitude of the upstream MF B_{IMF}, and θ_{IMF} (the angle between $\vec{v}_{sw}$ and $\vec{B}_{IMF}$). Here $\vec{v}_{sw}$, ρ_{sw}, ν_A, c_S, and ν_{ms} denote the SW velocity, mass density, Alfvén speed, sound speed, and fast mode wave speed, respectively. In the near-Earth region, the obstacle size and shape, P_{ram}, M_A, M_S, and θ_{IMF} all determine the location of the resulting shock. Far downstream of the Earth, M_{ms} effects dominate the position of the shock since the shock asymptotes to the fast mode Mach cone (e.g., *Petrinec and Russell*, 1997; *Verigin et al.*, 2003). At low Mach numbers (M_A, M_S, and M_{ms}),

the shock becomes weaker (smaller density jump), and the entire shock will be found farther from Earth so that flow deflection around the MP can still occur (e.g., *Fairfield*, 1971; *Farris and Russell*, 1994). Also, a decrease in M_A and/or M_{ms} (and thus M_{ms}) implies an increase in the ratios ν_A/ν_{sw}, and/or ν_S/ν_{sw} (and thus ν_{ms}/ν_{sw}), so that information is able to move farther upstream in the same number of nonlinear steepening times implying a more distant shock. It should be noted that in the SW frame, the shock propagates into the undisturbed medium at a velocity near -$\vec{v}_{sw}$.

In the near-Earth region (before the shock has asymptoted to the Mach cone), the shock has historically been modeled as a paraboloid or hyperboloid symmetric about the aberrated SW direction (e.g., *Cairns et al.*, 1995; *Farris et al.*, 1991; *Filbert and Kellogg*, 1979). For example, a paraboloid model is

$$x = a_s - b_s r^2, \tag{1.2}$$

where $r = \sqrt{y^2 + z^2}$, (x, y, z) are aberrated GSE coordinates, the Earth is at the origin, and a_s and b_s are the shocks standoff distance from Earth (measured along the x-axis) and the flaring parameter, respectively. However, the shock is formed via the steepening of fast magnetosonic waves with a characteristic wave speed,

$$\nu_{ms}^2 = \frac{1}{2}\left[c_S^2 + \nu_A^2 + \sqrt{\left(c_S^2 + \nu_A^2\right)^2 - 4c_S^2\nu_A^2 cos^2\theta_{bn}}\right]. \tag{1.3}$$

Here θ_{bn} denotes the angle between the local shock normal $\vec{n}$ (parallel to the wave vector) and $\vec{B}_{IMF}$.

The fast mode speed is maximum when $\vec{B}_{IMF}$ is perpendicular to $\vec{n}$, and minimum when $\vec{B}_{IMF}$ is parallel to $\vec{n}$. Accordingly, the shock should be found farther from Earth when $\vec{B}_{IMF}$ is perpendicular to $\vec{n}$ with $\nu_{ms}^2(90°) = c_S^2 + \nu_A^2$ and closer to Earth when $\vec{B}_{IMF}$ is parallel to $\vec{n}$ with $\nu_{ms}^2(0°) = max(c_S^2, \nu_A^2)$. For all other angles of θ_{bn} the magnitude of ν_{ms}^2 will lie somewhere between. Since $\vec{n}$ varies in direction around the shock surface, this effect should lead to the shock being tilted or skewed toward being symmetrical about the direction parallel to $\vec{B}_{IMF}$ rather than parallel to $\vec{v}_{sw}$, as illustrated in Figure 1.7 (*Chapman and Cairns*, 2003).

At present time, many BS models (mainly empirical) have been developed. *Merka et al.* (2003a) made a comparison review of BS models comparing their predicted shock radial distances with observed crossings registered by IMP 8 (totally 2293 BS crossings). For this study they have chosen the Formisano model (*Formisano*, 1979) (referred as F79), Němeček and Šafránková (NS91) (*Nemecek and Safrankova*, 1991), Farris and Russell (FR94) (*Farris and Russell*, 1994), Cairns and Lyon (CL95) (*Cairns and Lyon*, 1995) and Peredo et al. (P95) (*Peredo et al.*, 1995) models to comparisons with observed BS crossings. Table 1.2 shows the basic properties of these models.

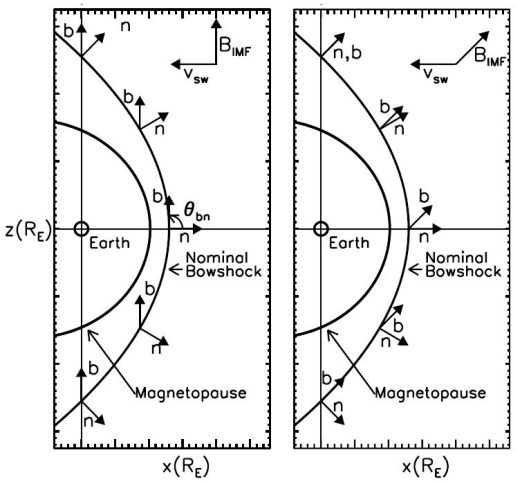

Figure 1.7: Illustration of the shock geometry showing the local shock normal **n**, vectors **b** (parallel to B_{IMF}), and θ_{bn}; $\theta_{IMF} = 90°$ (left); oblique orientations $0° < \theta_{IMF} < 90°$ (right). Adapted from *Chapman and Cairns* (2003).

In these models, the BS has been approximated using ellipsoidal, paraboloidal or hyperboloidal surfaces with varying standoff distances under assumption that both position and shape can be expressed as a function of upstream plasma parameters (usually by the dynamic pressure of the incoming solar wind and by upstream Mach numbers). *Merka et al.* (2003a) have shown that the NS91 model is nearly independent on the variations of IMF and its components as well as on extreme values of SW parameters and provides the best results in a broad range of upstream parameters.

Jeřáb et al. (2005) suggested a correction to the NS91 model. Since this model was used in our work for determination of the BS locations, a brief description is presented.

After all corrections, the BS model can be written in the form

$$R(\theta,\phi) = \frac{R_{av}(\theta,\phi)}{R_0} \cdot \frac{C}{(NV^2)^{1/6}} \cdot \left(1 + D\frac{(\gamma-1)M_A^2+2}{(\gamma+1)(M_A^2-1)}\right), \tag{1.4}$$

where $R(\theta,\phi)$ is given by equation

$$a_{11}X^2 + a_{22}Y^2 + a_{33}Z^2 + a_{12}XY + a_{14}X + a_{24}Y + a_{34}Z + a_{44} = 0, \tag{1.5}$$

where X, Y, and Z are GSE coordinates (in R_E) of the surface. The coefficients of the best single-surface fit are

$$\begin{aligned} &a_{11} = 0.45; a_{22} = 1; a_{33} = 0.8; a_{12} = 0.18; \\ &a_{14} = 46.6; a_{24} = -2.2; a_{34} = -0.6; a_{44} = -618, \end{aligned} \tag{1.6}$$

and the D parameter and constant C are

$$D = 0.937 \times (0.846 + 0.042|B|); C = 91.55. \tag{1.7}$$

Model	Reference Frame	Symmetry	Parameters
F79	GSE	north-south	P_{sw}
NS91	GSE	north-south	P_{sw}, B, M_{MS}
FR94	SW flow	axial	P_{sw}, B_z, M_{MS}
FR94c	SW flow	axial	P_{sw}, B_z, M_{MS}, R_c
CL95	SW flow	axial	P_{sw}, B_z, M_A, M_S, θ
P95	GIPM	north-south	P_{sw}, B_y, B_z, M_A

Table 1.2: An overview of the BS model basic properties for such parameters: SW dynamic pressure (P_{sw}); IMF magnitude (B) and its components (B_y, B_z); upstream sonic (M_S), Alfvénic (M_A) and magnetosonic (M_{MS}) Mach numbers; obstacle's curvature radius (R_c); and the angle between $\vec{v}_{sw}$ and $\vec{B}(\theta)$. Adapted from *Merka et al.* (2003a).

1.2.5 MP models

The most fundamental mode of interaction between the SW and the Earth's magnetosphere can be described as a compression of the Earth's dipole MF by the external SW plasma until pressure balance is achieved between the internal magnetosphere field and the exterior SW plasma with a outer boundary called the MP. Sudden SW pressure increases associated with interplanetary shocks are known to move the MP inward and further enhance the strength of the magnetosphere field (e.g., *Baumjohann et al.*, 1983; *Smith et al.*, 1986; *Wilken et al.*, 1982).

Various models for the size and shape of the MP have been developed (*Fairfield*, 1971; *Formisano*, 1979; *Howe and Binsack*, 1972; *Petrinec and Russell*, 1993, 1996; *Petrinec et al.*, 1991; *Roelof and Sibeck*, 1993; *Shue et al.*, 1997; *Sibeck et al.*, 1991). The *Howe and Binsack* (1972) and *Petrinec and Russell* (1996) models of the nightside MP use inverse trigonometric functions to describe the MP size and shape. The other models use either the general equation of an ellipsoid with two parameters (eccentricity and standoff distance) or the general quadratic equation. *Fairfield* (1995) discussed the limitations of using an elliptic equation.

Boardsen et al. (2000) presented an empirical model for the shape of the near-Earth high-latitude MP where they added a new parameter - dipole tilt angle. A new three-dimensional asymmetric MP model uses as a parameters the SW dynamic and magnetic pressures, the IMF B_Z, and the dipole tilt angle was developed by *Lin et al.* (2010). Recently, *Dušík et al.* (2010) discuss the influence of IMF cone angle on the MP locations and found that *Petrinec and Russell* (1996) and *Shue et al.* (1997) empirical models underestimate the dependence of MP locations on upstream dynamic pressure (D_p).

For determination of MP locations in our work, we use the *Shue et al.* (1997) model. *Shue et al.* (1997) made a statistical study of *in situ* MP crossings observed by ISEE 1 and 2, AMPTE/IRM, GOES 2, 5 and 6 (totally 553 crossings) and

obtained a quantitative relation between the size and shape of the MP and the upstream SW D_p and IMF B_z, observed by ISEE 3 and IMP 8. They proposed a new function which had the flexibility to describe the open or closed MP:

$$R = R_0 \left(\frac{2}{1 + cos\theta} \right)^{\alpha}, \tag{1.8}$$

where R is the radial distance at an angle (θ) between the Earth-Sun line and the direction of R, and R_0 is the standoff distance

$$R_0 = \begin{cases} (11.4 + 0.13B_z)(D_p^{-\frac{1}{6.6}}), & \text{for } B_z \geq 0 \\ (11.4 + 0.14B_z)(D_p^{-\frac{1}{6.6}}), & \text{for } B_z < 0, \end{cases} \tag{1.9}$$

α is the level of tail flaring defined as:

$$\alpha = (0.58 - 0.01B_z)(1 + 0.01D_p). \tag{1.10}$$

1.3 The Earth's MSH

1.3.1 MSH properties

The interaction of the supermagnetosonic SW flow with the Earth's MF forms a magnetospheric cavity bounded by the BS and MP. The layer between these two surfaces known as the magnetosheath enables the incident SW flow reduced to submagnetosonic speeds by the shock to be diverted around the magnetosphere. The observed MSH plasma parameters show both large scale spatial ordering, imposed by the shape of the MP, and variability dependent on the SW input. Because the nature of the BS depends on the orientation of the IMF with respect to the local BS normal (θ_{BN}), the processes in the MSH plasma just behind the BS depend also on whether the shock is quasi-perpendicular or quasi-parallel. The plasma properties of the MSH are influenced by the upstream SW including density, velocity, β and M_A.

The average MSH features have been documented based on data from several missions as ISEE 1 and 2 (e.g., *Kivelson and Russell*, 1995), AMPTE-IRM (*Hill et al.*, 1995; *Li et al.*, 1995; *Phan et al.*, 1994), and Wind (*Phan et al.*, 1996, 1997). MSH plasma is characterised by the following:

- its average density and MF strength are higher than in the upstream SW by a factor consistent on average with the Rankin-Hugoniot relation for the fast mode shock;

- the average flow direction deviates from the anti-solar direction such that the plasma flows around the blunt magnetosphere;

- the velocity downstream of the BS is lower than the local fast magnetosonic speed;
- the flow velocity increases again to supersonic speeds around the MP flanks;
- the ion temperature of the sheath is higher than in the SW while the electron temperature does not increase very much over its upstream value, such that the ion to electron temperature ratio in the sheath is of order 6-7;
- the plasma β shows large variations from the order of unity to values much greater than one;
- the MSH plasma develops a pronounced temperature anisotropy ($T_\perp > T_{||}$) behind the BS that increases toward the MP and is more pronounced in the ions than in the electrons.

From this follows that the MSH seems to develop two regions of different turbulent behavior: one behind the BS and the other closer to the MP.

Statistical studies of the MSH structure and plasma parameters based on several years of observations in the MSH flanks, both in night and dayside have been carried out using the INTERBALL-1 (IB-1) data by *Šafránková et al.* (2005) and *Němeček et al.* (2000b,c, 2002) using data from IMP 8 at the $-15 < X_{GSE} < -20R_E$ slice and SW data from ISEE 1, ISEE 3 and WIND (*Paularena et al.*, 2001), and using four years of Cluster orbital coverage (*Longmore et al.*, 2005, 2006). These studies resulted in a consistent picture of average parameters in the near-Earth MSH under various upstream conditions.

1.3.2 Sources of turbulence and low-frequency waves

The MSH is typically a high-β, anisotropic environment. Particle reflection at the BS and the ion foreshock provide upstream sources of turbulence and free energy to drive local instabilities. On the other hand, MF line draping and compression at the MP provide sources of free energy which are able to influence the local plasma and turbulence in the MSH (e.g., *Savin et al.*, 2002, 2004, 2001). Thus, the result is a turbulent MSH with significant power over a wide range of the low-frequency spectrum (see e.g., review of *Schwartz et al.* (1996)).

Luhmann et al. (1984) studied the spatial distribution of MSH MF fluctuations and they have shown that the amplitude of these fluctuations is controlled by the IMF direction being larger behind the quasi-parallel BS. In general, the MSH tends to be in a more turbulent state behind the spatially extended quasi-parallel BS.

A comprehensive study of ion flux fluctuations in the MSH by *Němeček et al.* (2001) has shown that the fluctuations are larger (1) behind the quasi-parallel BS, (2) closer to the MP, and (3) during intervals of the radial IMF. Moreover,

they have shown that a part of MSH fluctuations is of SW origin, whereas another part is generated at the BS and/or in the MSH proper.

Blanco-Cano et al. (2006) performed global hybrid simulations and studied foreshock morphology and its influence on the BS and MSH. The authors confirmed earlier expectations that downstream from the shock, the MSH is permeated by a variety of waves that result from the convection of upstream waves and also from local wave generation. The wave characteristics are different in the quasi-parallel and quasi-perpendicular parts of the MSH.

A similar finding follows from the papers by *Shevyrev and Zastenker* (2005), and *Shevyrev et al.* (2006). The authors concluded that in the MSH, the plasma flow is mainly turbulent and that the character of the turbulence is strongly controlled by the θ_{BN} angle. Behind quasi-parallel shocks, they observed different types of MHD-wave modes and variations of the ion flux and MF increase. On the other hand, behind the quasi-perpendicular BS, they observed sometimes mirrormode waves in the middle of the MSH and near the MP. Moreover, *Shevyrev and Zastenker* (2005) analyzed power spectra of plasma and MF fluctuations upstream and downstream separately for quasi-parallel and quasi-perpendicular BS conditions and suggested that these fluctuations are not born in the foreshock region but they are generated at the BS itself. On the other hand, *Constantinescu et al.* (2007) found a high concentration of low-frequency wave sources in the electron foreshock and in the cusp region.

According to e.g., *Schwartz et al.* (1996), two wave modes dominate the MSH, and grow there owing to the ion $T_{\perp} > T_{||}$ anisotropy (*Denton*, 2000). The Alfvén ion cyclotron (AIC) mode grows under modest β condiconditions, and is found behind the weaker quasi-perpendicular BSs and in the plasma depletion layer. Ion cyclotron waves typically have phase velocities close to the Alfvén speed and propagate away from their source region. At higher β, for instant, behind strong quasi-perpendicular BSs and in the middle MSH, the zero-frequency compressive mirror mode dominates the power spectra at low frequencies. Mirror instability generates large amplitude, anti-correlated variations in the MF magnitude and plasma density which are non-propagating in the plasma frame. These structures can act as magnetic bottles, trapping part of the particle distribution (e.g., *Kivelson and Southwood*, 1996). A modified version of the mirror mode, with finite frequency and propagation speed, appears to exist downstream of the slow mode transition close to the subsolar MP. However, several aspects complicate the mode identification: (1) There is usually a mixture, possibly phase coherent, of modes and/or frequencies, rather than an isolated mode. (2) Frequencies are often Doppler shifted by an unknown amount. (3) Wave vectors are often difficult to determine from the one (or few) point measurement available from the spacecraft. (4) The mode eigenstate can depend on the wave vector, plasma β, and temperature anisotropy, as well as on the contributions of multispecies or non-Maxwellian kinetic features. The result is that both the background state and fluctuations are not accurately known.

Numerous studies have been dedicated to the origin and nature of plasma waves in the MSH and its adjacent regions.

In *Zastenker et al.* (1999), the middle-scale (from minutes to hours) variations of the ion flux and MF magnitude were investigated in middle- and high-latitude MSH regions near terminator. As a summary, the authors considered a portion of observed variations is the structures originating in the subsolar region and propagating downstream with the MSH speed. *Zastenker et al.* (2002) discuss the origin of MSH variations and show that a part of variations is repetition or amplification of SW or IMF disturbances which pass through the BS and a part of variations originates inside the MSH. For very close (about 0.3 R_E) spacecraft, the authors observed the absence of correlation for 5-20 s variations but rather good correlations for about 3-min variations. On the other hand, they observed poor correlations between two well-separated (about 4 R_E) spacecraft for 3-5 min variations but good correlations for longer (20-30 min) variations. From these, the authors suppose that the persistent time of MSH variations is roughly by an order of the magnitude larger than the period of variations.

Zwan and Wolf (1976) referred to the slow-mode processes inherent to magnetized fluids and found a depletion effect for plasma near the MP. *Song et al.* (1990, 1992b) discovered a region of plasma density enhancement and MF depression in the inner MSH and attributed it to a slow-mode standing wave. In their MHD simulations, *Lee et al.* (1991) showed that such structure can be formed close to the subsolar stagnation region. *Southwood and Kivelson* (1992) suggested that slow-mode structures can create disturbances at the MP.

Song et al. (1990, 1992a,b) showed evidence of a standing slow mode wave in front of the MP over which higher-frequency mirror modes convected with the MSH flow are superposed. *Hubert et al.* (1998) suggest that the distance from the BS is a key parameter determining the nature of plasma waves. They found compressive and AIC modes from the ramp to the undershoot of an oblique shock, pure AIC waves in the outer MSH, a mixture of AIC and mirror modes close to the shock and in the middle MSH, pure mirror modes in the inner MSH, and distorted mirror modes (observed also by *Denton et al.* (1995)) close to the MP, while *Lacombe et al.* (1992) detected Alfvén and mirror modes in the vicinity of the BS.

Schäfer et al. (2005) identified different MSH wave populations and found a multiplicity of standing structures (mirror modes) convected with the plasma flow and a large number of Alfvénic waves. The results confirm previous MSH wave studies (e.g., *Denton*, 2000) but the authors also discuss a small number of mirror mode-like waves that have propagation speeds up to the local Alfvén velocity, quasi-perpendicular to the magnetic field.

Lucek et al. (1999) observed mirror modes in approximately 30% of MSH passes of Equator S throughout the whole MSH under a variety of upstream SW conditions.

Tátrallyay and ErdőS (2002) identified mirror-type fluctuations in MF data

from the ISEE 1/2 spacecraft in different regions of the MSH and concluded that these fluctuations do not always originate near the BS but that the source may be somewhere else (e.g., at the MP, inside the MSH, or in localized regions of the BS). A detailed four-point Cluster study of mirror type MF fluctuations by *Tátrallyay et al.* (2008) reveals that these fluctuations decrease in the inner regions of the MSH, indicating some saturation in the growth of the waves when proceeding toward the MP. The results suggest that mirror type fluctuations originate from the compression region downstream of the quasi-perpendicular BS and that the growth of the fluctuations cannot be described by linear approximations.

Narita and Glassmeier (2005) used MF data from Cluster spacecraft to determine the wave vectors across the MSH. The multipoint measurements allowed for Doppler correction and for the determination of the dispersion relation and the wave mode identification. They found a mixture of ion cyclotron and mirror modes close to the shock, then a region where mirror modes were dominating and finally, close to the MP they found distorted mirror modes.

The direction of propagation of low-frequency waves (drift mirror and mirror mode waves) in the MSH was studied by *Narita and Glassmeier* (2006). The authors found that the anti-sunward propagation (in the plasma frame) dominates. At the smaller zenith angles, the propagation is toward the MSH flank, and at the larger angles, it is toward the MP. As continuation of this study, *Narita et al.* (2006) conclude: the spatial pattern of wave propagation directions indicates that propagation is outward divergent in the upstream region, inward divergent in the MSH near the subsolar MP, and inward convergent at the MSH flank. The divergent pattern in the MSH indicates that the waves propagate along the plasma stream lines, following the refraction of the plasma flow at the shock. The convergent pattern in the MSH flank is consistent with the perpendicular propagation in the draped MF.

1.3.3 Mirror mode theory

Mirror mode waves as they described in Section 1.3.2 frequently occur in the MSH under conditions of enhanced ion temperature anisotropy ($T_\perp > T_{||}$) and high $\beta_{\perp i} \sim 2$. They are non-propagating magnetic bottle structures, characterised by large amplitude variations in the MF magnitude, $\Delta B/B \sim 1$, anti-correlated with variations in the plasma number density introducing inhomogeneity into the plasma. Anticorrelation between MF and density perturbations is not unique to mirror modes. It is also typical of slow mode waves, and can lead to large amplitude soliton chains (as it has been shown by *Stasiewicz* (2004)), in which case no anisotropy is required. Such structures may appear in the solar wind. In the MSH, mirror modes are dominant because the presence of the large anisotropy and high plasma temperature damps slow mode waves.

The existence of mirror modes was predicted by *Rudakov and Sagdeev* (1961) and *Chandrasekhar et al.* (1958) from an anisotropic plasma fluid theory followed

by kinetic approaches by *Tajiri* (1967), *Hasegawa* (1969), and *Pokhotelov and Pilipenko* (1976).

The starting point in a quasi-hydrodynamic approach is the pressure equilibrium condition for an anisotropic plasma

$$\delta p_\perp + \frac{B\delta B_{||}}{\mu_0} = -\frac{k_{||}^2}{k_\perp^2}\left[1 + \frac{1}{2}(\beta_\perp - \beta_{||})\right]\frac{B\delta B_{||}}{\mu_0}, \tag{1.11}$$

where $\delta p_\perp$ is the variation of the perpendicular plasma pressure, $B = |\vec{B}|$ is the magnitude of the ambient MF $\vec{B}$, $\delta B_{||}$ is the compressional magnetic field perturbation, $k_\perp$ and $k_{||}$ are the components of the wave vector $\vec{k} = (k_\perp, k_{||})$ perpendicular and parallel to the ambient field, respectively, and μ_0 is the free space permeability. The ratio of kinetic to magnetic energy density is given by $\beta = nk_B T/(B^2/2\mu_0)$, with indices $\perp$, $||$ indicating perpendicular or parallel pressures; n is the plasma number density. The perturbed quantities in Equation 1.11 are assumed to vary in both time and space as $\sim exp(-i\omega t + i\vec{k}\cdot\vec{r})$, where $\omega \ll \omega_{ci}$ is the wave frequency. The variation in the perpendicular plasma pressure is obtained from the perturbed particle distribution (*Pokhotelov et al.*, 2001)

$$\delta F_j = -\frac{\mu\delta B_{||}}{B}\frac{\partial F_j}{\partial \mu} + q_i\phi\frac{\partial F_j}{\partial W} - \frac{\omega(q_j\phi + \mu\delta B_{||})}{\omega - k_{||}\nu_{||}}\frac{\partial F_j}{\partial W}, \tag{1.12}$$

where $F_j(W,\mu)$ is the particle distribution function which depends on the energy, W, and magnetic moment, μ of the jth species of mass m_i, charge q_j and parallel speed $\nu_{||} = \sigma[2(W - \mu B)/m_j]^{\frac{1}{2}}$ ($\sigma\pm 1$ and indicates the direction of $\nu_{||}$). Here, ϕ is the scalar potential, with the wave electric field given by $E_{||}$=-$ik_{||}\phi$+$i\omega A_{||}$, $A_{||}$ being the parallel vector potential.

The ordinary ion-mirror mode is only one of the possibly unstable solutions of the dispersion relation (*Pokhotelov et al.*, 2003) resulting from a pressure balance and Maxwell's equations $D(\omega,\mathbf{k})\cdot\Psi$=0 for the wave field vector Ψ, whose components are

$$\Psi_{||} = A_{||} - \tfrac{k}{\omega}\phi, \quad \Psi_A = -\tfrac{k_\perp}{\omega}\phi, \quad \Psi_M = \frac{(\mathbf{k}\times\mathbf{A})_{||}}{k_\perp} - \tfrac{k_y\kappa_B}{k_\perp\omega}\phi. \tag{1.13}$$

The last term includes the background MF inhomogeneity $\kappa_B = |\nabla \ln B|$ which yields the drift frequency ω_D= $(k_y\nu_\perp^2/2\omega_{ci})\kappa_B$. The simplest case neglecting the drift frequency contributions and assuming two-component Maxwellian plasma with cold electrons yields the ordinary ion-mirror mode which becomes unstable when the pressure anisotropy $A \equiv p_\perp$ / $p_{||}$, satisfies

$$A - 1 > \beta_\perp^{-1}, \tag{1.14}$$

where $\beta_\perp$=$2\mu_0 nk_B T_{i\perp}/B^2$ is the perpendicular ion β, and the electrons do not play any role in the instability. The growth rate of this mode (*Hasegawa*, 1969)

is proportional to the ratio $(k_{||}/k_{\perp})^2$ where $(k_{||}/k_{\perp})^2 \ll 1$. The **k**- vector is thus nearly perpendicular to the MF and the mode has a small growth rate. However, because it is practically non-propagating and is therefore convected with the plasma flow, it has plenty of time to grow and so can reach large amplitudes which ultimately cannot be described by simple linear theory. In the limit of $T_e \to 0$, the theory predicts that the cold electrons will wipe out any parallel electric field and therefore that $k_{||}$ should be zero and the mode cannot exist. However, a small but finite temperature of the electrons will allow for the mode to exist in slightly oblique direction

The ordinary ion-mirror mode grows fastest (*Pokhotelov et al.*, 2004) at perpendicular wavelengths comparable to the ion gyroradius, $\mathrm{k}_{\perp}\rho_i \sim 1$. The above threshold for the short wavelength mirror mode is higher by a factor of 2 than in the very long wavelength case $\mathrm{k}_{\perp}\rho_i \ll 1$. Thus, depending on the anisotropy, the fastest growing waves will be those which have a wavelength just long enough for the anisotropy to exceed the instability threshold. The inclination of the mode with respect to the MF implies that the bottles are no longer symmetric around the field direction. Field aligned currents should flow within the structure, generating a non-coplanar MF component, which twists the mirror mode MF around the bottle.

The mirror mode is never observed in the state of linear small MF compressions. MF compression ratios of 30-80% are observed, deep in the nonlinear regime. Since the mode is non-oscillatory, it is unsurprising that a quasi-linear approach (*Treumann and Baumjohann*, 1997) does not explain the observations. That particle trapping occurs it has been suggested by *Kivelson and Southwood* (1996). Such trapping is inferred from lion roar excitation (*Treumann et al.*, 2000) and observation within mirror modes (*Baumjohann et al.*, 1999), as well as by direct electron observation (*Chisham et al.*, 1998). In the nonlinear marginally stable state, the mirror modes should evolve into three-dimensional cylindrical structures with zero parallel wave number extended along the ambient MF (*Treumann et al.*, 2004).

Constantinescu (2002) used the marginal mirror equilibrium condition to consider the stationary equilibrium state of a mirror bottle. A pressure equilibrium in the plasma reference frame is written

$$\nabla\left(p_{\perp} + \frac{B^2}{2\mu_0}\right) + \nabla\left[\left(p_{||} - p_{\perp} - \frac{B^2}{\mu_0}\right)\frac{\mathsf{B}}{B^2}\right] = 0, \tag{1.15}$$

where μ_0 is susceptibility, B MF strength, B is a tensor with elements $(\mathsf{B})_{ij} = B_i B_j$, and $p_{||}$ and $p_{\perp}$ are plasma pressure components. The temperature anisotropy in a bi-Maxwellian plasma is

$$A(\mathbf{r}) = \frac{T_{\perp}(\mathbf{r})}{t_{||}(\mathbf{r})} = \left[1 - \left(1 - \frac{1}{A_0}\right)\frac{B_0}{B(\mathbf{r})}\right]^{-1}, \tag{1.16}$$

where $A(\mathbf{r})$ and $B(\mathbf{r})$ are the final anisotropy and MF, and A_0 and B_0 are unperturbed anisotropy and MF. Equation (1.16) holds for 2 (*Lee et al.*, 1987) and 3 (*Constantinescu*, 2002) dimensions.

In cylindrical symmetry ρ,z,$\partial/\partial\varphi$ =0, one has $\mathbf{B}(\rho,z)=(B_0+\delta \mathrm{B}_z(\rho,z))\mathbf{e}_z$ + $\delta \mathrm{B}_\rho(\rho,\, z)\mathbf{e}_\rho$, leading to a set of Bessel differential equations

$$\rho^2 \frac{d^2}{d\rho^2}\delta B_\rho^n + \rho\frac{d}{d\rho}\delta B_\rho^n + \left[\left(\frac{n\alpha\rho}{L}\right)^2 - 1\right]\delta B_\rho^n = 0, \tag{1.17}$$

where α is a dimensionless parameter:

$$\alpha = \pi\sqrt{\frac{\frac{1}{2}\left(1-\frac{1}{A_0}\right)+\frac{1}{\beta_{0\perp}}}{A_0 - 1 - \frac{1}{\beta_{0\perp}}}} \tag{1.18}$$

and $\beta_{0\perp}$ is the plasma parameter, i.e., the ratio between the orthogonal plasma pressure, $\mathrm{p}_{0\perp}$ and the magnetic pressure, $\mathrm{B}_0^2/2\mu_0$.

The solution of Equation (1.17)

$$\left\{\delta B_\rho^n(\rho), \delta B_z^n(\rho)\right\} = \left\{\frac{i\pi}{\alpha}C_n J_1\left(\frac{n\alpha\rho}{L}\right), C_n J_0\left(\frac{n\alpha\rho}{L}\right)\right\} \tag{1.19}$$

holds for $\alpha^2 > 0$, and for physically realistic solutions $\mathrm{C}_{-n} = \mathrm{C}_n^*$. In terms of the initial anisotropy and plasma β this is equivalent to:

$$A_0 > 1 + \tfrac{1}{\beta_{0\perp}} \quad \text{or} \quad A_0 < \tfrac{\beta_{0\perp}}{\beta_{0\perp}+2}. \tag{1.20}$$

The first inequality in Equation (1.20) is the mirror instability condition, and the second the firehose condition (e.g., *Baumjohann and Treumann*, 1996).

Figure 1.8 shows the onion layer like structure of the MF of a mirror mode bubble. For values of ρ for which $J_1(\rho) = 0$, the field lines become straight lines on the surface of the cylinder, defining the boundary between two layers of an opposite curvature. The position of the first boundary, which defines the main structure, is given by the ratio of radius to length of the central bubble

$$\alpha R/L = 3.832, \tag{1.21}$$

and α thus determines the elongation of the bubble.

1.4 Planetary sheaths

Some planetary sheaths have the same origin, however, they differ mainly in the dimension of an interaction region. Planetary sheaths range from the sheath of Mercury with a scale of $4 \cdot 10^{-4}$ AU to that of Jupiter with a scale of 0.1 AU. Observed Interplanetary Coronal Mass Ejections (ICME) sheaths increase in size

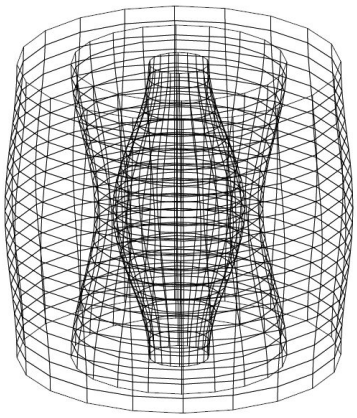

Figure 1.8: MF surfaces of the first Fourier component of the magnetic mirror perturbation. The main structure, closest to the axis, has a typical bottle shape. Moving radially away from the axis one encounters a series of nested structures which have a similar symmetry to the central one. The surfaces shown in the figure represent surfaces of constant MF, with the field increasing radially outward from the axis. The ambient field direction in this model is parallel to the axis. Adapted from *Constantinescu* (2002).

with distance from the Sun and their scale lengths increase from 0.01 AU near the Sun to tens of AU near the termination shock (TS). In the heliosheath (HSH), the region between the TS and the heliopause, the scales reach of tens to a hundred AU (*Siscoe and Odstrcil*, 2008). Nevertheless, some similarities were already found in all types of sheaths. For example, plasma depletion layers (PDLs) form in front of the obstacle (Earth, Jupiter, Saturn, ICME sheaths (*Crooker et al.*, 1979; *Farrugia et al.*, 1997; *Hammond et al.*, 1993; *Liu et al.*, 2006; *Violante et al.*, 1995)) or structures with anticorrelation between the MF and plasma density are generated downstream of quasi-perpendicular shocks (*Bavassano Cattaneo et al.*, 1998; *Burlaga et al.*, 2006a; *Hill et al.*, 1995; *Kaufmann et al.*, 1970; *Liu et al.*, 2006; *Richardson and Liu*, 2007; *Tsurutani et al.*, 1992; *Violante et al.*, 1995)).

1.5 Interaction of the SW with the heliosphere and HSH formation

1.5.1 Global structure of the heliosphere

The heliosphere extends from the solar corona to an outer boundary, the heliopause, where the SW encounters the interstellar medium. The SW flows outward at supersonic speeds until it passes through the heliospheric TS. This shock slows and heats the SW and begins the diversion of the SW plasma down the tail of the heliosphere. The region between the TS and heliopause with shocked SW plasma is called the HSH. Figure 1.9 shows a schematic picture of the heliosphere

and the locations of two Voyager spacecraft. On February 2010, Voyager 1 (V1) was at a distance of 112.7 AU from the Sun and Voyager 2 (V2) at a distance of 91.5 AU.

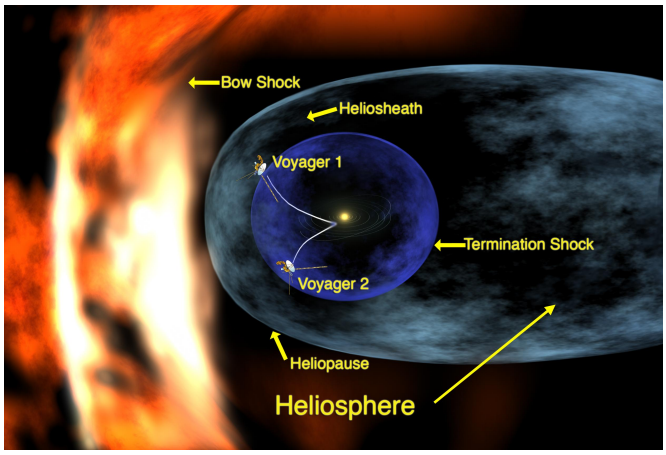

Figure 1.9: Schematic picture of the heliosphere showing the termination shock, the HSH, the heliopause, and the locations of the Voyager spacecraft. Adapted from the JPL Voyager web page.

The TS marks the abrupt slowing of the supersonic SW as it approaches contact with the interstellar wind. In the HSH region beyond the shock, the wind is slower, hotter, and denser as it interacts with the surrounding interstellar matter. V1 crossed the TS in December of 2004 at a radial distance from the Sun of 94.0 AU and at a heliographic latitude of N34.1° (*Decker et al.*, 2005; *Stone et al.*, 2005), and since then has been in the HSH. V2 crossed the TS in August of 2007 at radial distance 81.6 AU from the Sun and S27.1° and is also now in the HSH (*Burlaga et al.*, 2008; *Decker et al.*, 2008; *Gurnett and Kurth*, 2008; *Richardson et al.*, 2008; *Stone et al.*, 2008).

The time of the TS crossings on DOY 242-244, 2007 is indicated by the line in Figure 1.10. The daily averages of the MF strength (B) measured by the MF instrument on V2 from 2007 DOY 1 to 2008 DOY 75 are shown panel (a). Daily averages of the density (N), proton temperature (T), and SW speed (V) are shown in panels (b), (c), and (d), respectively, in Figure 1.10.

The region of subsonic outward flow and deflection of the postshock solar plasma has been predicted theoretically. However, its structure and properties have been discussed only for large scales. The observed fluctuations and inward and outward motions of the TS can change the observations and make it difficult to interpret.

1.5.2 Variability of the TS location

Since *Parker* (1963) proposed the description of the heliospheric interface configuration, it was already predicted that the locations of the SW TS and the he-

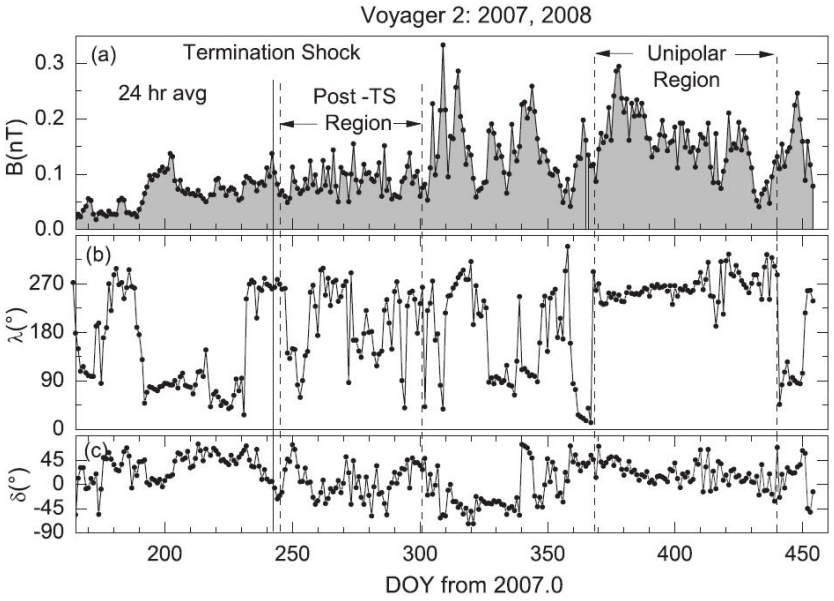

Figure 1.10: Daily averages of MF strength (a), plasma density (b), proton temperature (c), and bulk speed (d) measured by V2. Adapted from *Burlaga et al.* (2009).

liopause would vary under different inner heliospheric pressure conditions. However, these early models resulted from stationary equilibrium considerations requiring that the boundary conditions do not change in time. Model calculations with these restrictions are completed, as soon as an asymptotic state in the locations of the heliospheric structures is reached.

Barnes (1993, 1994, 1995); *Grzedzielski and Lazarus* (1993); *Naidu and Barnes* (1994); *Wang and Belcher* (1998, 1999) have considered the motion of the TS in response to a jump in the SW density or an interplanetary shock passage using a one-dimensional planar approximation. *Ratkiewicz et al.* (1996) showed that the resulting responses viewed in compression ratios and propagation speeds of the shock are much less pronounced in a spherically symmetric approach. Similar studies already based on measured perturbations of SW properties were carried out by *Whang and Burlanga* (1993) and *Whang et al.* (1999). The authors conclude that the location of the upstream TS is anti-correlated with the sunspot number, i.e., moving inward or outward at the rising or the declining phase of the solar cycle.

1.5.3 Mirror instabilities in the HSH

The HSH exhibits MF fluctuations of very large amplitudes at scales from several hours to tens of days with complex profiles. The fluctuations were described as "turbulence", although the nature and origin of these fluctuations are not fully understood.

Burlaga and Ness (2009) showed that turbulence consists of both coherent (semi deterministic) structures and random structures as seen in time profiles of the MF strength $B(t)$ on scales from 48 s to several hours, which vary greatly from day to day. They observed two different regions in the HSH (1) the "post-TS region" observed in the interval 2007 DOY 245301 (just behind the TS, which was crossed by V2 at least five times from 2007 DOY 242245) and (2) the "unipolar region" which was observed by V2 in the interval from 2008 DOY 276 in which the direction of the MF was nearly constant. The authors concluded that the fluctuations observed in these two regions differ in some important respects, but share some common properties. They have suggested that in order to understand the turbulence of the HSH, it is important to consider that the TS is rapidly evolving on a wide range of scales, including very small scales.

Liu et al. (2007) observed data from V1 after the TS crossing on 2004 December 16 (day 351). They have studied the magnetic fluctuations which where characterized by a series of depressions in the field magnitude that have been called magnetic holes (*Burlaga et al.*, 2006a,b). They showed that the magnetic holes observed by V1 in the HSH are produced by the mirror-mode instability. These fluctuations are similar to those observed downstream of quasi-perpendicular interplanetary and planetary BSs that have been identified as mirror-mode structures (*Bavassano Cattaneo et al.*, 1998; *Kaufmann et al.*, 1970; *Tsurutani et al.*, 1992; *Violante et al.*, 1995).

Chapter 2

The aims of the thesis

As we explained in the introduction part, an importance of the MSH consists in the fact that it is the interface through which energy and momentum are transported from the SW into the Earth's magnetosphere. The MSH is a highly turbulent anisotropic environment with many kinds of instabilities that propagate from the foreshock, bow shock and/or MP or are created within the MSH itself. These instabilities can launch different types of waves. As a result, the MSH MF and ion density fluctuate often with magnitudes exceeding the mean value. The sources of waves in a particular location at the MSH are not always clear because there are many factors that influenced them. It is a reason why the thesis is devoted to study the properties of MSH fluctuations.

The IMF orientation and mainly the sign of its B_Z component have been found to be a dominant factor influencing the conditions for the mentioned energy and mass transfer. However, the interaction of different discontinuities with the bow shock modifies their parameters and/or generates new discontinuities that propagate through the MSH and hit the MP. Thus, we will carry out a systematic study of the probability of observations of the same B_Z sign in the SW and in the Earth's MSH in the first part of the thesis.

In the main part of the thesis, we discuss the correlation length of MF fluctuations through the Earth's MSH. In particular: (i) we will present the results of a statistical survey of the MF fluctuations using two years of Cluster observations; (ii) we will show the dependence of the cross-correlation coefficients between different spacecraft pairs on an orientation of the separation vector with respect to the average MF, plasma flow vectors, and other parameters; (iii) we will investigate the relationship between the correlation length and upstream parameters as well as its connection with the wave mode and frequency power spectrum in the frequency interval of 0.001-0.125 Hz. A cross-correlation between the magnetic field and plasma density allows us to classify roughly a wave mode, thus (iv) we will study of the profiles of cross-correlation coefficients through the MSH at both flanks and in the subsolar region.

Finally, not only the Earth's but also other planets have the sheath of the same

origin, however, these sheaths differ in the dimension of an interaction region. The last part of the thesis deals with a comparison of the Earth's MSH with the sheath of another planet (Jupiter), with the sheath that is created between the edge of the magnetic cloud and its driven shock, and with the heliosheath.

At present, there are several spacecraft that can be used as MSH monitors. In the Earth's MSH studies, we focused on the Cluster and Themis projects located in various positions from the subsolar region to dusk and down near flanks during the years of operations; moreover, their measurements cover one half of the solar cycle. For other sheath investigations, we applied the Voyager 1 and 2 data from the Jovian sheath and heliosheath, and Wind observations of magnetic clouds. As monitors of the SW conditions, usually Wind plasma and interplanetary MF were used.

Chapter 3

Measurements of IMF and plasma parameters

3.1 Interball project

The INTERBALL Project was launched to study various SW parameters in the critical regions of the SW/magnetosphere system. This project consisted of four spacecraft, two of which were closely spaced pairs on different high-altitude orbits.

The TAIL PROBE part of the project consisted of IB-1 and its subsatellite MAGION-4 (M4) was launched on 3 August of 1995 to the elongated elliptical orbit with the inclination of 65 degrees and apogee of 200 000 km. The spacecraft separation changed from less than 100 km allowing to study the small-scale wave and plasma structures at the boundaries till $\sim 1 - 2R_E$ to study large plasma structures in the tail. Nevertheless, the main aim of the project was investigation the interaction between the SW and the MP and the outer regions of the magnetosphere.

The AURORAL PROBE with its subsatellite was launched on 29 August 1996, to the 65 degrees inclination orbit and the apogee of 20 000 km above the northern auroral zone and polar cap. This tragectory allowed to place *in situ* measurements from two probes in the global geophysical perspective of large-scale magnetospheric processes.

3.1.1 TAIL PROBE instrumentation

The ion flux measurements on-board the TAIL PROBE spacecraft were performed by the Faraday cup instruments (VDP on IB-1 (*Safrankova et al.*, 1997), VDP-S on M4 (*Nemecek et al.*, 1997)) with the time resolution of 1 or 16 Hz.

The omnidirectional plasma sensor VDP was designed to determine the integral flux vector and integral energetic spectrum of ions and electrons in the energy range of 0.2 ± 2.4 keV. For simultaneous measurements in all directions the VDP device was equipped with six independent wide-angle Faraday's cups

(FCs). Their axes form a three-dimensional orthogonal system. This configuration permits to find the main flow directions even in highly turbulent regions.

The VDP-S device was based on the simultaneous measurements of the currents of four identical FCs which are placed symmetrically on the subsatellite's surface with axes declined from the main subsatellite's axis by $\sim 45°$. Due to the satellite in-flight orientation, the axis of the first FC is directed nearly towards the Sun.

The MF vector measurements were performed by the FM-3 fluxgate magnetometer (*Nozdrachev et al.*, 1998) with a time resolution of 16 Hz on IB-1 and by the SG-R8 triaxial magnetometer on the M4 subsatellite.

The FM-3 instrument was designed to measure three components of the MF in two different ranges: $\pm$ 200 nT and $\pm$ 1000 nT. Measurements in these ranges where performed independently by two identical magnetometers M1 and M2, respectively. Each magnetometer consisted of triaxial flux-gate sensor and unit containing analogue and digital electronics. The M1 and M2 sensors where mounted on the non-magnetic boom which was attached to the edge of the solar panel.

The triaxial sensor SG-R8 was made of three monoaxial sensors orthogonally disposed; the coordinate axes of the sensor - X, Y, Z - coincide with the coordinate axes of the satellite. This magnetometer was designed for studying space and time variations of the MF intensity. In addition, it enabled one to determine the attitude of the subsatellite with respect to the MF vector.

3.2 Cluster project

The Cluster project consists of four identical spacecraft that are orbiting around the Earth. They perform a pyramid or tetrahedral (triangular pyramid) formation that allows the simultaneous measurements - from small structures (if they are separated by several hundred kilometers), to larger structures (they could be separated up to 20 000 kilometers). The spacecraft move in a very elongated polar orbit, from 19 000 to 119 000 kilometers from Earth.

Each of the four spacecraft carries an identical set of 11 instruments to investigate charged particles, electrical, and MFs. We have used spin-averaged MF (Flux Gate Magnetometer (FGM), *Balogh et al.* (2001)) and ion density (Hot Ion Analyzer (HIA), *Rème et al.* (2001)) with temporal resolutions of both ~ 4 s.

All four Cluster spacecraft carry a dual sensor FGM instrument sampling the DC ambient MF along the orbit trajectory in the frequency range of DC to 10 Hz in "Normal" mode and up to 32 Hz in "Burst" mode in the field range from -65536 nT to +65528 nT. The instrument consists of two triaxial fluxgate sensors and an electronics box.

The CIS (Cluster Ion Spectrometry) experiment is a comprehensive ionic plasma spectrometry package on-board the four Cluster spacecraft, capable of obtaining full three-dimensional ion distributions with a good time resolution

(one spacecraft spin) and with mass-per-charge composition determination. The CIS package consists of two different instruments, a Hot Ion Analyser (HIA) and a time-of-flight ion Composition Distribution Function (CODIF), including a sophisticated dual-processor based instrument control and data processing system (DPS), which permit extensive on-board data-processing.

3.3 THEMIS

The mission was launched on February 17, 2007 and the spacecraft (hereafter termed "probes") were released on a highly elliptical, 14.716 R_E geocentric apogee, 437 km altitude perigee, 15.9 deg inclination, 31.4 hr period orbit, with their line of upsides pointing at apogee towards the pre-midnight sector (Right Ascension of Perigee = 288.8 deg). The probes were checked out and placed in a stable, coast-phase orbit, traversing the dayside magnetosphere in a string-of-pearls configuration near their launch orbit (Figure 3.1). After instrument commissioning, the probes, initially named by their letters A-E, were assigned their target orbits and were designated a probe number based on their on-orbit performance (mainly antenna performance) as follows: B, C, D, E, and A were assigned constellation positions P1, P2, P3, P4, and P5, respectively.

The primary aim of THEMIS was to elucidate which magnetotail process is responsible for substorm onset at the region where substorm auroras map ($\sim 10R_E$): (1) a local disruption of the plasma sheet current (current disruption) or (2) the interaction of the current sheet with the rapid influx of plasma emanating from reconnection at $\sim 25R_E$. The probes also traversed the radiation belts and the dayside magnetosphere allowing to address additional baseline objectives, namely: how the radiation belts are energized on time scales of 2-4 hours during the recovery phase of storms, and how the pristine SW interaction with upstream particle beams, waves, and the BS affects the Sun-Earth coupling.

The five spin-stabilized (T spin = 3 s) THEMIS probes where equipped with comprehensive *in situ* particles and fields instruments that measure the thermal and super-thermal ions and electrons, and electro magnetic fields from DC to beyond the electron cyclotron frequency in the regions of interest.

The THEMIS Fluxgate Magnetometer (FGM) (*Auster et al.*, 2008) detects the background magnetic field and its low frequency fluctuations (up to 64 Hz) in the near-Earth space. The FGM is capable of detecting variations of the MF with amplitudes of 0.01 nT, and it is particularly designed to study abrupt reconfigurations of the Earth's magnetosphere during the substorm onset phase. The FGM uses an updated technology developed in Germany that digitizes the sensor signals directly and replaces the analog hardware by software. A use of the digital fluxgate technology results in lower mass of the instrument and improved robustness.

The Electro Static Analyzer (ESA) built at UCB to the recent heritage of the

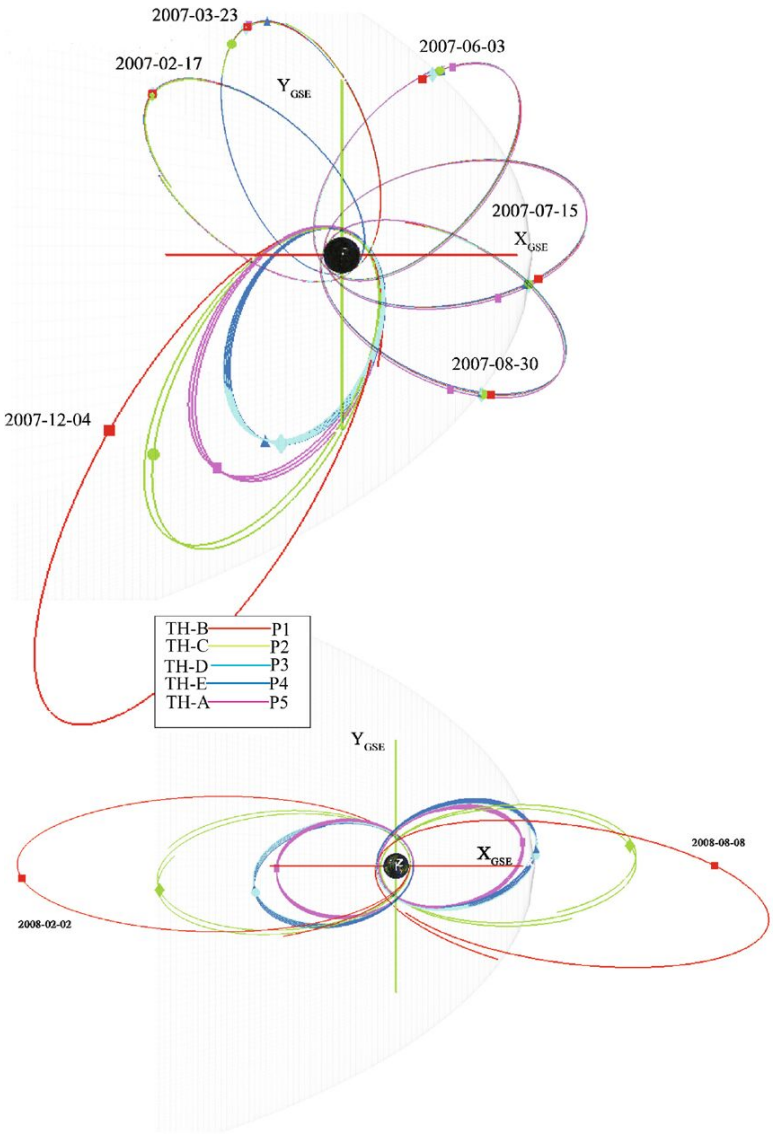

Figure 3.1: Top: THEMIS coast phase actual orbits; Bottom: THEMIS 1st year baseline orbit predicts (axis size is 10 R_E). Adapted from *Angelopoulos* (2008).

FAST ESA and the Cluster HIA instruments registers ions and electrons between 5 eV and 25 keV. On-board moment computations on an FPGA permit a subtraction of photoelectron fluxes and routine data collection and transmission of moments at spin period resolution. The ESA ground and in-flight inter-calibration, intracalibration and absolute calibration are described in *McFadden et al.* (2008) and result typically in better than 10% accuracy moments.

3.4 Wind

Wind is a spin stabilized spacecraft launched in November 1, 1994 and placed in a halo orbit around the L1 Lagrange point which is a point of the Earth-Sun gravitational equilibrium, more than 200 R_E upstream of Earth to observe the unperturbed SW that is to impact the magnetosphere of the Earth (Figure 3.2).

The primary science objectives of the Wind mission were: (1) provide complete plasma, energetic particle, and MF for magnetospheric and ionospheric studies; (2) investigate basic plasma processes occurring in the near-Earth SW; (3) provide baseline, 1 AU, ecliptic plane observations for inner and outer heliospheric missions.

In this thesis we used the Wind spacecraft as an upstream SW monitor of the MF and plasma data mainly for Cluster statistics 2002-2003 when it was orbiting in the SW (Figure 3.2).

The Wind MF Investigation (MFI) is composed of two triaxial fluxgate magnetometers located at the mid point and end of a 12 m boom. The instrument provides: (1) near real-time data at nominally one vector per 92 s as key parameter data for broad dissemination; (2) rapid data at 10.9 vectors s^{-1} for standard analysis; and (3) occasionally, snapshot memory data and Fast Fourier Transform data, both based on 44 vectors s^{-1}. The instrument features a very wide dynamic range of measurement capability, from ± 4 nT up to ± 65536 nT per axis in eight discrete ranges (*Lepping et al.*, 1995).

The SW Experiment (SWE) on the WIND spacecraft is a comprehensive, integrated set of sensors. It consists of two Faraday cup sensors; a vector electron and ion spectrometer (VEIS); a strahl sensor, and an on-board calibration system. The energy/charge range of the Faraday cups is 150 V to 8 kV, and that of the VEIS is 7 to 24.8 kV. The time resolution depends on the operation mode used, but can be of the order of few seconds for 3D measurements (*Ogilvie et al.*, 1995).

3.5 ACE

The Advanced Composition Explorer (ACE) was launched on August 25, 1997. The ACE orbits around the L1 libration point about 1.5 million km from the Earth and 148.5 million km from the Sun. The elliptical orbit affords ACE

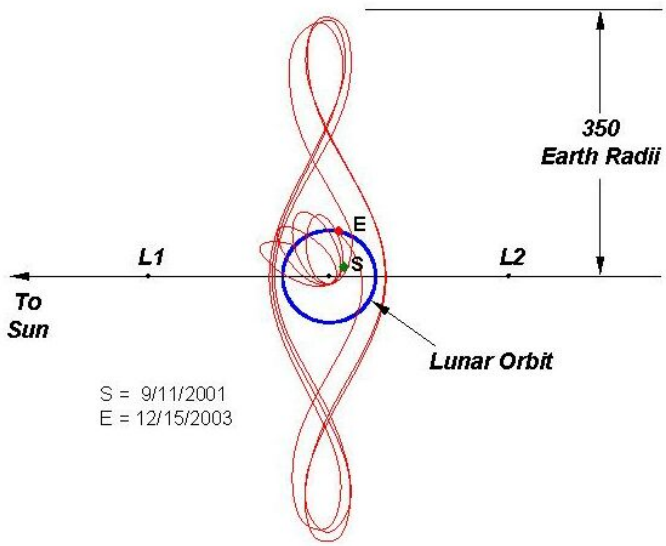

Figure 3.2: Wind distant prograde orbit - September 1, 2001 to December 15, 2003. Adapted from NASA's WIND web page.

a prime view of the Sun and the galactic regions beyond (Figure 3.3). The spacecraft carried nine instruments that provided high-precision measurements of the elemental, isotopic, and ionic charge-state composition of energetic nuclei over a broad energy range.

SWEPAM is a SW Electron, Proton, and Alpha Monitor that is designed to measure the three-dimensional characteristics of SW and suprathermal electrons from $\sim$ 1 to 900 eV and ions from 0.26 to 35 keV (*McComas et al.*, 1998). It consists of modified versions of the spare SW electron and ion sensors from the Ulysses mission.

MAG (*Smith et al.*, 1998) is a twin triaxial flux-gate sensors which are located 165 inches (= 4.19 m) from the center of the spacecraft on opposing solar panels. The electronics and digital processing unit (DPU) is mounted on the top deck of the spacecraft. The two triaxial sensors provide a balanced, fully redundant vector instrument and permit some enhanced assessment of the spacecraft's MF. The instrument provides high-level data with between 3 and 6 vector s^{-1} resolution for continuous coverage of the interplanetary magnetic field. Two high-resolution snapshot buffers each hold 297 s of 24 vector s^{-1} data while onboard Fast Fourier Transforms extend the continuous data to 12 Hz resolution. Magnetometer measures the dynamic behavior of the vector MF, including measurements of interplanetary shocks, waves, and other features that govern the acceleration and transport of energetic particles.

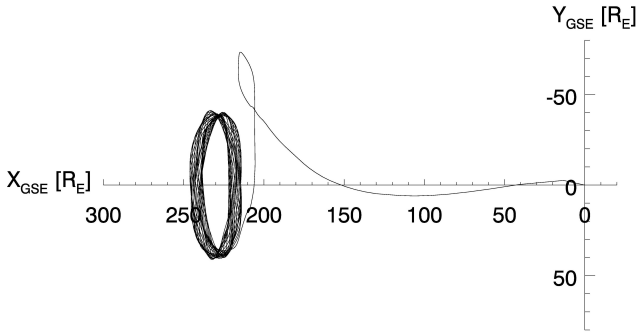

Figure 3.3: Projection of ACE orbits into the XY plane in the GSE coordinate system - August 26, 1997 to August 23, 2010.

3.6 Voyager interstellar mission

The twin Voyager 1 and 2 spacecraft have been launched in August (V2) and September (V1), 1977 on trajectories toward the giant planets, which was also toward the upstream direction of the heliosphere. After the successful planetary encounters, the Voyager Interstellar Mission continues outward with the goal of making first observations of the local interstellar medium. Both Voyagers already crossed the TS.

The identical Voyager spacecraft are three-axis stabilized systems that use celestial or gyro referenced attitude control to maintain pointing of the high-gain antennas toward Earth. The prime mission science payload consists of 10 instruments (11 investigations including radio science). Only five investigator teams are still supported, though data are collected for two additional instruments.

The Voyager plasma experiment (PLS) registers SW protons simultaneously in three Earthward-pointing Faraday cups over an energy range of 105950 eV with a time resolution of 192 s (*Bridge et al.*, 1977). When possible, the three spectra are fit with convected isotropic Maxwellian distributions to determine the proton velocity, density, and temperature. However, data quality often does not allow this fitting procedure.

The MF (MAG) experiment to be carried on Voyager 1 and 2 missions consists of dual low field (LFM) and high field magnetometer (HFM) systems (*Behannon et al.*, 1977). The dual systems provide greater reliability and, in the case of the LFM, permit the separation of spacecraft MFs from the ambient fields. Addition reliability is achieved through electronic redundancy. The wide dynamic ranges of $\pm 5 \cdot 10^4$ nT for the LFM and $\pm 200 \cdot 10^4$ nT for the HFM, low quantization uncertainly of ± 0.002 nT in the most sensitive (± 8 nT) LFM range, low sensor RMS noise level of 0.006 nT, and the use of data compaction schemes to optimize the experiment information rate all combine to permit the study of broad spectrum of phenomena during the mission.

3.7 Analysis of MF and plasma density fluctuations

In this part, we describe the techniques which are applied in our particular studies. We used the Fourier transformation to obtain a power spectral density for the energy spectra of MF fluctuations. For a rough classification of wave modes, we calculated cross-correlation coefficients between the magnetic field strength and density, and studied the form (slope) of the frequency power spectrum of magnetic fluctuations. From theory it is known that values for slopes around -5/3 suggests that the nonlinear turbulence cascades are a dominant process in forming the spectra of fluctuations.

3.7.1 The Fourier transformation

A physical process can be described either in the time domain by the values of some quantity h as a time function $h(t)$, or in the frequency domain, where the process is described by its amplitude H as a function of frequency $f, H(f)$ with $-\infty < f < \infty$. The Fourier transform equations for representations of a process will be

$$\begin{array}{c} H(f) = \int_{-\infty}^{\infty} h(t) e^{2\pi i f t} dt \\ h(f) = \int_{-\infty}^{\infty} H(f) e^{-2\pi i f t} df. \end{array} \tag{3.1}$$

From Equation (3.1) it is clear that the Fourier transformation is a linear operation.

The Fourier transform of a discrete function can be obtained after approximation of the integral in Equation (3.1) by a discrete sum:

$$H(f_n) = \int_{\infty}^{-\infty} h(t) e^{2\pi i f_n t} dt \approx \sum_{k=0}^{N-1} h_k e^{2\pi i f_n t} \Delta = \Delta \sum_{k=0}^{N-1} h_k e^{2\pi i k n / N}. \tag{3.2}$$

The final summation in Equation (3.2) is called the *discrete Fourier transform* of the N points h_k, denoted by H_n,

$$H_n \equiv \sum_{k=0}^{N-1} h_k e^{2\pi i k n / N}. \tag{3.3}$$

The formula for the discrete *inverse* Fourier transform, which recovers the set of points h_k from H_n is:

$$h_k = \frac{1}{N} \sum_{k=0}^{N-1} H_n e^{-2\pi i k n / N}. \tag{3.4}$$

The *total power* in a signal is the same in the time domain or in the frequency domain:

$$\text{Total Power} \equiv \int_{\infty}^{-\infty} |h(t)|^2 dt = \int_{\infty}^{-\infty} |H(f)|^2 df. \tag{3.5}$$

The *one-sided power spectral density (PSD)* define "how much power" is contained in the frequency interval between f and $f + df$ of the function h:

$$PSD_h(f) \equiv |H(f)|^2 + |H(-f)|^2, \quad 0 \leq f < \infty. \tag{3.6}$$

For real function *h(t)* $PSD_h(f) = 2|H(f)|^2$.

3.7.2 Correlation coefficient

There are two traditional ways of characterizing the correlation structure of a stationary signal: one is to use the autocorrelation function in the time domain and the other is to use the spectral density function in the frequency domain; both functions have distinct features that compensate for each other - the autocorrelation function describes linear relations among consecutive random samples in the time domain, whereas the spectral density function depicts the power distribution over different frequencies.

The correlation of two functions *h(t)* and *g(t)* with their corresponding Fourier transforms $H(f)$ and $G(f)$, denoted $Corr_{g,h}(\tau)$ is defined by

$$Corr_{g,h}(\tau) \equiv \lim_{T \to 0} \int_{-T}^{T} g(t + \tau)h(t)dt. \tag{3.7}$$

The correlation is a function of τ, which is called the *lag*. Multiplying the Fourier transform of one function by the complex conjugate of the Fourier transform of the other gives the Fourier transform of their correlation:

$$Corr_{g,h} \Leftrightarrow G(f)H(-f). \tag{3.8}$$

The correlation of a function with itself is called its *autocorrelation*. In this case, Equation (3.8) becomes the transform pair

$$Corr_{g,g} \Leftrightarrow |G(f)|^2. \tag{3.9}$$

For the characteristic of two signals it is widely used a *linear correlation coefficient*. For pairs of quantities (g_i, h_i), $i = 0, 1, ...N + M$, the linear correlation coefficient CC (also called the product-moment correlation coefficient or *Pearson's CC*) is given by the formula:

$$CC(l) = \frac{\sum_{i=0}^{N}(g_{i+l} - \overline{g})(h_i - \overline{h})}{\sqrt{\sum_{i=0}^{N}(g_{i+l} - \overline{g})^2}\sqrt{\sum_{i=0}^{N}(h_i - \overline{h})^2}}, l = (0, 1, ...M). \tag{3.10}$$

The value of CC lies between -1 and 1, inclusive. It takes on a value of 1, termed "complete positive correlation", when the data points lie on a perfect

straight line with a positive slope, with g and h increasing together. The value 1 holds independent of the magnitude of the slope. If the data points lie on a perfect straight line with a negative slope, h decreasing as g increases, then CC has the value -1; this is called "complete negative correlation". A value of CC near zero indicates that the variables g and h are uncorrelated.

3.7.3 Correlation length

Correlation length (CL) is the distance from a point beyond which there is no further correlation of a physical quantity associated with that point. Values for a given quantity at distances beyond the correlation length can be considered purely random.

In this study, we have calculated CL for the analyzed quantity and plotted it as a function of other quantity. We have made an exponential fit for the dependence of the CC calculated from MF strengths measured by Cluster spacecraft pairs vs their spatial separation:

$$CC(SS) = exp\left\{-(SS/CL)\right\}, \tag{3.11}$$

where SS stands for the spacecraft separation, CL for the correlation length, and CC was computed according to Equation (3.10).

3.8 Data sets and processing

In the statistical study of prediction of the MSH B_Z component from IMF observations, we have used well-proven sets from previous analyses: IB-1 (*Hayosh et al.*, 2005), IMP 8 (*Paularena et al.*, 2001), and Cluster (*Gutynska et al.*, 2009). The set of THEMIS MSH observations was created for this purpose.

The analysis is based on four sets of MSH magnetic field measurements from different spacecraft: IB-1 (*Klimov et al.*, 1997); IMP 8; Cluster (*Balogh et al.*, 2001) represented by C1; and THEMIS (*Auster et al.*, 2008) represented by THC. These spacecraft operated in the MSH in various phases of solar activity connected with Solar Cycle 23. Detailed information about the data sets (including the years of operation, coordinates in the GSE system, and a number of observational points) is listed in Table 3.1.

The study is based on a comparison of 5 min averaged MSH MF measurements with corresponding IMF observations. We used Wind as a common monitor of IMF B_Z for all four data sets. Wind data was lagged by the propagation time using a two-step approximation including the separation of both spacecraft along the X_{GSE} axis and the actual SW velocity measured by Wind. We excluded those time intervals when Wind was located near the BS (or foreshock), in the MSH, or inside the magnetosphere.

S/c	Years	X_{GSE}, R_E	Y_{GSE}, R_E	Z_{GSE}, R_E	No.
IB-1	1995-1999	$-20 < .. < 0$	$-25 < .. < 25$	$-15 < .. < 15$	~ 24000
IMP 8	1997-2001	$-35 < .. < -1$	$-35 < .. < 35$	$-30 < .. < 20$	~ 9300
C1	2002, 2003	$-7 < .. < 9$	$-20 < .. < 20$	$-10 < .. < 10$	~ 8000
THC	2007, 2008	$-10 < .. < 5$	$-10 < .. < 15$	$-2 < .. < 8$	~ 2700

Table 3.1: Data sets for each spacecraft, years of data collection, a range of coordinates of measurements, and the number of MSH measurements represented by 5 minutes averages. THEMIS MSH data are taken through June, July, and August 2007 from all THEMIS spacecraft and through May and November 2008 from THC, only.

For comparison with other upstream SW monitors, we applied the solar wind monitor ACE (*McComas et al.*, 1998) and the OMNI database (*King and Papitashvili*, 2005) for the set of the Cluster data. Also, in these cases, we used the same methodology to propagate 5 min averaged ACE or multispacecraft OMNI IMF data (*http://omniweb.gsfc.nasa.gov/*).

THEMIS C scanning near dayside MSH regions was applied as a measuring MSH point and was compared with THEMIS B, which was simultaneously located in the SW.

An analysis of the correlation length of MSH MF fluctuations is based on the MF strength measured by four Cluster spacecraft near the dawn-dusk meridional plane ($-7 < X_{GSE} < 7R_E$) on both flanks in a broad range of latitudes ($-10 < Z_{GSE} < 10R_E$). The reason for this selection was that Cluster spent usually several hours continuously in the sheath region and provided a sufficient amount of data for statistical processing.

The radial projection of the orbits used for an analysis is shown in Figure 3.4 together with the average model BS (*Jeřáb et al.*, 2005) and MP (*Shue et al.*, 1997) positions. Since the Cluster apogee is low, a majority of data was collected in the MP vicinity. A part of the orbits seems to lie outside of the MSH in Figure 3.4, however, this impression is caused by uncertainties in the applied models and variability of upstream parameters. We have carefully chosen only the intervals when all Cluster spacecraft were located in the MSH. The selection of such intervals proceeded in several steps. In the first step, we selected four basic intervals (May-June and November-December, 2002 and 2003) when the Cluster spacecraft were orbiting in our chosen region. The second step consisted of a visual inspection of daily plots of plasma and MF parameters and a rough identification of the MSH intervals. These intervals were divided into subintervals of a 60-min length and each of them underwent a new inspection to discard the subintervals containing BS or MP crossings or data gaps.

Altogether, we selected $\sim$ 740 one-hour intervals for further computation. For each of the selected intervals, we have calculated (1) the maximum cross-correlation coefficient between pairs of the spacecraft on the interval of 1200-s

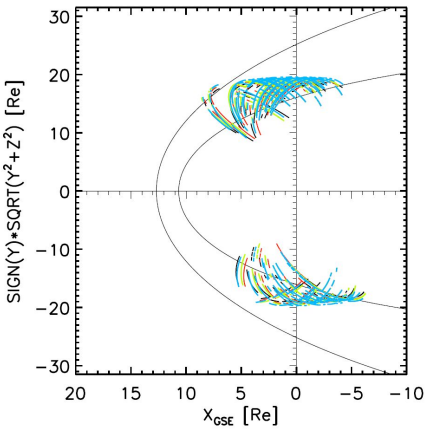

Figure 3.4: Radial projections of four Cluster spacecraft orbits. The data used are from the intervals of May-June, 2002, 2003 and November-December, 2002, 2003. The full lines display average locations of both MP and BS determined from the *Shue et al.* (1997) and *Jeřáb et al.* (2005) models, respectively (*Gutynska et al.*, 2008).

duration in the middle of each 1-h subinterval (6 values per interval), (2) the value of the cross-correlation functions computed between MF strength and ion density fluctuations for the C1, C3, and C4 spacecraft for zero time lag, (3) averaged upstream parameters (ACE MF and plasma data lagged on the propagation time are used), and (4) the location of a particular spacecraft with respect to the MP model (*Shue et al.*, 1997). The power of the fluctuations is described by a standard deviation and their character by a slope of the frequency spectrum on the interval of $0.001 - 0.125$ Hz.

For the study of MHD waves in the HSH, we have used the MF and SW proton data observed by the V2 probes.

The proton density has been calculated from the equation:

$$N = \sum_{k=1}^{8} \frac{I^k \sqrt{2M_p}}{Ae^{3/2} \left(U_t^k + U_p^k\right)^{1/2}}, \tag{3.12}$$

where I^k is a measured current from a channel k on collector B, M_p is the mass of the proton, A is the area of the entrance aperture, e is the charge of an electron, U_t^k is the threshold voltage of the channel k, and U_p^k is the peak threshold voltage of the channel k. Plasma data have a 192 s time resolution (*Bridge et al.*, 1977) and we used the highest available resolution (48 s) of MF data (*Behannon et al.*, 1977). Since these two parameters have different time resolutions, we linearly interpolated the proton density to obtain the same time resolution as MF measurements. The resulting data set consists of subintervals of 8-12 hour duration that repeat each day in two regions: (1) 2007 DOY 245 to 301, the post-TS region (38 intervals); and (2) 2008 DOY 2 to 75, the unipolar region (55

intervals).

The correlation functions have been computed for fluctuations with periods from $\sim$ 48 seconds (temporal resolution) to $\sim$ 2 hours (duration of the continuous intervals of data). For each of these intervals, we computed a cross-correlation coefficient using 10-12 hours of MF measurements in the center of the time interval and a time lag with respect to proton density measurements in a range of $\pm$3 hours or longer.

To compare fluctuations on different scales and various locations, we have extended our Cluster statistics (2002-2003) with further Cluster and Themis observations in the Earth's MSH.Enhanced data sets are shown in Figure 3.5 a) and b). A new Cluster data set covered the subsolar and near subsolar regions, $-12R_E < Z_{GSE} < 5R_E$ (Jan-Apr 2007, 2008) and the Themis data set also at the subsolar and near flank regions, $-4R_E < Z_{GSE} < -1R_E$ (Jan-Apr 2007, 2008). The selection of the intervals proceeded by the same way as for first Cluster statistics (2002-2003). In summary, a new Cluster set of events consists of 537 one-hour intervals (i.e., 1074 cross-correlation coefficients from the C1 and C3 spacecraft), and the Themis set consists of 373 one-hour intervals (863 cross-correlation coefficients from the P1-P5 spacecraft).

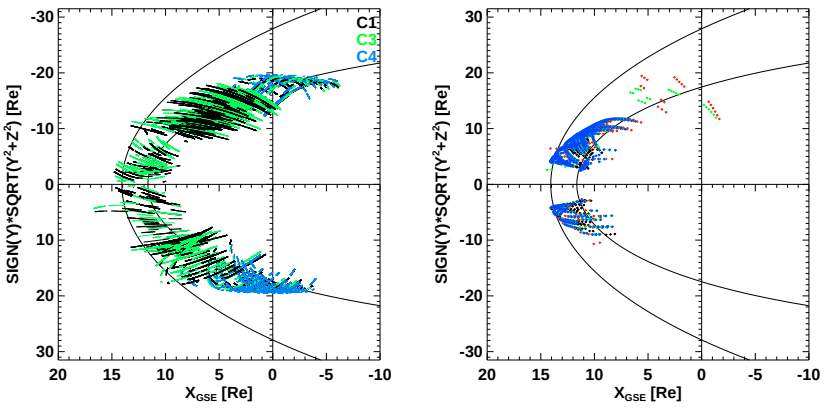

(a) (b)

Figure 3.5: a) Radial projections of Cluster orbits (C1, C3 and C4) from May-June 2002, 2003, November-December 2002, 2003 and Cluster orbits (C1 and C3) from January-April 2007, 2008. **b)** Radial projections of Themis (five spacecraft) orbits from June-August 2007, 2008. The full lines display average locations of both the MP and BS determined along the *Shue et al.* (1997) and *Jeřáb et al.* (2005) models, respectively.

To analyze fluctuations in the magnetic cloud sheaths observed at the 1 AU by Wind (*Lepping et al.*, 2006), we used a list of registered magnetic cloud driven shocks and defined magnetic cloud boundaries from *Lynnyk et al.* (2011). The

cross-correlations between B and N have been computed on half-hour intervals and data time resolution was 3 s (256 cross-correlation coefficients).

For the study of such fluctuations through the Jupiter's sheath (JSH), we used Voyager 1 and 2 both inbound and outbound crossings. Figure 3.6 shows these crossings of the Jupiter sheath by Voyager 1 and 2. We used 1-hour intervals

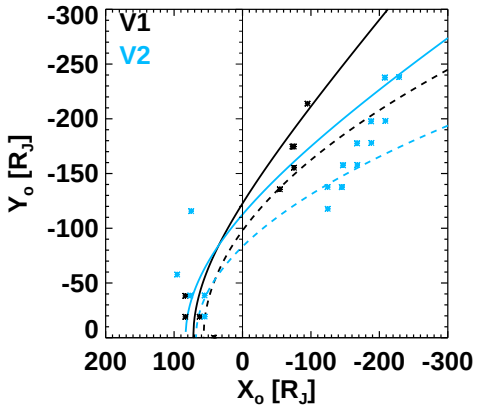

Figure 3.6: The inbound and outbound crossings of the JSH by V1 (black) and V2 (blue) in Jupiter's coordinates (average shock and MP locations are determined according to *Lepping et al.* (1981)).

with a 48-s time resolution of data and performed a similar correlation analysis of MF and density fluctuations in the frequency range of $1.38^{-4} - 1.10^{-2}$ Hz (32 cross-correlation from inbound and 120 cross-correlations from outbound orbits).

The cross-correlation function and the correlation length where computed as it is described in Section 3.7.2 and 3.7.3, respectively. Table 3.2 summarizes all used data sets in this study including their time resolutions and used spacecraft instruments.

		Plasma		**Magnetic field**	
S/c	**Region**	**Experiment**	**Res., s**	**Experiment**	**Res., s**
IB-1	MSH	VDP	1	FM-3	1/16
M4	MSH	VDPS	1	SG-R8	1/16
CLUSTER	MSH	CIS	4	FGM	4
THEMIS	SW, MSH	ESA	3	FGM	3
WIND	SW	SWE	3	MFI	3
ACE	SW	SWEPAM	64	MAG	16
V1	SW	PLS	192	MAG	48
V2	SW	PLS	192	MAG	48

Table 3.2: A survey of plasma and magnetic field instruments and data resolutions for measurements in the SW or in the MSH.

For data processing and visualization, we have applied programming language *Interactive Data language* (*http://www.ittvis.com/idl/*).

Chapter 4

Prediction of the MSH MF B_Z component from IMF observations

This chapter presents the results of a statistical study of reliability of the prediction of the MSH B_Z component from IMF observations. The study was published in *Šafránková et al.* (2009) and is attached in [**A1**].

A vector of the IMF can be represented in the GSE coordinate system by three components, two of which (B_X and B_Y) are oriented parallel to the ecliptic plane. The third component, B_Z is perpendicular to the ecliptic plane. This component is usually small and fluctuating near the ecliptic plane because it is mainly created by waves and other disturbances in the SW. When IMF and geomagnetic field lines are oriented antiparallel to each other, they can reconnect and result in the transfer of energy, mass, and momentum from the SW to magnetosphere. The strongest coupling occurs when the IMF B_Z component is oriented southward. From this point of view, the IMF B_Z is an important quantity; its sign and value influence many particular physical processes: (1) relations between the IMF orientation and draping in the dayside MSH and their impact on the ionosphere (e.g., *Coleman*, 2005); (2) observations of different plasma transients near the MP: a variety of vortices on different scales (e.g., Kelvin-Helmholtz vortices (e.g., *Hasegawa et al.*, 2006; *Nykyri et al.*, 2006; *Volwerk et al.*, 2008), kinetic Alfvén vortices (*Alexandrova et al.*, 2006; *Sundkvist et al.*, 2005), nonlinear vortex waves (e.g., *Savin et al.*, 2002, 2004) in the cusp-MSH interface, and a vortex-like cavity created because of the MP indentation (*Tkachenko et al.*, 2008)) and magnetic islands (*Eriksson et al.*, 2009); (3) creation of flux transfer events and their association with a southward IMF component (e.g., *Kawano and Russell*, 1997a; *Korotova et al.*, 2008); (4) geometry of the high-latitude MP (e.g., *Bogdanova et al.*, 2005; *Zhang et al.*, 2007); (5) locations, dynamics, and properties of the low- and high-altitude cusp (e.g., *Escoubet et al.*, 2008; *Merka et al.*, 2002; *Newell et al.*, 1989; *Němeček et al.*, 2000a, 2003); and (6) variations of the flank

low-latitude boundary layer (LLBL) thickness (e.g., *Šafránková et al.*, 2007) as examples.

On the other hand, despite the fact that it is a MSH magnetic field that comes into contact with the MP, only a few authors have commented on the impact of the MSH magnetic field orientation on reconnection and other processes. For example, *Nishida* (1989), *Kawano and Russell* (1997b), and *Sibeck* (2009) noted reconnection between antiparallel MSH and magnetospheric magnetic fields. The main reason for this is probably associated with the fact that the SW is monitored permanently, while systematic MSH observations are rather sporadic.

In order to find out if a sign of the IMF B_Z component is changing or not through the bow shock, we made a statistical study where we tested the sign of the magnetic field B_Z component in the MSH and its relation to the sign of the IMF B_Z component as determined by different upstream monitors. We used a standard propagation method of upstream observations from Wind and ACE as well as the OMNI database.

As we noted, the study is based on a comparison of 5 min averaged MSH magnetic field measurements with corresponding IMF observations.

An example of our analysis for the Cluster 1 data set is displayed in Figure 4.1. The figure shows the number of observations and probability of the same sign

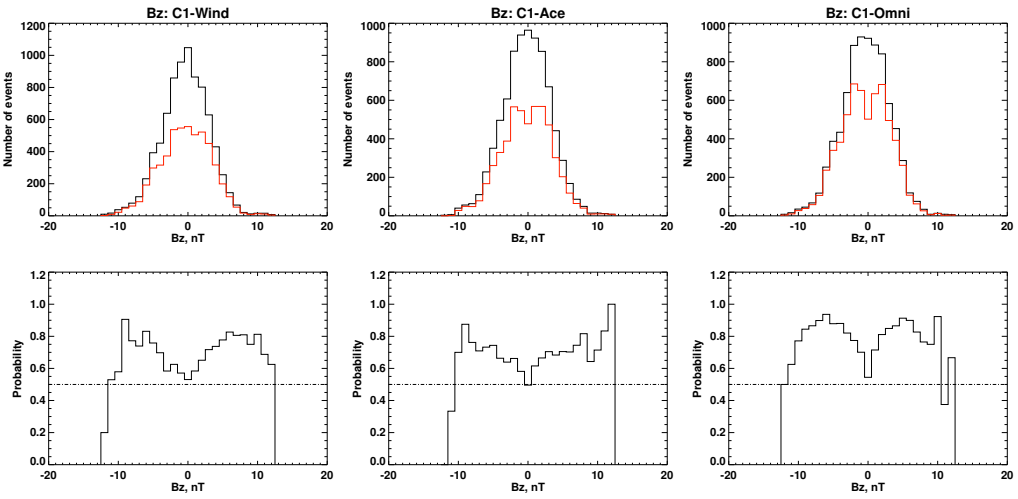

(a) (b) (c)

Figure 4.1: (top) A number of IMF B_Z observations in the SW registered by different SW monitors as a function of IMF B_Z (black line) and the number of the observations exhibiting the same B_Z sign in the MSH as determined by C1 (red line). (bottom) The probability that the same sign of the B_Z component is observed in the SW and MSH. The horizontal dash-dotted line displays the probability corresponding to a random coincidence of both B_Z signs. SW monitors used: (a) Wind, (b) ACE, and (c) OMNI.

obtained from C1 during an interval of maximum solar activity. The probability of the coincidence of B_Z signs in the SW and MSH is low for small B_Z and rises very slowly with increasing $|B_Z|$ reaching a level of 0.9 for $|B_Z| > 5$ nT (Figure 4.1(a) and (b)). However, the events with such large values of B_Z are not too frequent; they represent only 10% of all events in this data set (see Figures 4.1(a) and (b), top).

The method of propagation of the IMF measurements toward the MSH used in our analysis is rather simple. Thus, we have compared MSH observations from Figures 4.1(a) and 4.1(b) and the best up-to-date monitor of upstream conditions that represents the OMNI database. A comparison of the particular plots in Figure 4.1 shows that the OMNI database provides better results. The maximum of prediction probability rises from 0.8 to 0.9.

The analysis has shown that the IMF B_Z sign is not fully altered in the MSH. Results are summarized in Figure 4.2 for different sets and two values of IMF B_Z: -2 and -5 nT. One can note a clear solar cycle modulation for both values of IMF B_Z. However, Figure 4.2 brings a bad message for all studies of MP processes that use SW monitors as a proxy of the B_Z sign. Taking into account that IMF $|B_Z| < 2$ nT is about 60% of the time (e.g., *Němeček et al.*, 2003), the probability that MSH B_Z coincides with the prediction is generally very low.

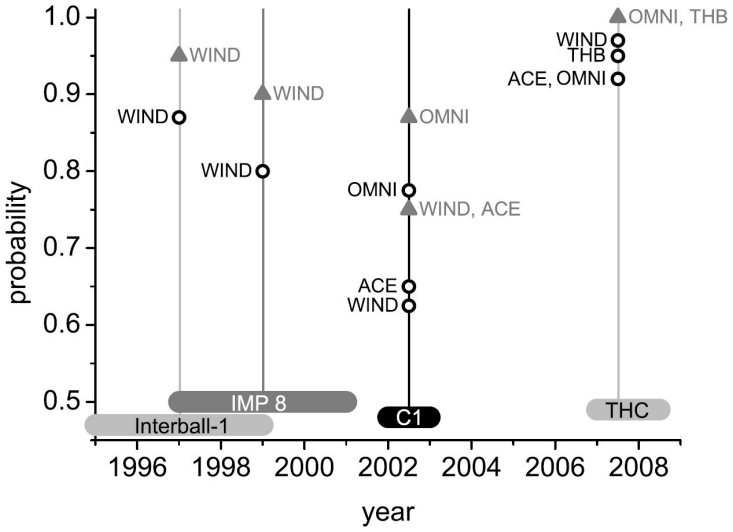

Figure 4.2: Dependence of the prediction probability on the solar cycle. The horizontal bars represent different data sets; the open circles stand for IMF $B_Z = -2$ nT, and the solid triangles show the probabilities for IMF $B_Z = -5$ nT (*Šafránková et al.*, 2009)[**A1**].

Finally, we can conclude that the probability of observation of the same sign of the B_Z component in the SW and at the particular point in the MSH (1) depends on the phase of solar cycle being largest at the solar minimum and gradually

decreases with increasing solar activity and (2) rises with the B_Z magnitude from values close to 0.5 for $|B_Z| \sim 1$ nT and reaches unity for $|B_Z| \sim 10$ nT during solar minimum, whereas a value of 0.95 was obtained for solar maximum. However, the present study did not cover the subsolar region ($X_{GSE} > 9R_E$).

Chapter 5

Plasma and/or MF fluctuations in different sheaths

In this chapter, we discuss MF and plasma density fluctuations which appear in the sheath and can vary with amplitudes and with time scales. We start from a brief examination of a case study of ion flux fluctuations in the Earth's MSH observed by two shortly separated spacecraft (by $\sim 1R_E$). The results of this study served as a motivation to a further study of the Earth's MSH: the correlation length of MF fluctuations and their properties.

5.1 Two-point observations of ion flux fluctuations in the Earth's MSH

This study is based on an analysis of measurements obtained onboard IB-1 and M4 satellites at the dusk flank of the MSH on January 28, 1997 and it was published by *Gutynska et al.* (2007) and is attached in [**A2**].

Figure 5.1 in this study (see [**A2**]) shows an overview of the event. One can note that, although the overall features of both spacecraft measurements are similar, the ion flux fluctuations exhibit significant differences (compare ninth and tenth panels in Figure 5.1, [**A2**]). In order to quantify them, we are presenting frequency spectra of fluctuations computed on the 12-minute subinterval in Figure 5.2. The spectra this figure, panels (a) and (c) were computed for the quasi-perpendicular upstream BS and thus they exhibit a low level of fluctuations with very similar spectra in both measuring intervals. On the other hand, the fluctuations in Figure 5.2 (b) measured behind the quasi-parallel BS are enhanced by an order of magnitude at all frequencies. This behavior could be expected but we can see that the amplitudes of low-frequency components are significantly larger at the IB-1 location (compare the power density of 10^2 on the M4 and 10^3 on IB-1 in the frequency range of $0 - 0.03$ Hz). This fact is surprising because the wavelength of such fluctuations is comparable or larger

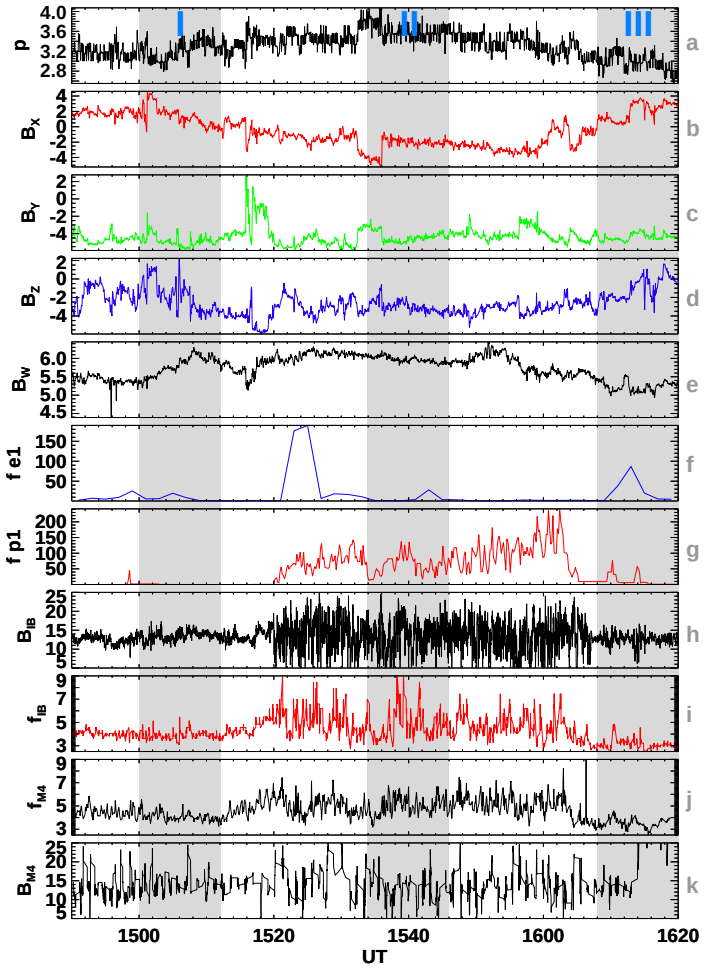

Figure 5.1: The ion flux and MF MSH fluctuations observed by IB-1 and M4 and corresponding SW conditions measured by WIND. From top to bottom: p - WIND dynamic pressure; B_x, B_y, B_z - WIND MF components; B_W - WIND MF magnitude; f e1 - IB-1 high-energy electron flux (*Kudela et al.*, 1995); f p1 - IB-1 high-energy ion flux (*Kudela et al.*, 1995); B_{IB} - IB-1 MF magnitude; f_{IB} - IB-1 ion flux; f_{M4} - M4 ion flux; B_{M4} - M4 MF magnitude (*Gutynska et al.*, 2007)[**A2**].

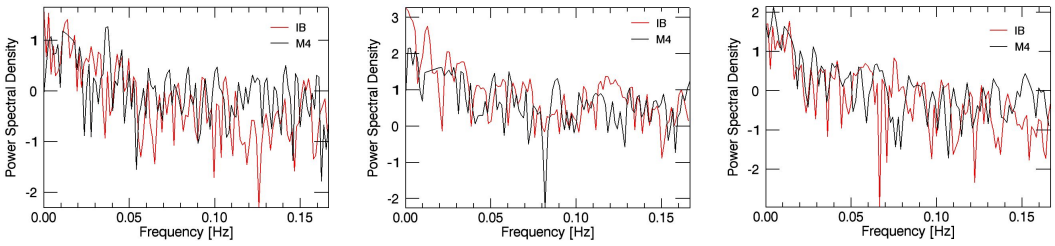

(a) (b) (c)

Figure 5.2: FFT spectra of ion flux fluctuations measured by IB-1 (red line) and M4 (black line) versus the frequency computed on the intervals (a) 1500-1512 UT, (b) 1536-1546 UT, and (c) 1608-1620 UT on January 28, 1997.

than the spacecraft separation. It means that these fluctuations can be hardly treated as a wave propagating through the MSH and that a description in terms of a non-linear interaction of multiple waves would be more appropriate for IB-1 and M4 observations.

As a conclusion, we could summarize that the analyzed fluctuations are probably generated at the quasi-parallel BS and the level of fluctuations can differ by an order of magnitude in two points separated by $\sim 1 R_E$.

5.2 Correlation length of MF fluctuations in the Earth's MSH

Based on conclusions in the previous section, we present the results of a statistical survey of the MSH MF fluctuations using two years of Cluster observations (*Gutynska et al.*, 2008) [**A3**]. We discuss the dependence of the cross-correlation coefficients between different spacecraft pairs on the orientation of the separation vector with respect to the average MF and plasma flow vectors and other parameters.

This study is based on the MF strength measured by four Cluster spacecraft in the MSH near the dawn-dusk meridional plane. Figure 5.3 shows the correlation coefficients as a function of the spacecraft separation. Since the correlation function depends on the time lag, the maxima of the cross-correlation function are plotted in this and following figure. The different spacecraft pairs are distinguished by the colors and only separations less than $0.05 R_E$ are shown. Since no systematic difference between the s/c pairs can be observed, we do not distinguish the s/c pair used for computation of a particular correlation coefficient in our analysis. However, the figure reveals one striking feature of MSH variations – the correlation coefficient can be as low as 0.5 for points separated by 100 km. The length of plasma waves in our frequency range is much larger (> 1000 km). The linear approximation of the trend shown by the heavy line leads to a value

of about $1R_E$ for a correlation coefficient equal to zero.

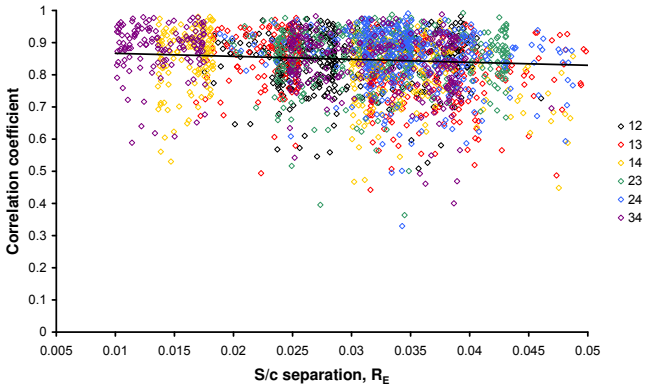

Figure 5.3: Cross-correlation coefficients as a function of the s/c separation. Only the separations shorter than $0.05R_E$ are displayed, the different colors denote a spacecraft pair (see a legend on the right side of the figure) (*Gutynska et al.*, 2008)[**A3**].

A similar result can be derived from Figure 5.4, where average values of correlation coefficients (regardless of the spacecraft pair) are plotted for the whole data set. The bins for averaging increase with the s/c separation in order to obtain a reasonable number of events in each bin. The averaged correlation coefficient rapidly falls down with the s/c separation until $\sim 0.2R_E$ and it exhibits a saturation at a level of ~ 0.3 for the largest s/c separations. The trend can be described rather well by a power law in a form $y = A \cdot x^B$ (see the heavy line in the figure), so we used this fit in our analysis.

The influence of the foreshock can be estimated by dividing the data set into dawn and dusk subsets (not shown here). The difference between distribution of points as well as the fits were not statistically significant and the presence of the foreshock fluctuations does not influence the correlation length in the MSH.

The MSH fluctuations are often treated as an ensemble of plasma waves, thus the direction of the magnetic field with respect to the s/c separation vectors would influence the value of the correlation coefficient. However, such investigation should reflect the dependence of the correlation coefficient on the separation distance shown in previous figures. Following the profile of this dependence, we have divided our set into three subsets according to separation length: separations shorter than $0.4R_E$, separations between 0.4 and $1R_E$ and larger separations (i.e., $> 1R_E$). The $1R_E$ break point was chosen because we determined the correlation length of this order and we think that the behavior of correlation coefficients can be different for larger separations. Figure 5.5(a) presents the correlation coeffi-

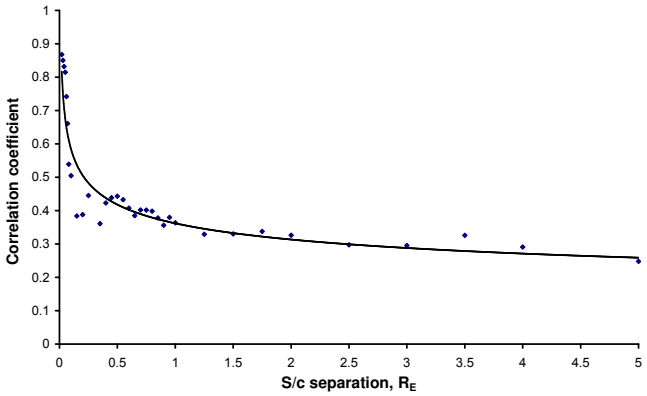

Figure 5.4: Averages of cross-correlation coefficients as a function of the s/c separation for a full set of events. The heavy line stands for a power-law fit (*Gutynska et al.*, 2008)[**A3**].

cient as a function of the angle between the separation vector and averaged MF ($S \times B$ angle) for the above groups of events. The data belonging to each of these groups are fitted with a linear fit. The group of shortest separations exhibits only a weak dependence of the correlation coefficient on the $S \times B$ angle. This effect can be expected because a typical correlation in this group is ~ 0.85. Nevertheless, the correlations are larger for small angles. This trend can be clearly seen in the second group (separations between 0.4 and $1R_E$) but the trend is very weak and reversed in the group of largest separations. However, a usual value of the correlation coefficients in this group is only ~ 0.3. We conclude that the correlations are slightly larger for the direction parallel to the MF, i.e., waves propagating along the ambient MF are correlated over longer distances than those proceeding in the perpendicular direction. In Figure 5.5(b) the correlation coefficients are plotted vs the angle between the s/c separation and velocity vectors ($S \times F$ angle). Figure 5.5(b) shows larger correlations for small $S \times F$ angles for all groups of s/c separations. Similarly to the previous figure, this trend is very clear for the separations between 0.4 and $1R_E$ and weak for other two groups.

According to *Zastenker et al.* (1999, 2002), the MSH variations can be divided into two classes: variations penetrating through the BS from the SW and intrinsic MSH variations. We checked whether these two classes behave the same way using the correlation of WIND and C1 MFs as a measure of penetration of solar wind variations into the MSH. Figure 5.6 shows the correlation coefficients between the Cluster pairs as a function of the C1-WIND correlation coefficients. The data are again sorted according to the s/c separations. The conclusion from this figure is clear; the correlation between two MSH points increases with the

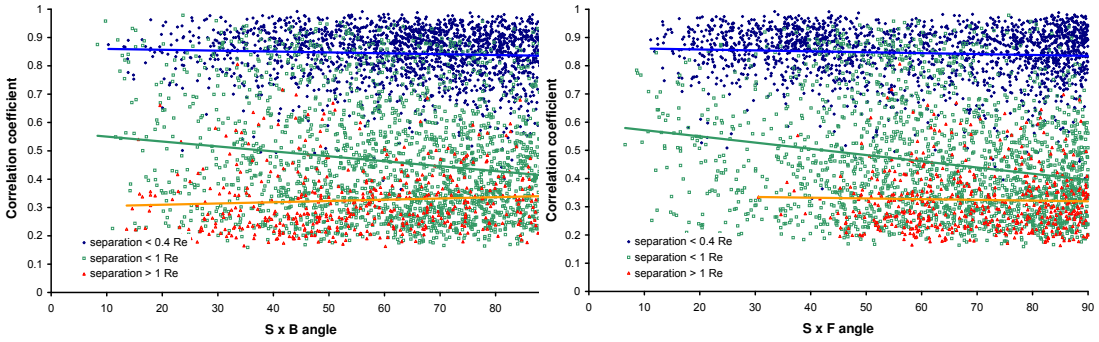

(a) (b)

Figure 5.5: Cross-correlation coefficients as a function of the angle between the s/c separation and averaged MF vectors, $S \times B$ (a) and the angle between the s/c separation and ambient plasma velocity vectors, $S \times F$ (b). The events are grouped according to the s/c separation and linear fits are shown for each group (*Gutynska et al.*, 2008)[**A3**].

correlations of IMF and MSH MF regardless of the s/c separations. A larger MSH-SW correlation can probably be interpreted as an increasing portion of SW variations in the MSH and the trends in Figure 5.6 suggest that these variations correlate over longer distances in the MSH than intrinsic MSH fluctuations.

Our analysis of two years of the Cluster MF measurements in the vicinity of the dawn-dusk meridional plane has shown that the correlation length of the fluctuations in the range of 0.001–0.125 Hz is approximately $1R_E$ in a statistical sense. This value is consistent with that obtained by *Lucek et al.* (2001) in their case study of mirror mode waves. However, we found a number of cases when the correlation falls to 0.5–0.6 for separations shorter than $0.05R_E$. If the fluctuations are small, their correlation may be poor because the contribution of the natural and uncorrelated noise prevails.

Based on results obtained by *Gutynska et al.* (2008)[**A3**], we continued these MSH studies and performed statistical investigations of properties of observed fluctuations in the frequency range of 0.001-0.125 Hz (*Gutynska et al.*, 2009)[**A4**].

Figure 5.7 presents the same set of events as we used in our previous statistical study. Since analyzed observations are not distributed equally within the range of spacecraft separations, we divided them into two groups of preferential separations: less than $0.1R_E$ and between 0.4 and $0.8R_E$. Within these ranges of separations, we have selected the groups of points with extremely low (red and green points in Figure 5.7) and high (black and yellow points) correlation coefficients. The groups are marked with different colors in Figure 5.7 (in which

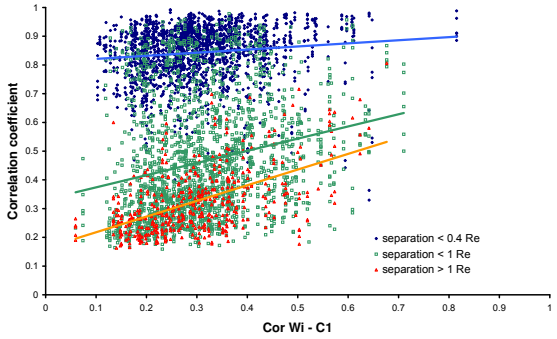

Figure 5.6: Cross-correlation coefficients between two MSH points as a function of the cross-correlation function between IMF (Wind) and MSH MF (*Gutynska et al.*, 2008)[**A3**].

an overview of all cross-correlation coefficients is plotted as a function of s/c separations). The black line shows the exponential fit of the whole data set. The fit provides a value of correlation length of about $0.75R_E$.

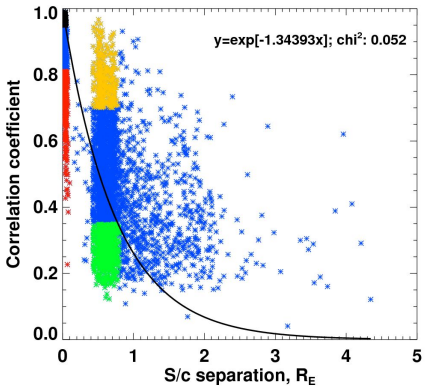

Figure 5.7: Cross-correlation coefficients of the magnetic field strength measured in two MSH points as a function of their separation. The black line shows the exponential fit, and its parameters (including $\chi^2 = 0.052$) are given in the top right corner (*Gutynska et al.*, 2009)[**A4**].

One can note a lack of points with correlations lower than ~ 0.2. We suggest that this is caused by a limited number of points used for correlation. In order to estimate the influence of a limited number of points, we generated several random sequences that simulated the Cluster data and applied the same procedures for calculation of correlations. When we used 300 points (a number of points used for correlations), the correlation coefficients ranged from 0.16 to 0.22, whereas using five times as many points leads to coefficients that do not exceed 0.1. Based on

this analysis, we note that the correlation coefficients on a level of 0.25 means that the signals are essentially uncorrelated. This suggests that the trend of the plots of correlation coefficients vs the s/c separation to saturation at a level of ~ 0.25 is a product of the data processing but it does not change our conclusion that a typical correlation length of the MSH fluctuations is about $1R_E$.

We have checked the distribution of extreme correlation coefficients within the MSH. The colored points from the selected groups were sufficiently dense in all locations. Thus, we have separately compared two groups of events with larger than average correlation coefficients (black and yellow points in Figure 5.7) and we did not find any difference. The same was true for a mutual comparison of other two groups (red and green in Figure 5.7). It means that the analyzed properties are conserved on the distances of the order of $1R_E$. For this reason, we have merged two groups of MSH observations with larger correlations (black and yellow) and plotted the probability that an event belongs to the merged group (i.e., the correlation is large) in Figure 5.8. Figure 5.8(a) shows that the proba-

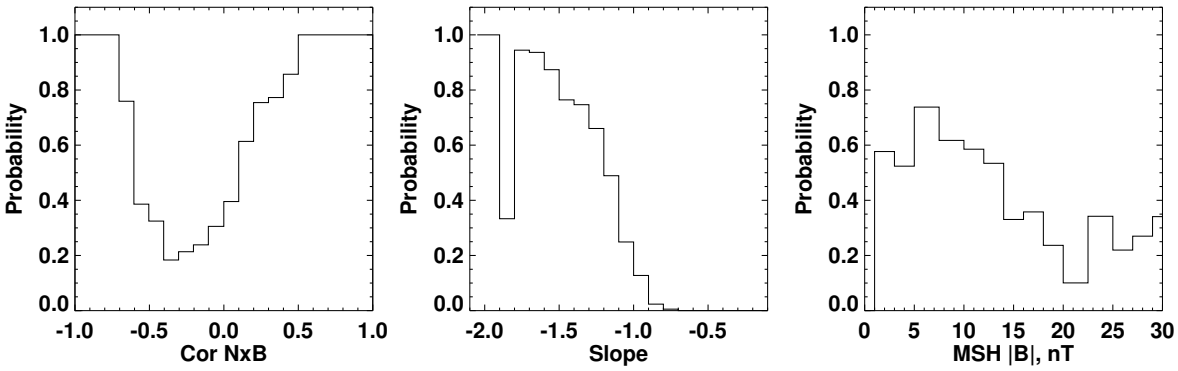

(a) (b) (c)

Figure 5.8: The probability of observations of larger than average cross-correlation coefficients as a function of: (a) the cross-correlation between the MF strength and ion density, (b) the spectral slope, and (c) the MSH MF strength. Adapted from *Gutynska et al.* (2009)[**A4**].

bility reaches unity when the cross-correlation between MF and plasma density is close either +1 or -1, i.e., when the MSH fluctuations are dominated by a particular wave mode. A more important criterion is probably of the spectral slope. Figure 5.8(b) shows the probability of larger correlations of the MF measured by two spacecraft as a function of the slope. This probability is nearly zero for slopes from 0 to -1 and rapidly increases for steeper slopes reaching unity for slopes of about -2.

The histograms in Figure 5.8(a), and (b) have shown that the wave modes present at a particular MSH location influence significantly their correlation over moderate distances (up to $0.8R_E$). The conditions for a local excitation of a

particular wave mode or for its propagation from a distant source would depend on the background values of MSH parameters. We have tested the probability that a particular observation belongs to the group of highly correlated events as a function of different parameters including the plasma density, MF strength and direction, ion β, etc. but we have found only the magnetic field strength to exhibit a notable influence on this probability (Figure 5.8(c)). Large values of the correlation coefficients were preferentially (60%) observed for an averaged local MF below $\sim$ 15 nT, whereas this probability falls dawn to $\sim$ 30% above this value. A similar, but no so distinct change was observed for ion β (larger correlations belong to the high-β regime). We assume that the reason for a better organization of the cross-correlation coefficients by the MF strength alone is connected with difficulties of a determination of a proper temperature in the anisotropic non-Maxwellian MSH plasma.

Further, we analyzed dependence of the correlation length on several upstream parameters. We evaluated the influence of the SW speed and density, and IMF B_Z component, etc. Criteria for binning into particular subsets were (1) approximately equal number of points in each subset, and (2) a sufficiently dense coverage of spacecraft separations in the interval of $0 - 2R_E$. We have computed the correlation length (equation 3.7.3) within each subset. Obtained correlation lengths are then plotted as a function of the analyzed parameter and fitted with linear fits in Figure 5.9, which does not show error bars, but since the points are averages from $\sim$ 1.000 individual values, the errors are $\sim$ 0.05 and never exceed 0.07.

Conditions for excitation of different wave modes, their growth rates, and their amplitudes would depend on the upstream parameters. However, our results show that the connection between these parameters and the correlation length of MSH fluctuations is surprisingly weak. Figure 5.9(a) suggests that the correlation length is a slightly rising function of the SW speed. On the other hand, it is not influenced by the upstream density, as it is shown in Figure 5.9(b). The correlation length is connected with the processes at the MP because we have found a longer correlation length for large negative values of the IMF B_Z component as it is displayed in Figure 5.9(c).

The penetrating variations are correlated over longer distances and they increase the correlation length as it can be seen from Figure 5.10(a) where the correlation lengths are plotted as a function of cross-correlations between the Wind and Cluster C1.

Based on our previous results (*Gutynska et al.*, 2008)[**A3**], we suggest that one of the most important factors influencing the correlation length of MSH MF fluctuations is their amplitude described by the standard deviation (SD).The results are plotted in Figure 5.10(b) and one can see a clear rising trend of the correlation length from $\sim 0.6R_E$ for SD $\sim$ 2 nT up to $\sim 1.2R_E$ at SD $\sim$ 6 nT. Since the average MSH MF strength in our data set is between 8 and 20 nT, we can suppose that even if the magnitude of the MF fluctuations is comparable

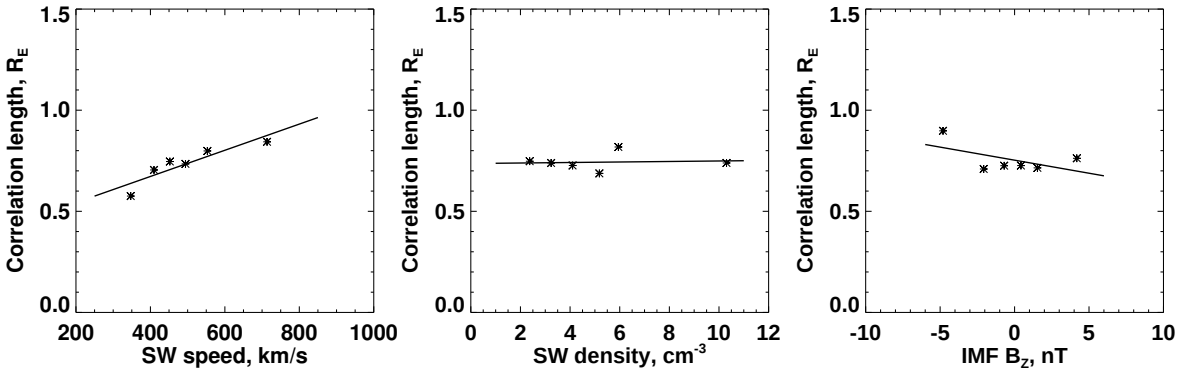

Figure 5.9: Correlation length of MSH fluctuations: (a) as a function of the upstream speed; (b) versus SW density; (c) as a function of the IMF B_Z component (*Gutynska et al.*, 2009)[**A4**].

with the mean value their correlation length only slightly exceeds $1R_E$.

The downstream parameters in a given MSH location are generally considered to be proportional to their upstream values (e.g., *Spreiter et al.*, 1966). This is probably the reason why plots of the correlation length as functions of the downstream density, MF strength, speed, and ion beta resemble all features of corresponding plots for upstream parameters, thus we are not showing them. However, the proportionality constant is a function of the location in the MSH. We are investigating a narrow MSH slice, so the most important parameter would be a relative location with respect to MSH boundaries that we describe by the radial distance of Cluster 1 from the model (*Shue et al.*, 1997)MP. The plot of the correlation length versus this distance is shown in Figure 5.10(c). Both the MP and BS were suggested to be sources of the MSH fluctuations, thus one would expect a better correlation over longer distances near the source. Figure 5.10(c) confirms this expectation for the MP but the dependence is only weak. The MSH thickness at the dawn-dusk meridian is about $10R_E$ and the last point in Figure 5.10(c) belongs to the middle of the MSH. An analysis of measurements closer to the BS suggests a new rise of the correlation length in this region but we have only a limited number of observations there.

Finally, we can conclude that the correlation length of MSH MF fluctuations is generally short ($\sim 0.7R_E$), however, it is longer under specific upstream conditions: (1) during intervals of the high SW speeds (Figure 5.9(a)); and (2) it slightly increases with higher values of the IMF strength. Similarly, the correlation length is longer (3) if the cross-correlation between the IMF and MSH MF is higher (Figure 5.10(a)); and (4) if the amplitude of fluctuations represented by a standard deviation (Figure 5.10(b)) is larger. Nevertheless, these effects are not necessarily independent because, for example, fluctuations with larger amplitudes

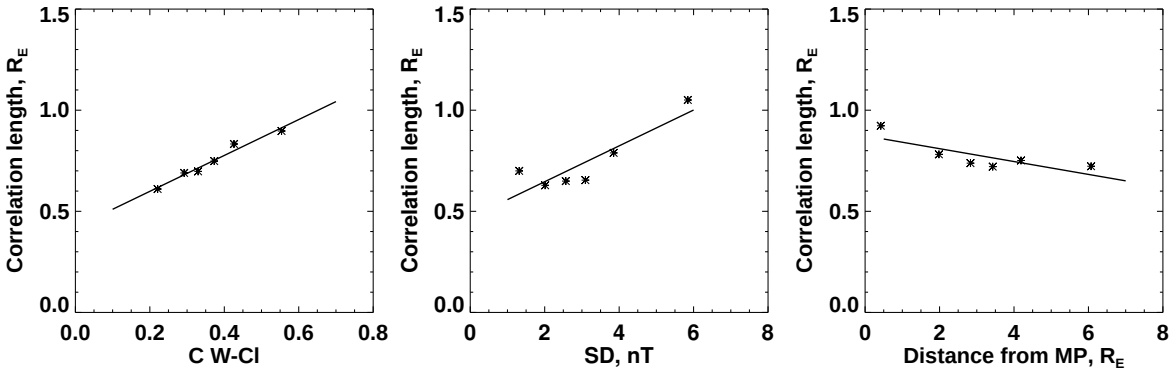

(a) (b) (c)

Figure 5.10: Correlation length of MSH fluctuations: (a) as a function of the cross-correlation coefficient between the IMF and MSH MFs; (b) as a function of their standard deviation; (c) versus the distance to the MP (*Gutynska et al.*, 2009)[**A4**].

can be excited by high-speed solar wind streams. We have tested this hypothesis by plots of one of aforementioned parameters as a function of another and we did not find any notable functional dependence.

On the other hand, Figure 5.10(c) shows a slight dependence of the correlation length on the distance of a measuring point from the MP being larger near the MP. From this follows that the MP plays some role in the wave mode propagation and/or excitation (e.g., *Alexandrova et al.*, 2008; *Attié et al.*, 2008). This role is probably connected with subsolar reconnection because Figure 5.9(c) shows a longer correlation length of fluctuations for a strongly negative IMF B_Z component.

Figure 5.8(b) suggests that the cross-correlations are generally larger when their spectral slope is steeper, i.e., when the spectrum is dominated by low frequencies. Our search for conditions favorable for excitation and propagation of such waves have brought almost negative results because we have found only two parameters exhibiting an influence on the spectral slope. First of them is the distance to the MP as it can be seen from Figure 5.11(a) where the spectral slope is plotted as a function of this distance. A preference of steeper slopes at the MP vicinity can probably explain a larger correlation length in this region (Figure 5.10(c)). On the other hand, steeper slopes are observed during intervals of a low SW speed as it can be seen from Figure 5.11(b). This dependence is rather complicated but an overall trend is clear and out of error bars. In accord with Figure 5.8(b), the steeper spectral slopes would result in longer correlation length of MSH fluctuations but Figure 5.9(a) shows an opposite trend. Both dependencies are out of the statistical errors, thus a more complex multifactor study is required for an explanation of this contradiction.

As a conclusion, we can note that the correlation length of MSH MF fluctuations varies from 0.5 to $1.5R_E$. It means that for a reliable determination of the MF at the MP, the monitor should be as close as $\sim 1R_E$ from the investigated MP point.

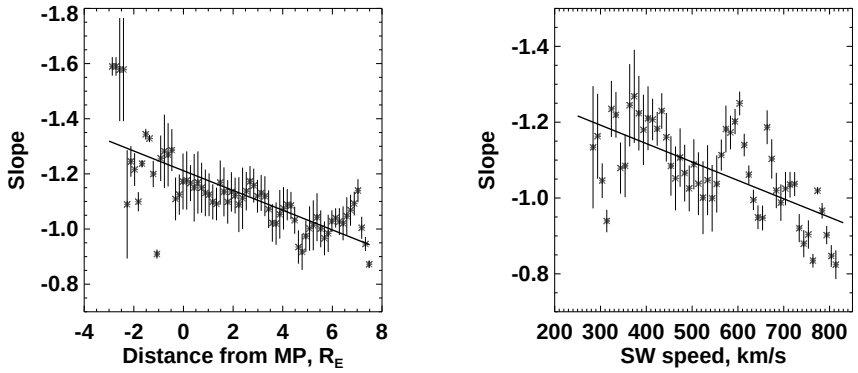

(a) (b)

Figure 5.11: The dependence of the frequency spectrum slope on: (a) the distance of a measuring point to the MP; (b) the SW speed (*Gutynska et al.*, 2009)[**A4**].

5.3 MHD waves in the HSH

The HSH exhibits MF fluctuations of very large amplitudes at scales from several hours to tens of days with complex profiles. We performed a study of correlation properties of fluctuations of the plasma density, N, and magnetic field strength, B, measured by V2 in two HSH regions.

The purpose of the study was to find the dominant wave modes in the HSH, to deduce possible sources of these waves, and to compare the HSH with the Earth's MSH. Among many types of fluctuations observed in these regions, we concentrated on MHD waves that exhibit a significant correlation between the plasma density and magnetic field strength (*Gutynska et al.*, 2010)[**A5**].

Figure 5.12 shows an example of the MF and plasma density profiles measured in one $\approx$ 10 hr time interval on DOY 277 of 2007 in the post-TS region. A duration of the interval where we correlate the data is 120 minutes. The bottom panel shows the autocorrelation coefficients of the MF (blue line), as well as the proton density (red line) and their cross-correlation coefficients (black line). The auto-correlation does not decrease to zero for large time lags, which suggests the presence of coherent periodic components. The same is true for the profile of the density auto-correlation but the periodicity is different. The cross-correlation techniques allow us to filter from the whole spectrum of fluctuations those in which B and N behave a coherent way. The dashed line distinguishes the maximum and minimum of the cross-correlation coefficient, which are +0.7

and −0.7, respectively. In this particular case, the difference of the corresponding lags (≈ 230 minutes) is approximately equal to a half of the period of the dominant MHD wave. However, the cross-correlation profile suggests the presence of a wave with a much shorter period, about 55 minutes. The presence of two (or more) waves can explain why the typical value of the cross-correlation coefficient for zero lag was found to be arbitrary (close to zero in Figure 5.12), whereas the MHD theory predicts that B and N would change in phase or anti-phase for fast and slow waves, respectively.

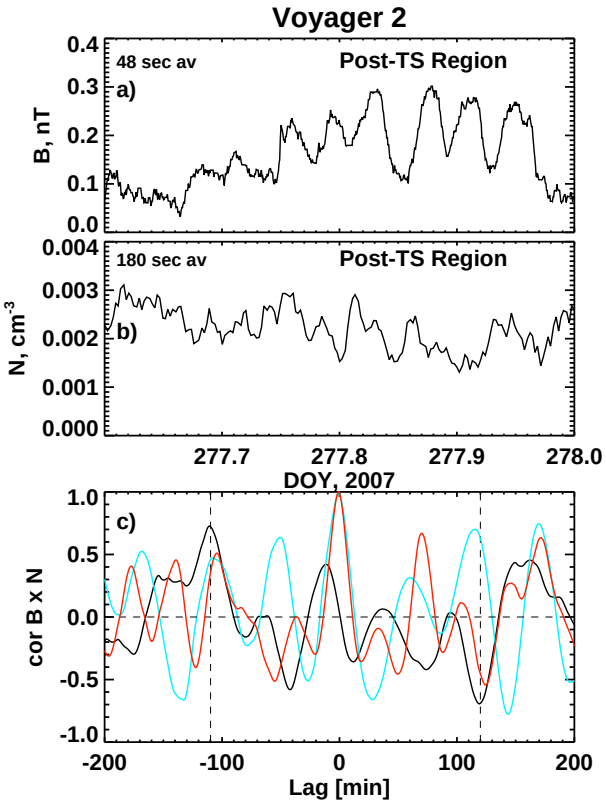

Figure 5.12: An example of measured and computed profiles through one ≈ 10 hr time interval on DOY 277 of 2007: (a) the MF, (b) the plasma density, and (c) the computed cross-correlation coefficient between the MF and plasma density (black line) and the auto-correlation coefficients of the magnetic field (blue) and the proton density (red). The light dashed lines distinguish one half of the period of the dominant MHD wave (*Gutynska et al.*, 2010)[**A5**].

Figure 5.13 shows the comparison of the real signals and 1000 pairs of generated random sequences processed the same way. The black squares show the average maximum (top) or minimum (bottom) correlations computed using different data subintervals within the post-TS region (38 intervals). The black bars show the standard deviations. The green squares show the correlations for the unipolar region (55 intervals) and the red for the random signals. The MF and

plasma density exhibit a statistically significant correlation. The mean correlation coefficient decreases nearly linearly with the duration of the subinterval and approaches the random sequence level for subintervals of 4 $\approx$ 600 minute long. This result indicates that the coherent features persist for about 10 hr in the analyzed frequency range.

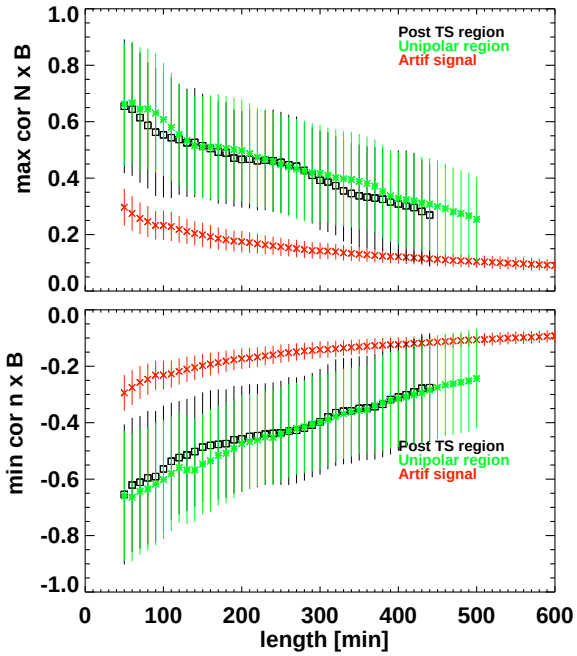

Figure 5.13: Averaged profiles of maxima and minima of correlation coefficients in both regions computed using subintervals with different durations. For comparison, the correlation coefficients derived from a random sequence of two signals are also shown (red points) (*Gutynska et al.*, 2010)[**A5**].

The same features were found in both regions, but the correlation is slightly higher in the unipolar region. Since the MHD fluctuations are generated either at the TS or locally in the HSH near the TS, the small increase of the correlation at larger distances from the TS suggests that the incoherent fluctuations are gradually damped as they are convected from the source through the post-TS region to the unipolar region.

Finally, Figure 5.14 presents histograms of the maxima (positive values) and minima (negative values) of correlation coefficients between N and B in both regions. The distributions are nearly identical, which suggests that the periodic behavior shown in the last panel of Figure 5.12 is typical. The most frequent values of the coefficients are around 0.6 and are slightly higher in the unipolar region. These values are surprisingly large; *Gutynska et al.* (2009) reported that correlation coefficients of 0.4 were typical in the Earth's MSH. The distribution of correlations for zero lag (red line in Figure 5.14) is very broad and centered around zero. This suggests that there is no preferred wave mode in the HSH,

whereas *Gutynska et al.* (2009) found slow or mirror mode to be more frequent in the MSH.

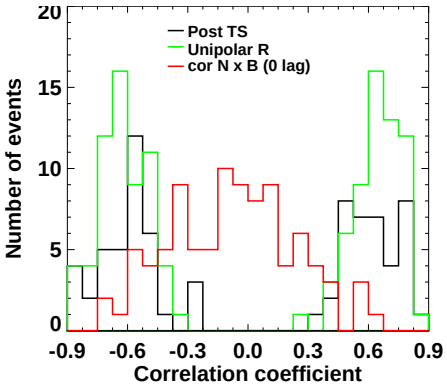

Figure 5.14: Distributions of maximum and minimum correlation coefficients in the post-TS (black) and unipolar (green) regions. The red histogram shows the distribution of correlations coefficients for zero lag in both regions (*Gutynska et al.*, 2010)[**A5**].

We can note that one-point measurements are insufficient for a reliable determination of the wave mode. If the mirror mode waves in the HSH (*Liu et al.*, 2007) and in the Earth's MSH behind of the quasi-perpendicular BS (e.g., *Schwartz et al.*, 1996; *Tátrallyay et al.*, 2008) were similar, the typical wavelength would be of the order of 10^6 km. Since the mean Alfvén velocity is about 50 km s^{-1} and mean flow speed $\approx$ 150 km s^{-1} in the HSH, the wavelength of other modes would be of the same order. Such waves cannot propagate (or be convected) through planetary MSHs (*Hubert et al.*, 1998), thus a comparison of these apparently similar environments is difficult. Nevertheless, we extended this study including the JSH and MC sheaths.

5.4 Comparison of sheaths

In this chapter, we compare properties of plasma and MF fluctuations in the sheaths on different scales. As we noted in Chapter 1.4, the scales of the interactions vary greatly. *Richardson and Liu* (2007) proposed a review of sheaths regions including planetary MSHs, ICME sheaths and the HSH and found several similarities as well as differences. The authors reported observations of mirror mode waves with periods increasing with distances in steady state sheaths and longer periods in ICME sheaths. We used data sets (see Chapter 3.8) of sheath observations and performed the similar study of correlations between plasma density and MF fluctuations.

Since we used all available data from the HSH and JSH observations, data sets from studied regions are discussed together regardless of the exact area of

sheaths which they cover. Figure 5.15(a) presents the results of such analysis. A comparison of maxima and minima of correlation coefficients between the HSH and JSH shows larger coefficients (> 0.7) in both HSH regions behind the TS. The coefficients are slightly lower (~ 0.5) in the JSH.

On the other hand, the Earth's MSH correlations are significantly lower (< 0.4). The different situation is in the MC sheath, there are minima of correlation coefficients very high (> 0.9). Figure 5.15(b) shows a distribution of correlation coefficients for zero time lags for the MC sheaths and the Earth's MSH. In the MC sheaths, correlation coefficients are large and almost negative (> 0.9). Also in the MSH, we found negative correlations both in the subsolar and flanks regions (0.3–0.4). We would note that the maxima of distributions of correlation coefficients for zero time lags in the HSH and JSH were about zero.

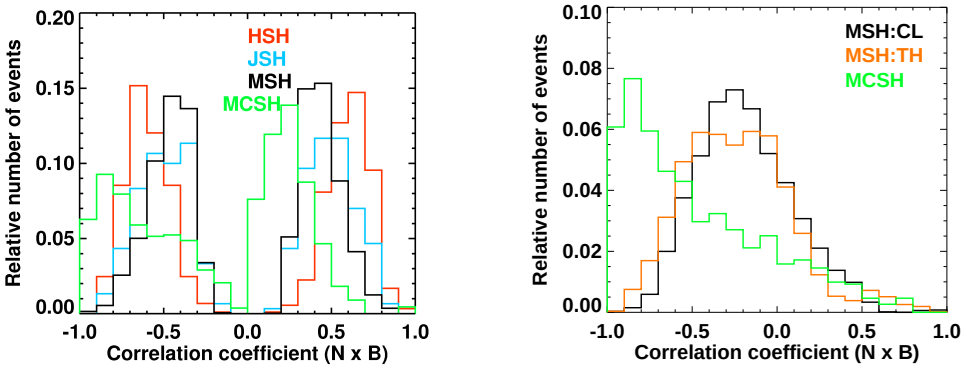

(a) (b)

Figure 5.15: (a) A comparison of distributions of maxima and minima of correlation coefficients in the HSH, JSH, MC sheaths, and Earth's MSH. (b) Histogram of correlation coefficients between B and N for a zero lag in the MSH (MSH:TH - the subsolar region, MSH:CL - flanks regions) and in MC sheaths.

The distribution of correlation coefficients through the MC sheath profile is shown in Figure 5.16(a). The set was divided into two groups: non-expanding (or with a slight change of the expansion velocity – blue points) and expanding (those clouds with large expansion velocities (red points) according to *Lynnyk and Vandas* (2010)). We normalized the distance between the shock and leading edge of MCs, thus we can discuss what types of waves are generated in a particular place of the MC sheath. Significant positive correlations that correspond to the fast wave mode were found only near the shock. On the other hand, mean correlation coefficients about -0.6 were found in the rest of the sheaths. It means that the sheaths of MCs are occupied by the slow or mirror mode waves in both expanding and non-expanding MCs.

Let us compare this result with the Earth's MSH. We used a similar procedure

to normalize the distance between the BS and MP and we presented a radial profiles of cross-correlations between B and N for the subsolar and flanks regions in Figure 5.16(b) that shows a large spread of correlations in the range from 0.5 to approx.-1 for whole MSH profile. Slightly higher values were found closer to the MP. It suggests an increasing portion of the slow and/or mirror mode waves or gradual dumping of the fast modes. From it follows that the MP plays a significant role in generation of instabilities with different types of MHD-wave modes, as we already noted in the previous chapter.

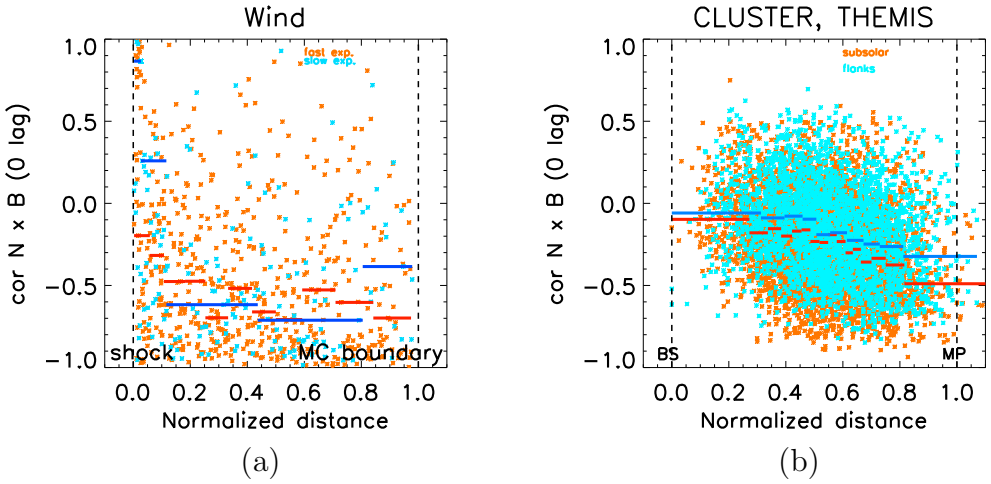

Figure 5.16: Distributions of correlation coefficients: (a) along the MC sheath and the difference between fast and slow MC expansions; (b) through the Earth's MSH profile.

Chapter 6

Conclusions

The thesis focuses on the analysis of MF and plasma density fluctuations in three types of sheaths: in the planetary sheaths (Earth and Jupiter), in the HSH, and in the sheaths of magnetic clouds. We compared correlation properties of the fluctuations in these environments, nevertheless, the main attention was dialed with the Earth's MSH. The following topics are discussed in details:

1. The prediction of the MSH B_Z component from IMF observations.
2. The correlation length of MF fluctuations in the Earth's MSH and its dependence on upstream conditions.
3. A comparison of Earth's MSH fluctuations with the fluctuations of other planetary sheaths and the sheath of MCs.

The statistical study of reliability of the prediction of the MSH B_Z component from IMF observations (*Šafránková et al.*, 2009)[**A1**] has shown that the probability of observation of the same sign of the B_Z component in the SW and at the particular point in the MSH (1) depends on the phase of solar cycle being largest at the solar minimum and gradually decreases with increasing solar activity and (2) rises with the B_Z magnitude from values close to 0.5 for $|B_Z| \sim 1$ nT and reaches unity for $|B_Z| \sim 10$ nT during solar minimum, whereas a value of 0.95 was obtained for solar maximum. Nevertheless, we can conclude that a coincidence of the sign of both MFs is very low from general point of view.

The second part of the thesis starts from a case study of ion flux fluctuations in the Earth's MSH observed by two shortly separated spacecraft (by $\sim 1R_E$). In *Gutynska et al.* (2007)[**A2**], we showed that the analyzed fluctuations are probably generated at the quasi-parallel BS and the level of fluctuations can differ by an order of magnitude in two points separated by $\sim 1R_E$. This result was continued by a series of statistical studies.

A statistical survey of the MSH MF fluctuations using two years of Cluster observations near the dawndusk meridional plane (*Gutynska et al.*, 2008)[**A3**] has shown that the correlation length of the fluctuations in the range of 0.001–0.125

Hz is approximately $1R_E$ in a statistical sense. However, we have also found a number of the cases when the correlation drops to 0.6–0.5 for separations shorter than $0.05R_E$. Also, in *Gutynska et al.* (2009)[**A4**], we showed that the correlation length of MSH MF fluctuations is generally short ($\sim 0.7R_E$), however, it is longer under specific upstream conditions: (1) during intervals of the high SW speeds; and (2) it slightly increases with higher values of the IMF strength. Similarly, the correlation length is longer (3) if the cross-correlation between the IMF and MSH MF is higher; and (4) if the amplitude of fluctuations represented by a standard deviation is larger.

From a study of MHD waves in the HSH (*Gutynska et al.*, 2010)[**A5**] it follows that typical correlation coefficients in the regions behind of the termination shock are about 0.55–0.65, larger than in the Earth's MSH. The largest correlations occur when the spectrum of MF fluctuations is dominated by low frequencies.

A comparison of properties of plasma and MF fluctuations in the planetary and other sheaths based on an analysis of high-resolution observations of the MF strength, B and proton density, N in the JSH, in the HSH behind the crossing of the TS, in the different locations of the Earth's MSH, and in the sheaths of magnetic clouds has shown: 1) slow or mirror wave modes (negative correlation coefficients) prevail in all sheaths except the HSH; 2) a portion of the fluctuations exhibiting correlated variations of the MF and plasma density increases with the distance from the Sun; 3) the typical cross-correlation coefficient is ~ 0.3 in the Earth's MSH; ~ 0.9 in the sheaths of magnetic clouds; ~ 0.5 in the JSH; and ~ 0.6 in the HSH. Moreover, in the case of the Earth's MSH, an anticorrelation between the plasma density and MF was observed, with higher cross-correlation coefficients in a close vicinity of the MP. It again suggests that the MP is a source of mirror mode waves.

References

Alexandrova, O., A. Mangeney, M. Maksimovic, N. Cornilleau-Wehrlin, J. Bosqued, and M. André (2006), Alfvén vortex filaments observed in magnetosheath downstream of a quasi-perpendicular bow shock, *J. Geophys. Res.*, *111*, 12,208–+, doi:10.1029/2006JA011934. 43

Alexandrova, O., C. Lacombe, and A. Mangeney (2008), Spectra and anisotropy of magnetic fluctuations in the Earth's magnetosheath: Cluster observations, *Ann. Geophys.*, *26*, 3585–3596. 57

Angelopoulos, V. (2008), The THEMIS Mission, *Space Sci. Rev.*, *141*, 5–34, doi:10.1007/s11214-008-9336-1. 30

Attié, D., L. Rezeau, G. Belmont, N. Cornilleau-Wehrlin, and E. Lucek (2008), Power of magnetopause low-frequency waves: A statistical study, *J. Geophys. Res. (Space Phys.)*, *113*, 7213–+, doi:10.1029/2007JA012606. 57

Auster, H. U., et al. (2008), The THEMIS Fluxgate Magnetometer, *Space Sci. Rev.*, *141*, 235–264, doi:10.1007/s11214-008-9365-9. 29, 36

Balogh, A., et al. (2001), The Cluster Magnetic Field Investigation: overview of in-flight performance and initial results, *Ann. Geophys.*, *19*, 1207–1217. 28, 36

Barnes, A. (1993), Motion of the heliospheric termination shock - A gas dynamic model, *J. Geophys. Res.*, *98*, 15,137–+, doi:10.1029/92JA02895. 22

Barnes, A. (1994), Motion of the heliospheric termination shock. 2: Energy loss due to energetic particle acceleration, *J. Geophys. Res.*, *99*, 6553–6560, doi:10.1029/94JA00262. 22

Barnes, A. (1995), Motion of the Heliospheric Termination Shock at High Heliographic Latitude, *Space Sci. Rev.*, *72*, 233–236, doi:10.1007/BF00768785. 22

Baumjohann, W., and R. A. Treumann (1996), *Basic space plasma physics*. 19

Baumjohann, W., O. H. Bauer, G. Haerendel, H. Junginger, and E. Amata (1983), Magnetospheric plasma drifts during a sudden impulse, *J. Geophys. Res.*, *88*, 9287–9289, doi:10.1029/JA088iA11p09287. 11

REFERENCES

Baumjohann, W., R. A. Treumann, E. Georgescu, G. Haerendel, K. Fornacon, and U. Auster (1999), Waveform and packet structure of lion roars, *Ann. Geophys.*, *17*, 1528–1534, doi:10.1007/s005850050878. 18

Bavassano Cattaneo, M. B., C. Basile, G. Moreno, and J. D. Richardson (1998), Evolution of mirror structures in the magnetosheath of Saturn from the bow shock to the magnetopause, *J. Geophys. Res.*, *103*, 11,961–11,972, doi:10.1029/97JA03683. 20, 23

Behannon, K. W., M. H. Acuna, L. F. Burlaga, R. P. Lepping, N. F. Ness, and F. M. Neubauer (1977), Magnetic field experiment for Voyagers 1 and 2, *Space Sci. Rev.*, *21*, 235–257, doi:10.1007/BF00211541. 33, 38

Bennett, L., M. G. Kivelson, K. K. Khurana, L. A. Frank, and W. R. Paterson (1997), A model of the Earth's distant bow shock, *J. Geophys. Res.*, *102*, 26,927–26,942, doi:10.1029/97JA01906. 8

Blanco-Cano, X., N. Omidi, and C. T. Russell (2006), Macrostructure of collisionless bow shocks: 2. ULF waves in the foreshock and magnetosheath, *J. Geophys. Res. (Space Phys.)*, *111*, 10,205–+, doi:10.1029/2005JA011421. 14

Boardsen, S. A., T. E. Eastman, T. Sotirelis, and J. L. Green (2000), An empirical model of the high-latitude magnetopause, *J. Geophys. Res.*, *105*, 23,193–23,220, doi:10.1029/1998JA000143. 11

Bogdanova, Y. V., et al. (2005), On the formation of the high-altitude stagnant cusp: Cluster observations, *Geophys. Res. Let.*, *32*, 12,101–+, doi:10.1029/2005GL022813. 43

Bridge, H. S., J. W. Belcher, R. J. Butler, A. J. Lazarus, A. M. Mavretic, J. D. Sullivan, G. L. Siscoe, and V. M. Vasyliunas (1977), The plasma experiment on the 1977 Voyager mission, *Space Sci. Rev.*, *21*, 259–287, doi:10.1007/BF00211542. 33, 38

Burlaga, L. F., and N. F. Ness (2009), Compressible "Turbulence" Observed in the Heliosheath by Voyager 2, *Astrophys. J.*, *703*, 311–324, doi:10.1088/0004-637X/703/1/311. 22

Burlaga, L. F., N. F. Ness, and M. H. Acũna (2006a), Trains of magnetic holes and magnetic humps in the heliosheath, *Geophys. Res. Let.*, *33*, 21,106–+, doi:10.1029/2006GL027276. 20, 23

Burlaga, L. F., N. F. Ness, and M. H. Acuña (2006b), Magnetic Fields in the Heliosheath: Voyager 1 Observations, *Astrophys. J.*, *642*, 584–592, doi:10.1086/500826. 23

Burlaga, L. F., N. F. Ness, M. H. Acuña, R. P. Lepping, J. E. P. Connerney, and J. D. Richardson (2008), Magnetic fields at the solar wind termination shock, *Nature*, *454*, 75–77, doi:10.1038/nature07029. 21

Burlaga, L. F., N. F. Ness, M. H. Acuña, J. D. Richardson, E. Stone, and F. B. McDonald (2009), Observations of the Heliosheath and Solar Wind Near the Termination Shock by Voyager 2, *Astrophys. J.*, *692*, 1125–1130, doi:10.1088/0004-637X/692/2/1125. 22

Cairns, I. H., and J. G. Lyon (1995), MHD simulations of Earth's bow shock at low Mach numbers: Standoff distances, *J. Geophys. Res.*, *100*, 17,173–17,180, doi:10.1029/95JA00993. 8, 9

Cairns, I. H., D. H. Fairfield, R. R. Anderson, V. E. H. Carlton, K. I. Paularena, and A. J. Lazarus (1995), Unusual locations of Earth's bow shock on September 24 - 25, 1987: Mach number effects, *J. Geophys. Res.*, *100*, 47–62, doi:10.1029/94JA01978. 9

Chandrasekhar, S., A. N. Kaufman, and K. M. Watson (1958), The Stability of the Pinch, *Proc. R. Soc. A*, *245*, 435–455. 16

Chapman, J. F., and I. H. Cairns (2003), Three-dimensional modeling of Earth's bow shock: Shock shape as a function of Alfvén Mach number, *J. Geophys. Res.*, *108*, 1174–+, doi:10.1029/2002JA009569. 8, 9, 10

Chapman, S., and J. Bartels (1941), Geomagnetism. Vol. I. Geomagnetic and related phenomana. Vol. II. Analysis and physical interpretation of the phenomena. The International Series of Monographs on Physics., *Quart. J. Royal Meteorol. Society*, *67*, 63–66, doi:10.1002/qj.49706728810. 3

Chapman, S., and V. C. A. Ferraro (1931a), a New Theory of Magnetic Storms, *J. Geophys. Res.*, *36*, 77–97, doi:10.1029/TE036i002p00077. 3

Chapman, S., and V. C. A. Ferraro (1931b), a New Theory of Magnetic Storms, *J. Geophys. Res.*, *36*, 171–186, doi:10.1029/TE036i003p00171. 3

Chisham, G., D. Burgess, S. J. Schwartz, and M. W. Dunlop (1998), Observations of electron distributions in magnetosheath mirror mode waves, *J. Geophys. Res.*, *103*, 26,765–26,774, doi:10.1029/98JA02620. 18

Coleman, I. J. (2005), A multi-spacecraft survey of magnetic field line draping in the dayside magnetosheath, *Ann. Geophys.*, *23*, 885–900, doi:10.5194/angeo-23-885-2005. 43

Constantinescu, O. D. (2002), Self-consistent model of mirror structures, *J. Atmos. and Solar-Terrestrial Phys.*, *64*, 645–649, doi:10.1016/S1364-6826(02)00024-X. 18, 19, 20

Constantinescu, O. D., K. Glassmeier, P. M. E. Décréau, M. Fränz, and K. Fornaçon (2007), Low frequency wave sources in the outer magnetosphere, magnetosheath, and near Earth solar wind, *Ann. Geophys.*, *25*, 2217–2228. 14

Crooker, N. U., T. E. Eastman, and G. S. Stiles (1979), Observations of plasma depletion in the magnetosheath at the dayside magnetopause, *J. Geophys. Res.*, *84*, 869–874, doi:10.1029/JA084iA03p00869. 20

REFERENCES

De Sterck, H., and S. Poedts (1999), Stationary slow shocks in the magnetosheath for solar wind conditions with $\beta<2/\gamma$: Three-dimensional MHD simulations, *J. Geophys. Res.*, *104*, 22,401–22,406, doi:10.1029/1999JA900299. 8

Decker, R. B., S. M. Krimigis, E. C. Roelof, M. E. Hill, T. P. Armstrong, G. Gloeckler, D. C. Hamilton, and L. J. Lanzerotti (2005), Voyager 1 in the Foreshock, Termination Shock, and Heliosheath, *Science*, *309*, 2020–2024, doi:10.1126/science.1117569. 21

Decker, R. B., S. M. Krimigis, E. C. Roelof, M. E. Hill, T. P. Armstrong, G. Gloeckler, D. C. Hamilton, and L. J. Lanzerotti (2008), Mediation of the solar wind termination shock by non-thermal ions, *Nature*, *454*, 67–70, doi:10.1038/nature07030. 21

Denton, R. E. (2000), ULF waves in the magnetosheath, *Int. J. Geomagn. Aeron.*, *2*, 1–14. 14, 15

Denton, R. E., S. P. Gary, X. Li, B. J. Anderson, J. W. Labelle, and M. Lessard (1995), Low-frequency fluctuations in the magnetosheath near the magnetopause, *J. Geophys. Res.*, *100*, 5665–5679, doi:10.1029/94JA03024. 15

Dušík, Š., G. Granko, J. Šafránková, Z. Němeček, and K. Jelínek (2010), IMF cone angle control of the magnetopause location: Statistical study, *Geophys. Res. Let.*, *37*, L19,103, doi:10.1029/2010GL044965. 11

Eriksson, S., et al. (2009), Magnetic island formation between large-scale flow vortices at an undulating postnoon magnetopause for northward interplanetary magnetic field, *J. Geophys. Res.*, *114*, 0–+, doi:10.1029/2008JA013505. 43

Escoubet, C. P., et al. (2008), Effect of a northward turning of the interplanetary magnetic field on cusp precipitation as observed by Cluster, *J. Geophys. Res.*, *113*, 7–+, doi:10.1029/2007JA012771. 43

Fairfield, D. H. (1971), Average and unusual locations for the earth's magnetopause and bow shock., *J. Geophys. Res.*, *76*, 6700–6716, doi:10.1029/JA076i028p06700. 8, 9, 11

Fairfield, D. H. (1995), *Observations of the Shape and Location of the Magnetopause: A Review*, pp. 53–+, the American Geophysical Union. 11

Fairfield, D. H., I. H. Cairns, M. D. Desch, A. Szabo, A. J. Lazarus, and M. R. Aellig (2001), The location of low Mach number bow shocks at Earth, *J. Geophys. Res.*, *106*, 25,361–25,376, doi:10.1029/2000JA000252. 8

Farris, M. H., and C. T. Russell (1994), Determining the standoff distance of the bow shock: Mach number dependence and use of models, *J. Geophys. Res.*, *99*, 17,681–+, doi:10.1029/94JA01020. 9

Farris, M. H., S. M. Petrinec, and C. T. Russell (1991), The thickness of the magnetosheath - Constraints on the polytropic index, *Geophys. Res. Let.*, *18*, 1821–1824, doi:10.1029/91GL02090. 8, 9

Farrugia, C. J., N. V. Erkaev, H. K. Biernat, L. F. Burlaga, R. P. Lepping, and V. A. Osherovich (1997), Possible plasma depletion layer ahead of an interplanetary ejecta, *J. Geophys. Res.*, *102*, 7087–7094, doi:10.1029/96JA03822. 20

Filbert, P. C., and P. J. Kellogg (1979), Electrostatic noise at the plasma frequency beyond the earth's bow shock, *J. Geophys. Res.*, *84*, 1369–1381, doi:10.1029/JA084iA04p01369. 9

Formisano, V. (1979), Orientation and shape of the earth's bow shock in three dimensions, *Planet. Space Sci.*, *27*, 1151–1161, doi:10.1016/0032-0633(79)90135-1. 9, 11

Fuselier, S. A., J. H. Waite, L. A. Avanov, V. M. Smirnov, O. L. Vaisberg, G. Siscoe, and C. T. Russell (2002), Characteristics of magnetosheath plasma in the vicinity of the high-altitude cusp, *Planet. Space Sci.*, *50*, 559–566. 8

Grzedzielski, S., and A. J. Lazarus (1993), 2- to 3-kHz continuum emissions as possible indications of global heliospheric 'breathing', *J. Geophys. Res.*, *98*, 5551–5558, doi:10.1029/92JA02395. 22

Gurnett, D. A., and W. S. Kurth (2008), Intense plasma waves at and near the solar wind termination shock, *Nature*, *454*, 78–80, doi:10.1038/nature07023. 21

Gutynska, O., Z. Němeček, and J. Šafránková (2007), Two-point observations of magnetosheath fluctuation, *WDS'07 Proceedings of Contributed Papers*, *2*, 34–41. 47, 48, 65

Gutynska, O., J. Šafránková, and Z. Němeček (2008), Correlation length of magnetosheath fluctuations: Cluster statistics, *Ann. Geophys.*, *26*, 2503–2513. 38, 49, 50, 51, 52, 53, 55, 65

Gutynska, O., J. Šafránková, and Z. Němeček (2009), Correlation properties of magnetosheath magnetic field fluctuations, *J. Geophys. Res.*, *114*, 8207–+, doi:10.1029/2009JA014173. 36, 52, 53, 54, 56, 57, 58, 60, 61, 66

Gutynska, O., J. Šafránková, Z. Němeček, and J. D. Richardson (2010), Correlations of Plasma Density and Magnetic Field Strength in the Heliosheath, *Astrophys. J.*, *722*, L228–L232, doi:10.1088/2041-8205/722/2/L228. 58, 59, 60, 61, 66

Hammond, C. M., J. L. Phillips, S. J. Bame, E. J. Smith, and C. G. Maclennan (1993), Ulysses observations of the planetary depletion layer at Jupiter, *Planet. Space Sci.*, *41*, 857–868, doi:10.1016/0032-0633(93)90093-H. 20

Hasegawa, A. (1969), Drift mirror instability of the magnetosphere., *Phys. Fluids*, *12*, 2642–2650, doi:10.1063/1.1692407. 17

Hasegawa, H., M. Fujimoto, K. Takagi, Y. Saito, T. Mukai, and H. Rème (2006), Single-spacecraft detection of rolled-up Kelvin-Helmholtz vortices at the flank magnetopause, *J. Geophys. Res.*, *111*, 9203–+, doi:10.1029/2006JA011728. 43

REFERENCES

Hayosh, M., J. Šafránková, Z. Němeček, L. Přech, K. Kudela, and G. N. Zastenker (2005), Relationship between high-energy particles and ion flux in the magnetosheath, *Planet. Space Sci.*, *53*, 103–115, doi:10.1016/j.pss.2004.09.034. 36

Hill, P., G. Paschmann, R. A. Treumann, W. Baumjohann, N. Sckopke, and H. Lühr (1995), Plasma and magnetic field behavior across the magnetosheath near local noon, *J. Geophys. Res.*, *100*, 9575–9584, doi:10.1029/94JA03194. 12, 20

Howe, H. C., Jr., and J. H. Binsack (1972), Explorer 33 and 35 plasma observations of magnetosheath flow., *J. Geophys. Res.*, *77*, 3334–3344, doi:10.1029/JA077i019p03334. 11

Hubert, D., C. Lacombe, C. C. Harvey, M. Moncuquet, C. T. Russell, and M. F. Thomsen (1998), Nature, properties, and origin of low-frequency waves from an oblique shock to the inner magnetosheath, *J. Geophys. Res.*, *103*, 26,783–26,798, doi:10.1029/98JA01011. 15, 61

Jeřáb, M., Z. Němeček, J. Šafránková, K. Jelínek, and J. Měrka (2005), Improved bow shock model with dependence on the IMF strength, *Planet. Space Sci.*, *53*, 85–93, doi:10.1016/j.pss.2004.09.032. 10, 37, 38, 39

Kaufmann, R. L., J. Horng, and A. Wolfe (1970), Large-amplitude hydromagnetic waves in the inner magnetosheath., *J. Geophys. Res.*, *75*, 4666–4676, doi:10.1029/JA075i025p04666. 20, 23

Kawano, H., and C. T. Russell (1997a), Survey of flux transfer events observed with the ISEE 1 spacecraft: Dependence on the interplanetary magnetic field, *J. Geophys. Res.*, *102*, 11,307–11,314, doi:10.1029/97JA00481. 43

Kawano, H., and C. T. Russell (1997b), Cause of postterminator flux transfer events, *J. Geophys. Res.*, *102*, 27,029–27,038, doi:10.1029/97JA02139. 44

King, J. H., and N. E. Papitashvili (2005), Solar wind spatial scales in and comparisons of hourly Wind and ACE plasma and magnetic field data, *J. Geophys. Res.*, *110*, 2104–+, doi:10.1029/2004JA010649. 37

Kivelson, M. G., and C. T. Russell (1995), *Introduction to Space Physics*. 12

Kivelson, M. G., and D. J. Southwood (1996), Mirror instability II: The mechanism of nonlinear saturation, *J. Geophys. Res.*, *101*, 17,365–17,372, doi:10.1029/96JA01407. 14, 18

Klimov, S., et al. (1997), ASPI experiment: measurements of fields and waves on board the INTERBALL-1 spacecraft, *Ann. Geophys.*, *15*, 514–527, doi:10.1007/s00585-997-0514-3. 36

Korotova, G. I., D. G. Sibeck, and T. Rosenberg (2008), Seasonal dependence of Interball flux transfer events, *Geophys. Res. Let.*, *35*, 5106–+, doi:10.1029/2008GL033254. 43

Kudela, K., M. Slivka, J. Rojko, and V. N. Lutsenko (1995), The apparatus DOK-2 (project INTERBALL): Output data structure and modes of operation, *preprint of Inst. Exp. Phys. UEF-01-95*, *20*, 35–+. 48

Lacombe, C., F. G. E. Pantellini, D. Hubert, C. C. Harvey, A. Mangeney, G. Belmont, and C. T. Russell (1992), Mirror and Alfvenic waves observed by ISEE 1-2 during crossings of the earth's bow shock, *Ann. Geophys.*, *10*, 772–784. 15

Lee, L. C., C. S. Wu, and C. P. Price (1987), On the generation of magnetosheath lion roars, *J. Geophys. Res.*, *92*, 2343–2348, doi:10.1029/JA092iA03p02343. 19

Lee, L. C., M. Yan, and J. G. Hawkins (1991), A study of slow-mode structures in the dayside magnetosheath, *Geophys. Res. Let.*, *18*, 381–384, doi:10.1029/90GL02787. 15

Lepping, R. P., L. F. Burlaga, and L. W. Klein (1981), Jupiter's magnetopause, bow shock, and 10-hour modulated magnetosheath Voyagers 1 and 2, *Geophys. Res. Let.*, *8*, 99–102, doi:10.1029/GL008i001p00099. 40

Lepping, R. P., D. B. Berdichevsky, C. Wu, A. Szabo, T. Narock, F. Mariani, A. J. Lazarus, and A. J. Quivers (2006), A summary of WIND magnetic clouds for years 1995-2003: model-fitted parameters, associated errors and classifications, *Ann. Geophys.*, *24*, 215–245. 39

Lepping, R. P., et al. (1995), The Wind Magnetic Field Investigation, *Space Sci. Rev.*, *71*, 207–229, doi:10.1007/BF00751330. 31

Li, X., H. R. Lewis, J. Labelle, T. Phan, and R. A. Treumann (1995), Characteristics of the Ion Pressure Tensor in the Earth's Magnetosheath, *Geophys. Res. Let.*, *22*, 667–670, doi:10.1029/95GL00005. 12

Lin, R. L., X. X. Zhang, S. Q. Liu, Y. L. Wang, and J. C. Gong (2010), A three-dimensional asymmetric magnetopause model, *J. Geophys. Res.*, *115*, A04,207, doi: 10.1029/2009JA014235. 11

Liu, Y., J. D. Richardson, J. W. Belcher, J. C. Kasper, and R. M. Skoug (2006), Plasma depletion and mirror waves ahead of interplanetary coronal mass ejections, *J. Geophys. Res.*, *111*, 9108–+, doi:10.1029/2006JA011723. 20

Liu, Y., J. D. Richardson, J. W. Belcher, and J. C. Kasper (2007), Temperature Anisotropy in a Shocked Plasma: Mirror-Mode Instabilities in the Heliosheath, *Astrophys. J.*, *659*, L65–L68, doi:10.1086/516568. 23, 61

Longmore, M., S. J. Schwartz, J. Geach, B. M. A. Cooling, I. Dandouras, E. A. Lucek, and A. N. Fazakerley (2005), Dawn-dusk asymmetries and sub-Alfvénic flow in the high and low latitude magnetosheath, *Ann. Geophys.*, *23*, 3351–3364. 13

Longmore, M., S. J. Schwartz, and E. A. Lucek (2006), Rotation of the magnetic field in Earth's magnetosheath by bulk magnetosheath plasma flow, *Ann. Geophys.*, *24*, 339–354. 13

REFERENCES

Lucek, E. A., M. W. Dunlop, A. Balogh, P. Cargill, W. Baumjohann, E. Georgescu, G. Haerendel, and K. Fornacon (1999), Mirror mode structures observed in the dawn-side magnetosheath by Equator-S, *Geophys. Res. Let.*, *26*, 2159–2162, doi: 10.1029/1999GL900490. 15

Lucek, E. A., et al. (2001), Cluster magnetic field observations in the magnetosheath: four-point measurements of mirror structures, *Ann. Geophys.*, *19*, 1421–1428. 52

Luhmann, J. G., R. J. Walker, C. T. Russell, N. U. Crooker, J. R. Spreiter, and S. S. Stahara (1984), Patterns of potential magnetic field merging sites on the dayside magnetopause, *J. Geophys. Res.*, *89*, 1739–1742, doi:10.1029/JA089iA03p01739. 13

Lynnyk, A., and M. Vandas (2010), Influence of Magnetic Cloud Expansion on Its Fits, in *American Institute of Physics Conference Series*. 62

Lynnyk, A., J. Šafránková, Z. Němeček, and J. D. Richardson (2011), Deformation of ICMEs/MCs along their path, *Planet. Space Sci.*, *59*, 840–847, doi:10.1016/j.pss. 2011.03.016. 39

McComas, D. J., S. J. Bame, P. Barker, W. C. Feldman, J. L. Phillips, P. Riley, and J. W. Griffee (1998), Solar Wind Electron Proton Alpha Monitor (SWEPAM) for the Advanced Composition Explorer, *Space Sci. Rev.*, *86*, 563–612, doi:10.1023/A: 1005040232597. 32, 37

McFadden, J. P., C. W. Carlson, D. Larson, J. Bonnell, F. Mozer, V. Angelopoulos, K. Glassmeier, and U. Auster (2008), THEMIS ESA First Science Results and Performance Issues, *Space Sci. Rev.*, *141*, 477–508, doi:10.1007/s11214-008-9433-1. 31

Merka, J., J. Safránková, and Z. Nemecek (2002), Cusp-like plasma in high altitudes: a statistical study of the width and location of the cusp from Magion-4, *Ann. Geophys.*, *20*, 311–320, doi:10.5194/angeo-20-311-2002. 43

Merka, J., A. Szabo, T. W. Narock, J. H. King, K. I. Paularena, and J. D. Richardson (2003a), A comparison of IMP 8 observed bow shock positions with model predictions, *J. Geophys. Res.*, *108*, 1077–+, doi:10.1029/2002JA009384. 8, 9, 10, 11

Merka, J., A. Szabo, J. Šafránková, and Z. Němeček (2003b), Earth's bow shock and magnetopause in the case of a field-aligned upstream flow: Observation and model comparison, *J. Geophys. Res.*, *108*, 1269–+, doi:10.1029/2002JA009697. 8

Naidu, K., and A. Barnes (1994), Motion of the heliospheric termination shock. 4: MHD effects, *J. Geophys. Res.*, *99*, 17,673–+, doi:10.1029/94JA01342. 22

Narita, Y., and K. Glassmeier (2005), Dispersion analysis of low-frequency waves through the terrestrial bow shock, *J. Geophys. Res. (Space Phys.)*, *110*, 12,215–+, doi:10.1029/2005JA011256. 16

Narita, Y., and K. Glassmeier (2006), Propagation pattern of low frequency waves in the terrestrial magnetosheath, *Ann. Geophys.*, *24*, 2441–2444. 16

Narita, Y., K. Glassmeier, K. Fornaçon, I. Richter, S. Schäfer, U. Motschmann, I. Dandouras, H. Rème, and E. Georgescu (2006), Low-frequency wave characteristics in the upstream and downstream regime of the terrestrial bow shock, *J. Geophys. Res.*, *111*, 1203–+, doi:10.1029/2005JA011231. 16

Nemecek, Z., and J. Safrankova (1991), The earth's bow shock and magnetopause position as a result of the solar wind-magnetosphere interaction, *J. Atmos. Ter. Phys.*, *53*, 1049–1054. 9

Nemecek, Z., A. Fedorov, J. Safrankova, and G. Zastenker (1997), Structure of the low-latitude magnetopause: MAGION-4 observations, *Ann. Geophys.*, *15*, 553–561, doi:10.1007/s005850050471. 27

Newell, P. T., C. Meng, D. G. Sibeck, and R. Lepping (1989), Some low-altitude cusp dependencies on the interplanetary magnetic field, *J. Geophys. Res.*, *94*, 8921–8927, doi:10.1029/JA094iA07p08921. 43

Nishida, A. (1989), Can random reconnection on the magnetopause produce the low latitude boundary layer?, *Geophys. Res. Let.*, *16*, 227–230, doi:10.1029/GL016i003p00227. 44

Nozdrachev, M. N., A. A. Skalsky, V. A. Styazhkin, and V. G. Petrov (1998), Some Results of Magnetic Field Measurements by the FM-3I Flux-Gate Instrument Onboard the INTERBALL-1 Spacecraft, *Cosmic Res.*, *36*, 251–+. 28

Němeček, Z., J. Měrka, and J. Šafránková (2000a), The tilt angle control of the outer cusp position, *Geophys. Res. Let.*, *27*, 77–80, doi:10.1029/1999GL010699. 43

Němeček, Z., Šafr, J. ánková, L. Přech, G. N. Zastenker, K. I. Paularena, and S. Kokubun (2000b), Magnetosheath Study: Interball Observation, *Adv. Space Res.*, *25*, 1511–1516, doi:10.1016/S0273-1177(99)00663-8. 13

Němeček, Z., J. Šafránková, G. N. Zastenker, P. Pišoft, K. I. Paularena, and J. D. Richardson (2000c), Observations of the radial magnetosheath profile and a comparison with gasdynamic model predictions, *Geophys. Res. Let.*, *27*, 2801–2804, doi:10.1029/2000GL000063. 13

Němeček, Z., J. Šafránková, P. Pišoft, and G. N. Zastenker (2001), Statistical Study of Ion Flux Fluctuations in the Magnetosheath, *Czech. J. Phys.*, *51*, 853–862, doi:10.1023/A:1011630618180. 13

Němeček, Z., J. Šafránková, G. N. Zastenker, P. Pišoft, and K. I. Paularena (2002), Spatial distribution of the magnetosheath ion flux, *Adv. Space Res.*, *30*, 2751–2756, doi:10.1016/S0273-1177(02)80402-1. 13

Němeček, Z., et al. (2003), Structure of the outer cusp and sources of the cusp precipitation during intervals of a horizontal IMF, *J. Geophys. Res.*, *108*, 1420–+, doi:10.1029/2003JA009916. 43, 45

Nykyri, K., A. Otto, B. Lavraud, C. Mouikis, L. M. Kistler, A. Balogh, and H. Rème (2006), Cluster observations of reconnection due to the Kelvin-Helmholtz instability at the dawnside magnetospheric flank, *Ann. Geophys.*, *24*, 2619–2643, doi:10.5194/angeo-24-2619-2006. 43

Ogilvie, K. W., et al. (1995), SWE, A Comprehensive Plasma Instrument for the Wind Spacecraft, *Space Sci. Rev.*, *71*, 55–77, doi:10.1007/BF00751326. 31

Ogino, T., R. I. Walker, and M. Ashour-Abdalla (1992), A global magnetohydrodynamic simulation of the magnetosheath and magnetosphere when the interplanetary magnetic field is northward, *IEEE Trans. Plasma Sci.*, *20*, 817–828, doi:10.1109/27.199534. 5

Parker, E. N. (1958), Dynamics of the Interplanetary Gas and Magnetic Fields., *Astrophys. J.*, *128*, 664–+, doi:10.1086/146579. 1

Parker, E. N. (1963), *Interplanetary dynamical processes.* 21

Paularena, K. I., J. D. Richardson, M. A. Kolpak, C. R. Jackson, and G. L. Siscoe (2001), A dawn-dusk density asymmetry in Earth's magnetosheath, *J. Geophys. Res.*, *106*, 25,377–25,394, doi:10.1029/2000JA000177. 13, 36

Peredo, M., J. A. Slavin, E. Mazur, and S. A. Curtis (1995), Three-dimensional position and shape of the bow shock and their variation with Alfvenic, sonic and magnetosonic Mach numbers and interplanetary magnetic field orientation, *J. Geophys. Res.*, *100*, 7907–7916, doi:10.1029/94JA02545. 8, 9

Petrinec, S. M., and C. T. Russell (1993), An empirical model of the size and shape of the near-earth magnetotail, *Geophys. Res. Let.*, *20*, 2695–2698, doi:10.1029/93GL02847. 11

Petrinec, S. M., and C. T. Russell (1996), Near-Earth magnetotail shape and size as determined from the magnetopause flaring angle, *J. Geophys. Res.*, *101*, 137–152, doi:10.1029/95JA02834. 11

Petrinec, S. M., and C. T. Russell (1997), Hydrodynamic and MHD Equations across the Bow Shock and Along the Surfaces of Planetary Obstacles, *Space Sci. Rev.*, *79*, 757–791, doi:10.1023/A:1004938724300. 8

Petrinec, S. P., P. Song, and C. T. Russell (1991), Solar cycle variations in the size and shape of the magnetopause, *J. Geophys. Res.*, *96*, 7893–7896, doi:10.1029/90JA02566. 11

Phan, T., G. Paschmann, W. Baumjohann, N. Sckopke, and H. Luehr (1994), The magnetosheath region adjacent to the dayside magnetopause: AMPTE/IRM observations, *J. Geophys. Res.*, *99*, 121–141, doi:10.1029/93JA02444. 12

Phan, T. D., et al. (1996), The subsolar magnetosheath and magnetopause for high solar wind ram pressure: WIND observations, *Geophys. Res. Let.*, *23*, 1279–1282, doi:10.1029/96GL00845. 12

Phan, T. D., et al. (1997), Low-latitude dusk flank magnetosheath, magnetopause, and boundary layer for low magnetic shear: Wind observations, *J. Geophys. Res.*, *102*, 19,883–19,896, doi:10.1029/97JA01596. 12

Pokhotelov, O. A., and V. A. Pilipenko (1976), Contribution to the theory of the drift-mirror instability of the magnetospheric plasma, *Geomagn. Aeron.*, *16*, 504–510. 17

Pokhotelov, O. A., M. A. Balikhin, R. A. Treumann, and V. P. Pavlenko (2001), Drift mirror instability revisited: 1. Cold electron temperature limit, *J. Geophys. Res.*, *106*, 8455–8464, doi:10.1029/2000JA000069. 17

Pokhotelov, O. A., I. Sandberg, R. Z. Sagdeev, R. A. Treumann, O. G. Onishchenko, M. A. Balikhin, and V. P. Pavlenko (2003), Slow drift mirror modes in finite electron-temperature plasma: Hydrodynamic and kinetic drift mirror instabilities, *J. Geophys. Res. (Space Phys.)*, *108*, 1098–+, doi:10.1029/2002JA009651. 17

Pokhotelov, O. A., R. Z. Sagdeev, M. A. Balikhin, and R. A. Treumann (2004), Mirror instability at finite ion-Larmor radius wavelengths, *J. Geophys. Res. (Space Phys.)*, *109*, 9213–+, doi:10.1029/2004JA010568. 18

Powell, K. G., P. L. Roe, T. J. Linde, T. I. Gombosi, and D. L. de Zeeuw (1999), A Solution-Adaptive Upwind Scheme for Ideal Magnetohydrodynamics, *J. Comp. Phys.*, *154*, 284–309, doi:10.1006/jcph.1999.6299. 8

Ratkiewicz, R., A. Barnes, G. A. Molvik, J. R. Spreiter, and S. S. Stahara (1996), Heliospheric termination shock motion due to fluctuations in the solar wind upstream conditions: Spherically symmetric model, *J. Geophys. Res.*, *101*, 27,483–27,498, doi:10.1029/96JA02233. 22

Rème, H., et al. (2001), First multispacecraft ion measurements in and near the Earth's magnetosphere with the identical Cluster ion spectrometry (CIS) experiment, *Ann. Geophys.*, *19*, 1303–1354. 28

Richardson, J. D., and Y. Liu (2007), A comparison of magnetosheaths, ICME sheaths, and the heliosheath, in *Turbulence and Nonlinear Processes in Astrophysical Plasmas*, *American Institute of Physics Conference Series*, vol. 932, edited by D. Shaikh & G. P. Zank, pp. 387–392, doi:10.1063/1.2778990. 20, 61

Richardson, J. D., J. C. Kasper, C. Wang, J. W. Belcher, and A. J. Lazarus (2008), Cool heliosheath plasma and deceleration of the upstream solar wind at the termination shock, *Nature*, *454*, 63–66, doi:10.1038/nature07024. 21

Roelof, E. C., and D. G. Sibeck (1993), Magnetopause shape as a bivariate function of interplanetary magnetic field B_z and solar wind dynamic pressure, *J. Geophys. Res.*, *98*, 21,421–+, doi:10.1029/93JA02362. 11

Rudakov, L. I., and R. Z. Sagdeev (1961), A quasi-hydrodynamic description of a rarefied plasma in a magnetic field, in *Plasma Physics and the Problem of Controlled Thermonuclear Reactions, Volume 3*, edited by M. A. Leontovich, pp. 321–+. 16

REFERENCES

Russell, C. T. (1985), Planetary bow shocks, *Washington DC American Geophysical Union Geophysical Monograph Series*, *35*, 109–130. 8

Russell, C. T., and T. Zhang (1992), Unusually distant bow shock encounters at Venus, *Geophys. Res. Let.*, *19*, 833–836, doi:10.1029/92GL00634. 8

Safrankova, J., G. Zastenker, Z. Nemecek, A. Fedorov, M. Simersky, and L. Prech (1997), Small scale observation of magnetopause motion: preliminary results of the INTERBALL project, *Ann. Geophys.*, *15*, 562–569, doi:10.1007/s005850050472. 27

Samsonov, A. (2006), Numerical modelling of the Earths magnetosheath for different IMF orientations, *Adv. Space Res.*, *38*, 1652–1656, doi:10.1016/j.asr.2005.06.009. 8

Savin, S., et al. (2002), On the properties of turbulent boundary layer over polar cusps, *Nonlin. Proc. Geophys.*, *9*, 443–451. 13, 43

Savin, S., et al. (2004), Magnetosheath-cusp interface, *Ann. Geophys.*, *22*, 183–212. 13, 43

Savin, S. P., et al. (2001), Turbulent Boundary Layer at the Border of Geomagnetic Trap, *JETP Lett.*, *74*, 547–551, doi:10.1134/1.1450288. 13

Schäfer, S., K. Glassmeier, Y. Narita, K. H. Fornaçon, I. Dandouras, and M. Fränz (2005), Statistical phase propagation and dispersion analysis of low frequency waves in the magnetosheath, *Ann. Geophys.*, *23*, 3339–3349. 15

Schwartz, S. J., D. Burgess, and J. J. Moses (1996), Low-frequency waves in the Earthś magnetosheath: present status, *Ann. Geophys.*, *14*, 1134–1150, doi:10.1007/s005850050376. 13, 14, 61

Shevyrev, N. N., and G. N. Zastenker (2005), Some features of the plasma flow in the magnetosheath behind quasi-parallel and quasi-perpendicular bow shocks, *Planet. Space Sci.*, *53*, 95–102, doi:10.1016/j.pss.2004.09.033. 14

Shevyrev, N. N., G. N. Zastenker, P. E. Eiges, and J. D. Richardson (2006), Low frequency waves observed by Interball-1 in foreshock and magnetosheath, *Adv. Space Res.*, *37*, 1516–1521, doi:10.1016/j.asr.2005.07.072. 14

Shue, J., J. K. Chao, H. C. Fu, C. T. Russell, P. Song, K. K. Khurana, and H. J. Singer (1997), A new functional form to study the solar wind control of the magnetopause size and shape, *J. Geophys. Res.*, *102*, 9497–9512, doi:10.1029/97JA00196. 11, 37, 38, 39, 56

Sibeck, D. G. (2009), Concerning the occurrence pattern of flux transfer events on the dayside magnetopause, *Ann. Geophys.*, *27*, 895–903, doi:10.5194/angeo-27-895-2009. 44

Sibeck, D. G., R. E. Lopez, and E. C. Roelof (1991), Solar wind control of the magnetopause shape, location, and motion, *J. Geophys. Res.*, *96*, 5489–5495, doi:10.1029/90JA02464. 11

Siscoe, G., and D. Odstrcil (2008), Ways in which ICME sheaths differ from magnetosheaths, *J. Geophys. Res. (Space Phys.)*, *113*, 0–+, doi:10.1029/2008JA013142. 20

Siscoe, G. L., et al. (2002), MHD properties of magnetosheath flow, *Planet. Space Sci.*, *50*, 461–471. 8

Smith, C. W., J. L'Heureux, N. F. Ness, M. H. Acuña, L. F. Burlaga, and J. Scheifele (1998), The ACE Magnetic Fields Experiment, *Space Sci. Rev.*, *86*, 613–632, doi:10.1023/A:1005092216668. 32

Smith, E. J., J. A. Slavin, R. D. Zwickl, and S. J. Bame (1986), Shocks and storm sudden commencements, in *Solar Wind Magnetosphere Coupling*, *Astrophysics and Space Science Library*, vol. 126, edited by Y. Kamide & J. A. Slavin, pp. 345–365. 11

Song, P., C. T. Russell, J. T. Gosling, M. Thomsen, and R. C. Elphic (1990), Observations of the density profile in the magnetosheath near the stagnation streamline, *Geophys. Res. Let.*, *17*, 2035–2038, doi:10.1029/GL017i011p02035. 15

Song, P., C. T. Russell, and M. F. Thomsen (1992a), Waves in the inner magnetosheath - A case study, *Geophys. Res. Let.*, *19*, 2191–2194, doi:10.1029/92GL02499. 15

Song, P., C. T. Russell, and M. F. Thomsen (1992b), Slow mode transition in the frontside magnetosheath, *J. Geophys. Res.*, *97*, 8295–8305, doi:10.1029/92JA00381. 15

Song, P., C. T. Russell, T. I. Gombosi, J. R. Spreiter, S. S. Stahara, and X. X. Zhang (1999a), On the processes in the terrestrial magnetosheath 1. Scheme development, *J. Geophys. Res.*, *104*, 22,345–22,356, doi:10.1029/1999JA900247. 7

Song, P., C. T. Russell, X. X. Zhang, S. S. Stahara, J. R. Spreiter, and T. I. Gombosi (1999b), On the processes in the terrestrial magnetosheath 2. Case study, *J. Geophys. Res.*, *104*, 22,357–22,374, doi:10.1029/1999JA900246. 7

Southwood, D. J., and M. G. Kivelson (1992), On the form of the flow in the magnetosheath, *J. Geophys. Res.*, *97*, 2873–2879, doi:10.1029/91JA02446. 15

Spreiter, J. R., and S. S. Stahara (1985), Magnetohydrodynamic and gasdynamic theories for planetary bow waves, *Washington DC American Geophysical Union Geophysical Monograph Series*, *35*, 85–107. 8

Spreiter, J. R., A. L. Summers, and A. Y. Alksne (1966), Hydromagnetic flow around the magnetosphere, *Planet. Space Sci.*, *14*, 223–+, doi:10.1016/0032-0633(66)90124-3. 6, 7, 8, 56

Stahara, S. S. (2002), Adventures in the magnetosheath: two decades of modeling and planetary applications of the Spreiter magnetosheath model, *Planet. Space Sci.*, *50*, 421–442. 8

Stasiewicz, K. (2004), Theory and Observations of Slow-Mode Solitons in Space Plasmas, *Phys. Rev. Lett.*, *93*(12), 125,004–+, doi:10.1103/PhysRevLett.93.125004. 16

Stone, E. C., A. C. Cummings, F. B. McDonald, B. C. Heikkila, N. Lal, and W. R. Webber (2005), Voyager 1 Explores the Termination Shock Region and the Heliosheath Beyond, *Science*, *309*, 2017–2020, doi:10.1126/science.1117684. 21

Stone, E. C., A. C. Cummings, F. B. McDonald, B. C. Heikkila, N. Lal, and W. R. Webber (2008), An asymmetric solar wind termination shock, *Nature*, *454*, 71–74, doi:10.1038/nature07022. 21

Sundkvist, D., V. Krasnoselskikh, P. K. Shukla, A. Vaivads, M. André, S. Buchert, and H. Rème (2005), In situ multi-satellite detection of coherent vortices as a manifestation of Alfvénic turbulence, *Nature*, *436*, 825–828, doi:10.1038/nature03931. 43

Tajiri, M. (1967), Propagation of Hydromagnetic Waves in Collisionless Plasma. II. Kinetic Approach, *J. Phys. Society of Japan*, *22*, 1482–+. 17

Tátrallyay, M., and G. ErdőS (2002), The evolution of mirror mode fluctuations in the terrestrial magnetosheath, *Planet. Space Sci.*, *50*, 593–599. 15

Tátrallyay, M., G. Erdős, A. Balogh, and I. Dandouras (2008), The evolution of mirror type magnetic fluctuations in the magnetosheath based on multipoint observations, *Adv. Space Res.*, *41*, 1537–1544, doi:10.1016/j.asr.2007.03.039. 16, 61

Tkachenko, O., J. Šafránková, Z. Němeček, J. Šimůnek, and L. Přech (2008), Observations of vortex-like structure in the cusp-magnetosheath region during northward IMF orientation, *Ann. Geophys.*, *26*, 3375–3387, doi:10.5194/angeo-26-3375-2008. 43

Treumann, R. A., and W. Baumjohann (1997), *Advanced space plasma physics*. 18

Treumann, R. A., E. Georgescu, and W. Baumjohann (2000), Lion Roar Trapping in Mirror Modes, *Geophys. Res. Let.*, *27*, 1843–+, doi:10.1029/2000GL003767. 18

Treumann, R. A., C. H. Jaroschek, O. D. Constantinescu, R. Nakamura, O. A. Pokhotelov, and E. Georgescu (2004), The strange physics of low frequency mirror mode turbulence in the high temperature plasma of the magnetosheath, *Nonlin. Proc. Geophys.*, *11*, 647–657. 18

Tsurutani, B. T., D. J. Southwood, E. J. Smith, and A. Balogh (1992), Nonlinear magnetosonic waves and mirror mode structures in the March 1991 ULYSSES interplanetary event, *Geophys. Res. Let.*, *19*, 1267–1270, doi:10.1029/92GL00782. 20, 23

Šafránková, J., M. Hayosh, Z. Němeček, and L. Přech (2005), Magnetosheath investigations: Interball contribution to the topic, in *Multiscale Processes in the Earths Magnetosphere: From Interball to Cluster*, vol. 178, pp. 73–94, Kluwer Academic Publishers. 13

Šafránková, J., Z. Němeček, L. Přech, J. Šimnek, D. Sibeck, and J. Sauvaud (2007), Variations of the flank LLBL thickness as response to the solar wind dynamic pressure and IMF orientation, *J. Geophys. Res.*, *112*, 7201–+, doi:10.1029/2006JA011889. 44

Šafránková, J., M. Hayosh, O. Gutynska, Z. Němeček, and L. Přech (2009), Reliability of prediction of the magnetosheath B_Z component from interplanetary magnetic field observations, *J. Geophys. Res.*, *114*, 12,213+–, doi:10.1029/2009JA014552. 43, 45, 65

Verigin, M., G. Kotova, A. Szabo, J. Slavin, T. Gombosi, K. Kabin, F. Shugaev, and A. Kalinchenko (2001), Wind observations of the terrestrial bow shock: 3-D shape and motion, *Earth Planet. Space*, *53*, 1001–1009. 8

Verigin, M., J. Slavin, A. Szabo, G. Kotova, and T. Gombosi (2003), Planetary bow shocks: Asymptotic MHD Mach cones, *Earth Planet. Space*, *55*, 33–38. 8

Violante, L., M. B. B. Cattaneo, G. Moreno, and J. D. Richardson (1995), Observations of mirror waves and plasma depletion layer upstream of Saturn's magnetopause, *J. Geophys. Res.*, *100*, 12,047–+, doi:10.1029/94JA02703. 20, 23

Volwerk, M., T. L. Zhang, K. H. Glassmeier, A. Runov, W. Baumjohann, A. Balogh, H. Rème, B. Klecker, and C. Carr (2008), Study of waves in the magnetotail region with cluster and DSP, *Adv. Space Res.*, *41*, 1593–1597, doi:10.1016/j.asr.2007.04.005. 43

Wang, C., and J. W. Belcher (1998), Numerical investigation of hydrodynamic instabilities of the heliopause, *J. Geophys. Res.*, *103*, 247–+, doi:10.1029/97JA02773. 22

Wang, C., and J. W. Belcher (1999), The heliospheric boundary response to large-scale solar wind fluctuations: A gasdynamic model with pickup ions, *J. Geophys. Res.*, *104*, 549–556, doi:10.1029/1998JA900052. 22

Whang, Y. C., and L. F. Burlanga (1993), Termination shock - Solar cycle variations of location and speed, *J. Geophys. Res.*, *98*, 15,221–+, doi:10.1029/93JA01472. 22

Whang, Y. C., J. Y. Lu, and L. F. Burlaga (1999), The termination shock: 1979-1995, *J. Geophys. Res.*, *104*, 28,255–28,262, doi:10.1029/1999JA900413. 22

Wilken, B., C. K. Goertz, D. N. Baker, P. R. Higbie, and T. A. Fritz (1982), The SSC on July 29, 1977 and its propagation within the magnetosphere, *J. Geophys. Res.*, *87*, 5901–5910, doi:10.1029/JA087iA08p05901. 11

Wu, C. C. (1992), MHD flow past an obstacle - Large-scale flow in the magnetosheath, *Geophys. Res. Let.*, *19*, 87–90, doi:10.1029/91GL03007. 7

Zastenker, G. N., M. N. Nozdrachev, Z. Němeček, J. Šafránková, L. Přech, K. I. Paularena, A. J. Lazarus, R. P. Lepping, and T. Mukai (1999), Plasma and magnetic field variations in the magnetosheath: Interball-1 and ISTP Spacecraft observations, in *NATO ASIC Proc. 537: Interball in the ISTP Program : Studies of the Solar*

Wind-Magnetosphere-Ionosphere Interaction, edited by D. G. Sibeck & K. Kudela, pp. 277–+. 15, 51

Zastenker, G. N., M. N. Nozdrachev, Z. Němeček, J. Šafránková, K. I. Paularena, J. D. Richardson, R. P. Lepping, and T. Mukai (2002), Multispacecraft measurements of plasma and magnetic field variations in the magnetosheath: Comparison with Spreiter models and motion of the structures, *Planet. Space Sci.*, *50*, 601–612. 15, 51

Zhang, H., M. W. Dunlop, Q. Zong, T. A. Fritz, A. Balogh, and Y. Wang (2007), Geometry of the high-latitude magnetopause as observed by Cluster, *J. Geophys. Res.*, *112*, 2204–+, doi:10.1029/2006JA011774. 43

Zwan, B. J., and R. A. Wolf (1976), Depletion of solar wind plasma near a planetary boundary, *J. Geophys. Res.*, *81*, 1636–1648, doi:10.1029/JA081i010p01636. 7, 15

Appendix: List of abbreviations

BS	Bow Shock
HSH	Heliosheath
IB-1	INTERBALL-1 spacecraft
ICME	Interplanetary Coronal Mass Ejections
IMF	Interplanetary Magnetic Field
JSH	Jupiter's Sheath
M4	MAGION-4 spacecraft
MC	Magnetic Cloud
MF	Magnetic Field
MHD	Magnetohydrodynamics
MP	Magnetopause
MSH	Magnetosheath
R_E	Earth Radius
SW	Solar Wind
TS	Termination Shock
V1	Voyager 1 probe
V2	Voyager 2 probe

Appendix: List of publications

A1: Šafránková, J, M. Hayosh, O. Gutynska, Z. Němeček, and L. Přech (2009), Reliability of prediction of the magnetosheath Bz component from interplanetary magnetic field observations, *J. Geophys. Res-Space Phys.*, 114 (A12): Art. No. A12213 (7 pages), doi:10.1029/2009JA014552.

A2: Gutynska, O., Z. Němeček, and J. Šafránková (2007), Two-point observations of magnetosheath fluctuation, *in WDS'07 Proceedings of Contributed Papers*, 2, 34-41.

A3: Gutynska, O., J. Šafránková, and Z. Němeček (2008), Correlation length of magnetosheath fluctuations: Cluster statistics, *Ann. Geophys.*, 26 (9): 2503-2513.

A4: Gutynska, O., J. Šafránková, and Z. Němeček (2009), Correlation properties of magnetosheath magnetic field fluctuations, *J. Geophys. Res-Space Phys.*, 114 (A8): Art. No. A08207 (11 pages), doi:10.1029/2009JA014173.

A5: Gutynska, O., J. Šafránková, Z. Němeček, and J. D. Richardson (2010), Correlations of Plasma Density and Magnetic Field Strength in the Heliosheath, *Astrophys. J. Lett.*, 722 (2): L228-L232, doi:10.1088/2041-8205/722/2/L228.

A1 - Safránková et al. (2009)

Šafránková, J, M. Hayosh, O. Gutynska, Z. Němeček, and L. Přech (2009), Reliability of prediction of the magnetosheath Bz component from interplanetary magnetic field observations, *J. Geophys. Res.*, 114 (A12): Art. No. A12213 (7 pages), doi:10.1029/2009JA014552.

A2 - Gutynska et al. (2007)

Gutynska, O., Z. Němeček, and J. Šafránková (2007), Two-point observations of magnetosheath fluctuation, *in WDS'07 Proceedings of Contributed Papers*, 2, 34-41.

A3 - Gutynska et al. (2008)

Gutynska, O., J. Šafránková, and Z. Němeček (2008), Correlation length of magnetosheath fluctuations: Cluster statistics, *Ann. Geophys.*, 26 (9): 2503-2513.

A4 - Gutynska et al. (2009)

Gutynska, O., J. Šafránková, and Z. Němeček (2009), Correlation properties of magnetosheath magnetic field fluctuations, *J. Geophys. Res.*, 114 (A8): Art. No. A08207 (11 pages), doi:10.1029/2009JA014173.

A5 - Gutynska et al. (2010)

Gutynska, O., J. Šafránková, Z. Němeček, and J. D. Richardson (2010), Correlations of Plasma Density and Magnetic Field Strength in the Heliosheath, *Astrophys. J. Lett.*, 722 (2): L228-L232, doi: 10.1088/2041-8205/722/2/L228.